Snow modeling to predict surface contamination of cars

Capturing snow adhesion and build-up on the automotive exterior using multi-phase modeling

Master's thesis in Applied Mechanics
Department of Mechanics and Maritime Sciences
CHALMERS UNIVERSITY OF TECHNOLOGY
Göteborg, Sweden 2021

TEJAS SHARMA BANGALORE NARAHARI
YASHAS BHARADHWAJ

MASTER'S THESIS IN APPLIED MECHANICS 2021:43

Snow modeling to predict surface contamination of cars

Capturing snow adhesion and build-up on the automotive exterior using multi-phase modeling

TEJAS SHARMA BANGALORE NARAHARI
YASHAS BHARADHWAJ

Department of Mechanics and Maritime Sciences
Division of Fluid Dynamics
Chalmers University of Technology
Göteborg, Sweden 2021

Snow modeling to predict surface contamination of cars
Capturing snow adhesion and build-up on the automotive exterior using multi-phase modeling
TEJAS SHARMA BANGALORE NARAHARI
YASHAS BHARADHWAJ

Examiner and Academic Supervisor:
Henrik Ström
Associate Professor - Fluid Dynamics
Department of Mechanics and Maritime Sciences
Chalmers University of Technology

Industrial Supervisors:
Tobias Eidevåg
Industrial PhD Student, Contamination and Core CFD
Volvo Car Corporation

David Kallin
CAE Engineer, Contamination and Core CFD
Volvo Car Corporation

Master's Thesis 2021:43
Department of Mechanics and Maritime Sciences
Division of Fluid Dynamics
Chalmers University of Technology
SE-412 96 Göteborg
Telephone +46 31 772 1000

Cover: Ahmed Body subjected to snow contamination test in wind tunnel.

Printed by Chalmers Reproservice
Göteborg, Sweden 2021

Snow modeling to predict surface contamination of cars
Capturing snow adhesion and build-up on the automotive exterior using multi-phase modeling
TEJAS SHARMA BANGALORE NARAHARI
YASHAS BHARADHWAJ
Department of Mechanics and Maritime Sciences
Chalmers University of Technology

ABSTRACT

Passenger safety and autonomous transportation have been few of the important innovations in the development of modern-day cars amongst the top-tier automobile manufacturers. Correspondingly, innovation in the level of passenger safety has evolved from just passive safety systems towards enhanced active safety systems such as Advanced Driver Safety System (ADAS), in recent times. Such systems are generally comprised of various sub-systems including radar sensors, cameras, etc. Contamination or exterior soiling on these is one of the major issues at hand that are hindering their functionalities.

Contamination due to snow being one of the bigger issues under winter conditions poses a significant challenge towards its functionalities which needs to be addressed. Field testing and wind tunnel experiments are being used traditionally at Volvo Cars to address the above issue. As a scope of this project, the challenge is to develop a model which predicts the snow contamination on automotive cars or bluff bodies using a Multi-phase CFD simulation approach.

An aerodynamic analysis is initially performed to understand the flow features around the subject of interest. Later, particle simulation using the Lagrangian Particle Tracking method to study snow deposition is performed. To contrast with the results from simulation, wind tunnel experiments with similar test conditions are conducted over two bluff bodies, a Wedge section and an Ahmed body subjected to snow. The simulation results and experimental results are then compared with each other to analyse the deposition pattern in both real-world conditions and simulations.

Keywords: Multi-phase Modeling, Lagrangian Particle Tracking, Snow, Wind Tunnel Testing, Wedge, Ahmed Body.

PREFACE

This report is a detailed document of the master's thesis project done by Tejas Sharma Bangalore Narahari and Yashas Bharadhwaj which serves as completion of Master of Science Degree in Applied Mechanics at Chalmers University of Technology, Gothenburg, Sweden between the academic years 2019-21. The tenure of this thesis work is ten months carried out between the Autumn of 2020 and Spring of 2021 at the Contamination and Core CFD department at Volvo Cars Corporation in collaboration with the Division of Fluid Dynamics, the Chalmers University of Technology. The main goal of this thesis project is to predict snow impingement and snow accumulation on cars. This thesis work was examined by Henrik Ström at Chalmers University of Technology, supervised by Tobias Eidevåg and David Kallin at Volvo Cars and opposed by *Hariharan Sri Prasanna Venkatesh*, Applied Mechanics master's programme, Chalmers University of Technology and *Wei Wang*, Automotive master's programme, Chalmers University of Technology.

This report was typset using LaTeX

ACKNOWLEDGEMENTS

This thesis was written under the extraordinary circumstances of the Covid-19 pandemic. Most of the work was done away from the office and a lot of information was shared online. We would like to thank our supervisors Tobias Eidevåg and David Kallin for their patience, continuous support, guidance and constructive feedback throughout the tenure of this thesis. Our work would not have been this good if it were not for their continuous help in us learning about the new concepts in Multiphase and CFD. Thank you both for putting up with our endless questions and also for being there with us personally!

We would also like to thank the whole Contamination and Core CFD team for helping us with our small queries during the thesis work. We would like to thank Volvo Cars Corporation for providing us with the necessary resources to do our job well and also for allowing us to perform wind tunnel tests and go on a field trip.

We would like to thank our examiner Henrik Ström from the Chalmers University of Technology for his immense sharing of knowledge, guidance, support, and continuous monitoring of our progress to channel us on the right path throughout this project. We would like to thank Prof. Lars Davidson for his help in our thesis work regarding turbulence. Finally, we would like to thank our family and friends for being there with us during these hard times and constantly supporting and motivating us to do better.

Tejas Sharma Bangalore Narahari, Göteborg, June 2021
Yashas Bharadhwaj, Göteborg, June 2021

NOMENCLATURE

Acronyms

$ADAS$	Advanced Driver Assistance Systems
BL	Boundary Layer
BR	Blockage Ratio
CAD	Computer Aided Drawing
CCN	Convective Courant Number
CFD	Computational Fluid Dynamics
$DDES$	Delayed Detached Eddy Simulation
DEM	Discrete Element Method
DES	Detached Eddy Simulation
DRW	Discrete Random Walk model
EWM	Exterior Water Management
$IDDES$	Improved Delayed Detached Eddy Simulation
JKR	Johnson, Kendall, and Roberts model
LES	Large Eddy Simulation
LIC	Line Integral Convolution
LPT	Lagrangian Particle Tracking
LSQ	Least Square
NWR	Near Wall Resolved
PhD	Doctor of Philosophy
PSD	Particle Size Distribution
$RANS$	Reynolds Averaged Navier-Stokes
RK	Runge Kutta
SA	Spallart-Allamaras
SDR	Specific Dissipation Rate
$SIMPLE$	Semi-Implicit Method for Pressure Linked Equations
SST	Shear Stress Transport
SVV	Spectral Vanishing Viscosity
TKE	Turbulent Kinetic Energy
$URANS$	Unsteady Reynolds Averaged Navier-Stokes
VCC	Volvo Cars Corporation
$WMLES$	Wall Modeled Large Eddy Simulation

Greek Letters

δ_{ij}	Kronecker's delta	
ν	Kinematic viscosity	$\mathrm{m^2\,s^{-1}}$

ν_t	Kinematic turbulent viscosity	$\mathrm{m^2\,s^{-1}}$
ω	Specific dissipation	
$\overline{u}$	Local Reynolds-averaged velocity	$\mathrm{m\,s^{-1}}$
σ_{ji}	Stress tensor	
τ_{ij}	Viscous stress tensor	
ε	Dissipation rate	
ζ	Normally distributed random number	
C_d	Drag Coefficient	
C_μ	Constant in turbulence model	
$C_{\varepsilon 1}, C_{\varepsilon 2}$	Constants in modelled ε equation	
E'	Effective Young's Modulus	
e_n	Coefficient of Restitution	
f_{IDDES}	IDDES blending function	
f_i	Force vector	
$K_{resolved}$	Resolved Turbulent Kinetic Energy	$\mathrm{kg\,m^2\,s^{-2}}$
K_{sgs}	Modeled Turbulent Kinetic Energy	$\mathrm{kg\,m^2\,s^{-2}}$
P^k	Production term	
S_{ij}	Strain rate tensor	
u'	Induced velocity fluctuation	$\mathrm{m\,s^{-1}}$
V_S	Critical sticking velocity	$\mathrm{m\,s^{-1}}$
v_i	Velocity vector	
W	Work of Adhesion	
x_i	Displacement vector	
μ	Dynamic Fluid Viscosity	
ρ	Density	$\mathrm{kg\,m^{-3}}$
σ	Stress	$\mathrm{kg\,m^{-1}\,s^{-2}}$
θ	Contact angle	$^\circ$

Roman Letters

f	Body force	$\mathrm{kg\,m\,s^{-2}}$
k	Turbulent kinetic energy	$\mathrm{kg\,m^2\,s^{-2}}$
p	Pressure	$\mathrm{kg\,m^{-1}\,s^{-2}}$
t	Time	s
v	Fluid velocity	$\mathrm{m\,s^{-1}}$
x	Displacement or Distance	m

Superscripts and Subscripts

$\langle\square\rangle'$	Instantaneous component
$\overline{\langle\square\rangle'}$	Time averaged instantaneous component
$\overline{\langle\square\rangle}$	Time averaged component

Contents

List of Figures

List of Tables

1

Introduction

The evolution of passenger safety in modern-day cars has transformed far from just passive safety system a few decades ago towards advanced active safety systems, which has significantly improved the level of safety. Technologies such as Advanced Driver Assistance Systems (ADAS) has been primary contributions in this regard which marks the future of transportation, Autonomous vehicles. ADAS includes devices such as radar sensors, laser scanners, cameras etc. Thereby, they offer automation assistance under various circumstances such a lane change assist, obstacle detection and so on. A lot of research and development has been going into this amongst many top-tier automobile companies, that including Volvo cars, which has been a trendsetter in passenger safety and innovation in driving.

However, contamination on normal road cars caused due to dust, dirt, snow, water, etc is quite common. The above-mentioned devices sometimes won't be able to function as expected because the sensor gets dirty due to accumulation of snow or dirt. Common problems such as rear parking sensors not being able to detect obstacles, rear lights of a car being blocked by packed snow that will not be seen by other drivers behind under extreme snow conditions is a major concern within traffic safety. Implementing effective solutions towards addressing such problems then becomes a necessity.

To resolve the above-seen issues, traditionally Volvo Car Corporation (VCC) makes use of field testing by driving on snowy roads and also climatic wind tunnel experiments. To simulate/re-create these tests on a computer, Computational Fluid Dynamics (CFD) models, especially Multiphase CFD models will be very helpful. The challenge arises in developing an accurate working model to predict snow contamination on cars or prototypes with the computational power and knowledge available at our disposal which results in reduced developmental cost and lead time.

Contamination and Core CFD department at VCC is conducting a PhD project together with the Chemical Engineering Department at the Chalmers University of Technology with the focus on snow adhesion on car exteriors. The project aim is to maintain the availability of active safety by the development of simulation models to predict snow impingement and snow accumulation on car sensors. Hence, the primary focus of this master thesis is to support this project by studying snow deposition through particle tracking methods.

1.1 Background

There are three different types of contamination of snow when a car is driving on snowy roads as described by Gaylard et al. [10]. They are natural contamination due to falling snow or water from the sky, self-contamination where the car's tyres pick off snow from the ground and contaminate itself and third-party contamination where contamination is caused by other cars picking up snow lying on the ground. Examples of these contaminations are shown in Figure 1.1 taken from [1].

Figure 1.1: Different types of snow contamination - self, contamination, third party contamination and natural contamination (drawn from Tobias et. al. [2020] [1])

Experiments in climatic wind tunnels and field testing on winter test tracks are usually the techniques used by the automotive industry to predict how the deposition and accumulation of snow occur on an automotive's exterior. However, both these are expensive and time-consuming. Repeatability in wind tunnel experiments are relatively better than that of field testing since it is often hard to test twice under similar conditions. Also, it is often the case that a virtual prototype is enough instead of a physical prototype in the earlier design stages. This is where Computational Fluid Dynamics (CFD) comes into the picture as it helps in developing simulation models which can predict the snow accumulation on cars with the help of optimal computational resources. It is possible to experience problems with repeatability in CFD simulations as well, but it is not as common as field testing or wind tunnel tests. The visual data obtained from wind tunnel experiments and field tests are used to validate the simulation results obtained from CFD in this masters' thesis.

A good amount of research has already been done in the area of snow contamination. CFD was used to run a simulation that tracks painted particles to visualise the hit points on a car's surface [11]. Vehicle soiling is caused due to rain and often the term "soiling" is mistaken for contamination due to soil. Hence, Hagemeier et al. came up with a new concept called Exterior Water Management (EWM) which investigates the contamination caused by water into the automotive industry [12]. To simulate droplet transport at the rear surface of an SUV, a model was developed using aerodynamics simulations in combination with Lagrangian Particle Tracking and also a thin film model was used to investigate surface water dynamics [10].

Three different approaches were evaluated by programming user-defined functions (UDF) which proved to describe snow packing on cars after having compared with the climatic wind tunnel experimental data and test track runs data from Northern

Sweden [8].

Irrespective of the CFD approach taken to investigate the contamination due to snow, build up of snow is a complex phenomenon and one needs to understand the different types of snow, it's properties and it's behaviour when it is interacting with the surface of the body under consideration. To bridge this gap, various experiments have been previously performed on different types of snow to understand their physical properties and characteristics [13] [14] [15]. Multi-phase approaches such as DEM modeling and fluid film approaches have been previously employed to study this phenomenon.

1.2 Purpose

This thesis aims at capturing the physical phenomena of snow adhesion on an exterior surface through multi-phase modeling. Lagrangian Particle Tracking will be the particle modeling approach that will be taken, coupled with a turbulent aerodynamic field to study the snow deposition pattern on the given geometries of interest. Finally, the simulation results will be verified by performing necessary experimentation and comparing the respective results with each other.

1.3 Objectives

- Perform a literature survey to understand the important underlying concepts in the field of multi-phase flows and to derive from them, necessary modeling assumptions and references/guidelines.
- Starting with an analysis of simple geometries initially by setting up a baseline aerodynamic simulation model by employing a suitable turbulent model relevant to this application.
- Perform multi-phase analysis to determine the snow deposition pattern by means of Lagrangian particle tracking.
- Perform relevant tests at the Volvo climate wind tunnel to study the pattern of snow deposition by recording the event(s) with necessary data.
- Compare the results from simulations and experimental data to verify the closeness of the results or to detect any anomalies between them.

1.4 Limitations

- The working temperature for both snow and the ambient flow field will be maintained at a temperature range of -15 °C or lower, throughout the project.
- Geometric consideration of snow particles will be limited to perfect spheres, for ease of simulation. Non-spherical snow particles shall be included at a later stage if time permits.
- The primary focus will be on capturing the pattern of snow accumulation and not on the development of accumulation for varying time.

- Concepts and related data needed to model the ice physics are primarily derived from given sources and no new concepts will be developed.
- Simulation models implemented will be based on the Lagrangian particle tracking technique only since other methods have proven to be computationally heavy for this application.

2

Theory

The main intention of this chapter is to convey to the reader with a fair idea of the key concepts and equations involved in Computational Fluid Dynamics (CFD) and Multi-phase flows. The theory discussed here includes the necessary description of the software and corresponding tools used in this thesis.

2.1 Governing Equations in CFD

For analysis of fluid flows at the macroscopic level where the length scales are considerably larger than the spacing between atoms, the molecular structure and molecular motions may be ignored. Hence, the fluid flow is described in terms of macroscopic properties such as velocity, pressure, density and temperature along with their space and time derivatives, being regarded as a continuum [16]. The fundamental governing equations of fluid flow are mainly based on the laws of conservation of mass and conservation of linear momentum [2]. For an incompressible flow, they follow the equations in the subsequent sections.

2.1.1 Continuity Equation

The continuity equation referred to as the *balance equation for mass* states that the rate of increase of mass in the fluid element is proportional to the net flow rate of mass into the fluid element. Mathematically, it is expressed as :

$$\frac{d\rho}{dt} + \rho \frac{\partial v_i}{\partial x_i} = 0 \tag{2.1}$$

where v_i is the fluid velocity vector along x-direction at time instant t, ρ is the density of the fluid. Density is varied over time considering the compressibility effects of the fluid. However, for lower Mach numbers ($Ma < 0.3$), compressibility effects can be neglected.

2.1.2 Momentum Equation

This is the second conservation equation which originates from the Newton$'$s second law of motion which states that $'$the rate of change of momentum is equal to the sum of all the forces acting along each direction$'$. The instantaneous form is given by:

$$\frac{\partial\left(\rho v_i\right)}{\partial t} + \frac{\partial\left(\rho v_i v_j\right)}{\partial x_j} = -\frac{\partial p}{\partial x_i} + \frac{\partial \tau_{ij}}{\partial x_j} + \rho f_i \tag{2.2}$$

where v_i and v_j are the velocity vectors, p is the pressure and f_i is the body acceleration.
From constitutive relationship for a Newtonian fluid, stress tensor(σ_{ji}) is given by:

$$\begin{aligned} \sigma_{ji} &= -P\delta_{ij} + \tau_{ij} \\ \tau_{ij} &= 2\mu S_{ij} - \frac{2}{3}\mu S_{kk}\delta_{ij} \end{aligned} \tag{2.3}$$

where τ_{ij} is the viscous stress tensor, μ is the dynamic fluid viscosity, S_{ij} is the strain rate tensor with δ_{ij} the Kronecker's delta.

Furthermore, with the assumption that fluid flow is incompressible (constant density), body acceleration (f_i) can be neglected and a Newtonian fluid with constant viscosity, we arrive at the Navier-Stokes equation or the transport equation for momentum which is given by:

$$\rho\frac{dv_i}{dt} = -\frac{\partial P}{\partial x_i} + \mu\frac{\partial^2 v_i}{\partial x_j \partial x_j} + \rho f_i \tag{2.4}$$

2.2 Basic Aerodynamics

Study of Aerodynamics is the interaction between any surface and the fluid flowing around it. So, the physical phenomenon here involves the analysis of the forces generated as a result of interaction between this surface and the fluid. For simple surfaces, it is rather easy to understand the interaction between them in case of steady flows. However, most of the flow in real world is turbulent by nature and the study of aerodynamics becomes more complex. Apart from the nature of fluid flow, a lot of other factors influence the outcomes of this interaction. Properties of the fluid such as density, viscosity, etc. on one hand while the properties of the interacting surface such as geometry, surface heterogeneities, etc. play a significant role [16]. For example, it is easier to swim through the water rather than to walk through it since the projection of the body in latter case experiences less resistance.

2.2.1 Boundary Layer Theory

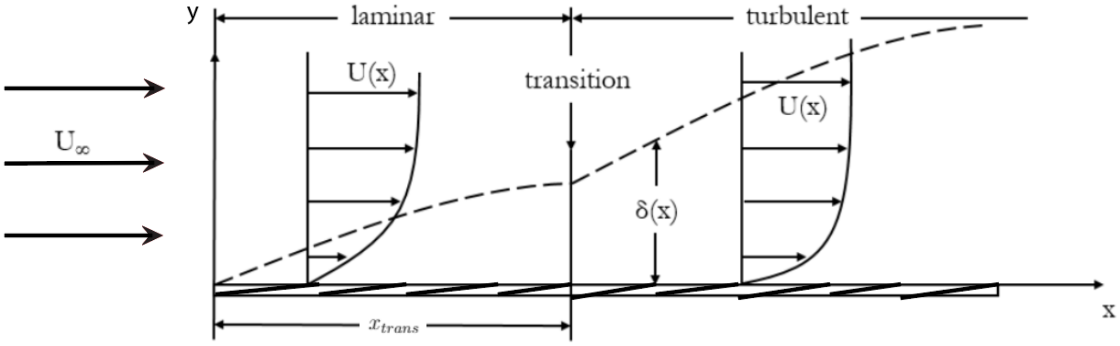

Figure 2.1: Flow over thin flat plate with boundary layer

Consider a flow over a thin flat plate as shown in Figure 2.1, where the U_∞ free stream velocity, $\delta(x)$ is the Boundary Layer (BL) thickness, shows the transition of fluid flow from laminar regime to turbulent regime. The immediate fluid layer above the surface experiences more stickiness compared to subsequent layer further above. This fluid layer is continuously developing and increases with increasing velocity. In the immediate vicinity of the surface its velocity equals zero, which is known as the *no-slip* condition. Progressing further away from the surface, a thin layer is formed. Hence, the immediate layer of fluid on the boundary which gives rise to viscous effects is called boundary layer (BL). In the near wall region, even though BL accounts for a very small portion , the fluid flow is still influenced largely by its presence.

In order to determine if the flow is laminar or turbulent, a dimensionless quantity known as Reynolds number is commonly used. It is given to be:

$$Re \ = \ \frac{\rho \ U_\infty \ L}{\mu} \tag{2.5}$$

where L is any characteristic length of the system and μ is the dynamic viscosity. Additionally, whether a flow is laminar or turbulent varies for external and internal flow applications. In context of this thesis, a Reynolds number of $5 * 10^5$ is taken as the critical value since the application considered here is an external flow [17].

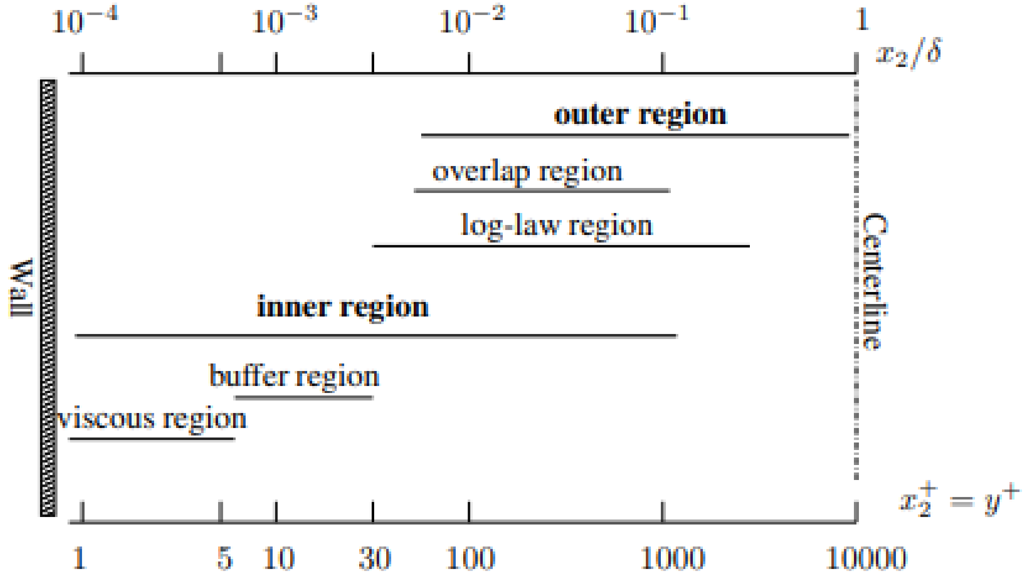

Figure 2.2: Schematic diagram of different wall regions (adapted from Davidson et. al [2])

Figure 2.2 describes the different regions of a wall boundary. The lower half is the viscous region and the upper half is the log-law region. The region between these two is the transition from viscous to turbulent effects thereby called as the buffer region. The topmost region is the outer region also called as inertial region. δ represents the half width of the channel and $y+$ represents the normalized wall distance [2].

There are two different types of conditions that influence formation of boundary layer - stationary and moving ground conditions. Under stationary condition, a relative velocity exists between the fluid and the surface resulting in the formation of the boundary layer, hence the ground is not moving. Whereas, in the moving ground condition, boundary layer is not formed due to negligible relative velocity. This is one of the most important parameters that should be considered which affect the aerodynamic behaviour such as aerodynamic forces and wake characteristics of the fluid flow around a body.

2.2.2 Wall Treatment

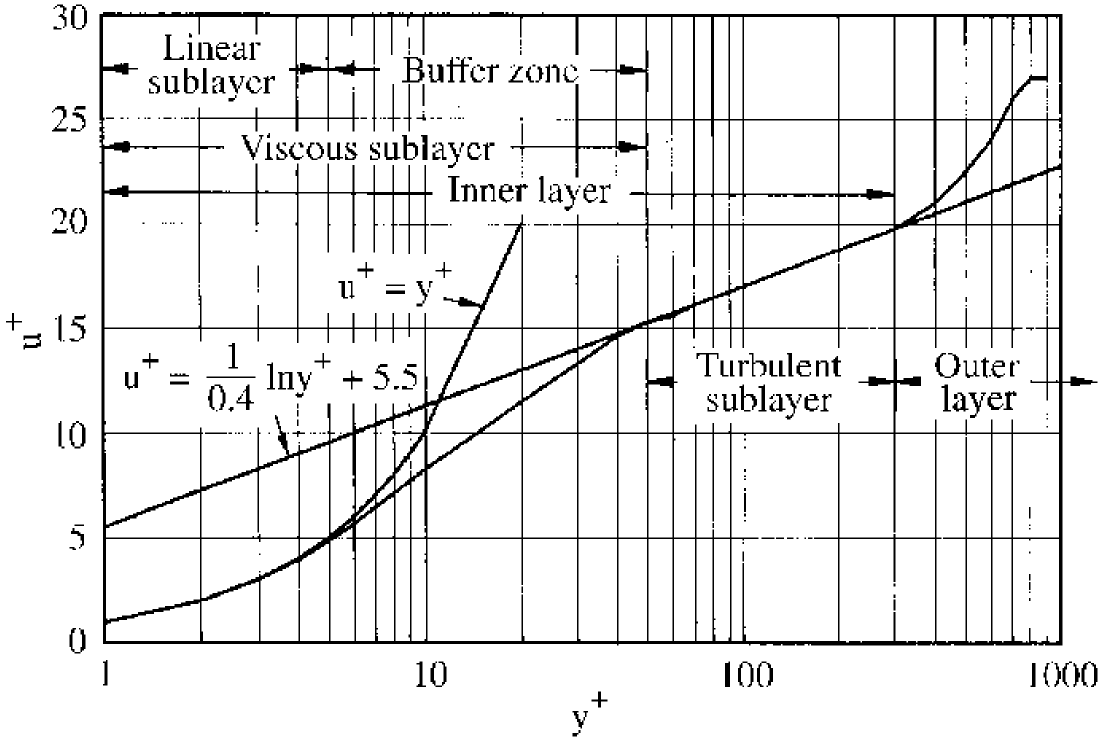

Figure 2.3: Law of the Wall (adapted from Cuhadarouglu et. al [3])

Figure 2.2 describes the Law of the Wall in fluid mechanics which states that "the average velocity of a turbulent flow at a certain point is proportional to the logarithm of the distance from that point to the "wall", or the boundary of the fluid region".

To further understand the boundary layer, it is categorized into smaller regions. This classification is made on the basis of the dimensionless wall distance (y+). This, together in relation with dimensionless velocity (u+) defines the Law of the Wall. y+ is given as:

$$y^+ = \frac{y u_\tau}{\nu} \tag{2.6}$$

where y is the absolute distance from the wall, u_τ = the friction velocity or shear velocity, ν is the kinematic viscosity [2]. Friction velocity (u_τ) is given as:

$$u_\tau = \sqrt{\frac{\tau_w}{\rho}} \tag{2.7}$$

where τ_w is the wall shear stress which is given by $\mu \frac{\partial v}{\partial y}$. The dimensionless velocity (u+) is given as:

$$u^+ = \frac{u}{u_\tau} \tag{2.8}$$

In essence, the absolute wall distance, fluid viscosity, fluid density and the corresponding wall shear stress have an effect on velocity of the fluid flow which is capitulated to be the Law of the Wall.

2.3 Simulation of Steady State and Transient Flows

CFD simulations can be performed using either a steady-state or a transient approach. A steady-state simulation solves for the flow field considering the time to be not advancing while unsteady/transient simulations are preferred in applications that involve physics that are time dependant. In common practice, a steady-state solution is used as an initial condition for unsteady simulation to ensure the flow field is properly initialized whereas unsteady simulations can be implemented either implicitly or explicitly. Implicit transient cases depend on unknown variables from the current time step, for which the system of equations needs to be solved simultaneously. Transient explicit cases, on the other hand, depends entirely on the variable values from the previous time step. In this thesis, the IDDES model being unsteady by nature follows an implicit unsteady method to solve for the fluid flow.

2.4 Turbulence Modeling

Most of the fluid flows we experience in daily life are turbulent by nature including the flow around cars. Turbulence is often characterized by random three dimensional flow of fluids and is visually chaotic. Turbulent flow occurs at higher Reynolds numbers due to hydrodynamic instabilities where the viscous forces are dominated by the inertial forces [16]. As a consequence, the velocity fluctuations are found to give rise to additional stresses on the fluid, the so-called *Reynolds stresses* which will be discussed in subsequent sections. The main categories of models used to solve these extra stress terms are discussed in this section. Various approaches towards capturing turbulence are available, that ranging from Direct Numerical Simulations (DNS) which resolves the entire flow to Large Eddy Simulations (LES) to Reynolds Averaged Navier Stokes (RANS) approach which entirely models turbulence. In context of this thesis, Improved Delayed Detached Eddy Simulation (IDDES) approach is considered which employs both modeling approach (RANS) and to some extent resolving approach (LES).

2.4.1 Reynolds Averaged Navier Stokes Equation

Random nature of the turbulent flows is characterized by the mean values and the fluctuating values of the flow properties. This concept is derived from the classical Reynolds decomposition theorem [2]. For instance, the velocity term can be divided into $v_i = \bar{v}_i + v_i'$, where the first term is the Reynolds time-averaged term and the second term being the instantaneous term.

When the equation (2.4) is time averaged and after simplification, it yields the Reynolds Averaged Navier-Stokes (RANS) equation:

$$\frac{\partial \overline{\rho u_i}}{\partial t} + \bar{u}_j \frac{\partial \overline{\rho u_i}}{\partial x_j} = \frac{\partial}{\partial x_j}\left[-\frac{\partial \bar{p}\delta_{ij}}{\partial x_i} + \mu\left(\frac{\partial \bar{u}_i}{\partial x_j} + \frac{\partial \bar{u}_j}{\partial x_i}\right) - \rho\overline{u_i' u_j'}\right] \tag{2.9}$$

The last term in the equation (2.1) is the momentum transport due to turbulence, commonly referred to as the *Reynolds stress* term. This term often requires additional modeling and an accurate way is to solve a transport equation for thee unknown turbulent stresses. This is commonly referred to as the closure problem [2]. Various two equation eddy-viscosity models such Spallart-Allamaras (SA) turbulence model, k - ε model, k - ω model and more has been previously suggested [16]. But in the context of this thesis, we employ the SST-Menter k - ω model for the same.

2.4.2 Two-Equation Models: $k - \omega$ (SST Menter) Model

$k - \omega$ model is a two-equation eddy-viscosity model where two transport equations for turbulent kinetic energy 'k' and specific dissipation rate ω are solved. The major advantages of this model are its enhanced predictability of shear stresses at the boundary layers in adverse pressure gradient flows and the necessity of a separate wall function can be ignored.

Shear Stress Transport model is also an eddy-viscosity model that blends well between both the k - ε model and k - ω model. It inhabits two benefits:

1. It employs k - ω model at the inner boundary layer and k - ε model at the outer boundary layer, thereby eliminating the need for near-wall modification.
2. It contains a shear stress limiter that helps predict lower shear stress in adverse pressure gradient regions.

The transport equation for 'k' is given as:

$$\frac{\partial(\rho k)}{\partial t} + \frac{\partial\left(\rho U_j k\right)}{\partial x_j} = \frac{\partial}{\partial x_j}\left[\left(\mu + \frac{\mu_t}{\sigma_k}\right)\frac{\partial k}{\partial x_j}\right] + P_k - \beta^* \rho k \omega \tag{2.10}$$

Similarly, the transport equation for ω is given as:

$$\frac{\partial(\rho\omega)}{\partial t} + \frac{\partial\left(\rho\omega U_j\right)}{\partial x_j} = \frac{\partial}{\partial x_j}\left[\left(\mu + \frac{\mu_t}{\sigma_{\omega,1}}\right)\frac{\partial\omega}{\partial x_j}\right] + \gamma_2\left(2\rho S_{ij}S_{ij} - \frac{2}{3}\rho\omega\frac{\partial U_i}{x_j}\delta_{ij}\right) - \beta_2\rho\omega^2 + 2\frac{\rho}{\sigma_{\omega,2}\omega}\frac{\partial k}{\partial x_j}\frac{\partial\omega}{\partial x_j} \quad (2.11)$$

where the last term on the right hand side is the cross-diffusion term, which arises during the $\varepsilon = k\omega$ transformation of the diffusion term in the ε-equation [16].

2.4.3 Scale-Resolving Models

In comparison to the RANS models where turbulence is mostly modeled, scale-resolving models resolve the large scales of turbulence and model the smaller ones. Two popular approaches are Large Eddy Simulations (LES) and Detached Eddy Simulations (DES). LES is an inherently transient technique which resolves various turbulent structures up until the smallest grid size and uses Sub-grid scale models to approximate the sub-grid sized turbulent structures [2]. In this approach, the equations solved are obtained by spatial filtering of any solution variable (ϕ) rather than time-averaging like in RANS. Solution variable is further decomposed into a filtered value and a sub-grid value.

In particular, this approach requires excessively fine mesh resolution in the wall-boundary region, wall-parallel and wall-normal directions. Because near the walls, the spatial scales of the “large” turbulent eddies which should be resolved by LES are small in reality. Also, these spatial scales become much smaller for increasing Reynolds numbers. This makes it computationally very expensive due to the very high cell count. Instead, a Hybrid LES-RANS approach (Detached Eddy Simulation) is a much suitable approach to overcome the aforementioned problem. Here, the turbulence is modeled using RANS in the near-wall region while the larger structures are resolved using LES.

The transport equation from RANS and LES can now be written as:

$$\frac{\partial\bar{v}_i}{\partial t} + \frac{\partial\bar{v}_i\bar{v}_j}{\partial x_j} = -\frac{1}{\rho}\frac{\partial\bar{p}}{\partial x_i} + \frac{\partial}{\partial x_j}\left(\left(\nu + \nu_T\right)\frac{\partial\bar{v}_i}{\partial x_j}\right) \quad (2.12)$$

Close to the walls, RANS turbulence models is used for the turbulent viscosity (i.e. $\nu_T = \nu_t$) [frmenter] and away from the walls LES turbulence model is employed (i.e. $\nu_T = \nu_{sgs}$). One has to note that the concept of averaging as in RANS is not the same in LES. The former averages the instantaneous quantities over time while the later volume averages the quantities. The solution being unsteady, the time dependence term (first term in equation 2.12) is retained and hence the model now operates in URANS mode in the near-wall region while it operates in LES mode away from the wall. An important element in DES simulations is when should the solver switch between RANS and LES modes. It is often seen that the grid size determines the location of the switch between the above-said modes. Particularly, a

DES modification means to switch between the turbulent length scales from a RANS length scale ($\alpha \ \frac{k^{(\frac{1}{2})}}{\omega}$) to that of LES when the grid is sufficiently fine.

The DES modification is applied to the SST model (equation 2.12) in the k-equation and is given as follows:

$$\rho\varepsilon = \beta^{*}\rho k\omega \rightarrow \beta^{*}\rho k\omega \cdot F_{DES} \quad \text{with} \quad F_{DES} = \max\left(\frac{L_t}{C_{DES}\Delta}, 1\right) \tag{2.13}$$

where ε is the dissipation rate, Δ is the maximum local grid sizing ($\Delta = \max(\Delta x, \Delta y, \Delta z)$), β^{*} is a constant, $C_{DES} = 0.61$ and L_t is the turbulent length scale.

It is often that for fine grids, the switch from RANS to DES mode occurs within the boundary layer and can hence produce a grid-induced separation. During this scenario, the grid sizes along the stream-wise direction and span-wise direction are smaller than the thickness of the boundary layer ($\Delta < \delta$). This may cause the turbulence model to switch prematurely thereby resolving the boundary layer using LES and leading to an inaccurate prediction [18]. To avoid this problem, multiple approaches have been made of which, Delayed Detached Eddy Simulation (DDES) model poses to be a better solution [18] [2]. Importantly, the blending function in equation 2.13 is modified in DDES and it reads:

$$F_{DDES} = \max\left\{\frac{L_t}{C_{DES}\Delta}\left(1 - F_S\right), 1\right\} \tag{2.14}$$

where F_S is the generic DES shielding function.

A much later development of the DDES model is the Improved Delayed Detached Eddy Simulation (IDDES) model which is currently employed in this thesis [19]. This model aims to combine DDES with an improved hybrid RANS-LES model, the Wall Modelled LES (WMLES) ensures a different response depending on whether the simulation consists of an inflow of turbulent content at the inlet. If there exists any turbulent content at the inlet, it reduces to WMLES. meaning, most of the turbulence is resolved except near the wall. A novel highlight of this model is that it accounts for subgrid length-scale which depends not only on the grid spacing but also on the wall distance. In case there is no inflow turbulent content, the proposed model performs as DDES (pure RANS solution for attached flows and a DES solution for massively separated flows) else switches to WMLES mode. The coordination between the two modes is carried out by a blending function (IDDES Blending function) which, in later sections, is also used to evaluate the meshing. The length scale in DDES model is given as:

$$L_{DDES} = L_{RANS} - f_d \min\left(0, L_{RANS} - L_{LES}\right) \tag{2.15}$$

where f_d is a generic DES shielding function. Equation 2.15 in IDDES, is further modified as:

$$L_{IDDES} = \tilde{f}_d\left(1 + f_e\right)L_{RANS} + \left(1 - \tilde{f}_d\right)L_{DES} \tag{2.16}$$

where the LES length scale, like discussed previously, is inclusive of wall distance also ($\Delta = \min\left[C_\omega \max\left[d, h_{\max}\right], h_{\max}\right]$) with h_{max} being the max. edge height of the cell of interest[shur].

2.5 Overview on Multiphase Flows

A fluid phase generally refers to the thermodynamic state, solid, liquid or vapour, of the matter. A phase could also be referred to as liquids or gases of different density, droplets of a different size or solid particles of different shapes. A phase can hence be defined as the solid, liquid or vapour state of the matter rather than its molecular components and signified by an interface separating the states [20]. Multiphase flow covers a wide range of problems, including suspended grain dust or coal dust, droplets and sprays, propellant burning, charring, soot, smoke formation, slurries, bubbles in liquids, rain, and sedimentation [21].

Multiphase flows in general, are classified into two subdivisions. They are *stratified flows* and *dispersed flows.* Also, a multiphase flow can either be a *single-component flow* or *multi-component flow.* For example, steam-water flow is a classic example of single-component multiphase flow while air-water or slurry flow is a classic example of multi-component multiphase flow. A phase is continuous if there are no additional phase boundaries between two points in a fluid domain while they are classified as dispersed flows if vice-versa.

Furthermore, dispersed phase flows are mainly classified into four categories: liquid-solid flows, gas-liquid flows, gas-solid flows and three-phase flows [4]. However, gas-solid flows will be our subject of interest in the context of this thesis with air to be the continuous phase and snow (solid particles) to be the dispersed phase.

2.5.1 Euler-Lagrangian Framework

Consider a fluid motion in a continuum. The motion of the fluid particle can be studied in two ways: Lagrangian frame of approach or Eulerian frame of approach. The former keeps the track of a particle starting from an initial position, at every subsequent instant of time while in the latter approach, a fixed position/ frame of reference is initially chosen and movement of a particle is observed as it passes by that point [2].

In the context of this thesis, we make use of the Euler-Lagrangian framework to account for tracking of snow particles within an aerodynamic field. The continuity and momentum equations are solved for the air mixture (Eulerian phase) while Newton's second law of motion is employed to account for the particle motion (Dispersed phase).

Typically, a Lagrangian frame of reference is used to describe the evolution of individual particles as they travel through the given domain. The trajectory equations are based on the movement of an individual particle. This thesis mainly revolves around the understanding that the exterior contamination on cars can be best analysed by considering snow particles as dispersed particles injected into a turbulent carrier flow field as computational parcels. Later, the trajectory of each parcel can be tracked using the Lagrangian Particle Tracking (LPT) approach.

2.5.2 Multiphase Coupling

Coupling between the continuous phase and the dispersed phase is an important concept in the analysis of multiphase flows. Generally, the coupling between phases takes place through the source terms in the governing equations of the fluid [4]. Coupling between phases, in a sense, also means that the dispersed phase may or may not influence the continuous phase. The system is said to be *one-way coupled* when dispersed (Lagrangian) phase is affected by the Eulerian phase but the latter is not affected back by the former. On the contrary, if both the continuous phase and the dispersed phase are mutually affected by each other then the system is said to be *two-way coupled* [4]. Figure 2.4 depicts the schematic of coupling between phases where the carrier phase and the dispersed phase represented by their respective field parameters are inter-related through the governing equations of the fluid.

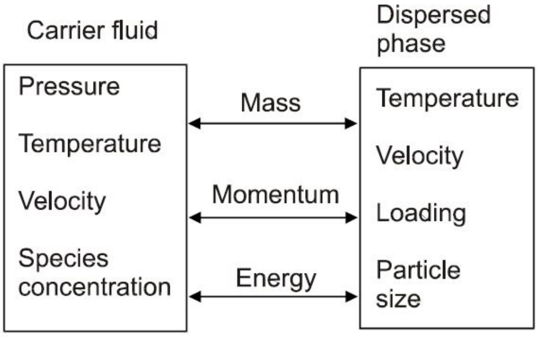

Figure 2.4: Schematic diagram of multiphase coupling [4]

Choice of coupling has a significant impact on the end solution and hence it becomes necessary to decide if the phases are one-way coupled or two-way coupled. For dilute flows with a low density of particles, the one-way coupling may be a good assumption whereas for flows with a significantly high density of particles, the effect of particles on the carrier field is no more negligible and hence they must be two-way coupled.

2.5.3 Lagrangian Particle Tracking

Processes which include a large number of diameter classes or a broad distribution of states can often be more easily modelled using a Lagrangian framework approach [22]. In the case of laminar flows, each particle released from a point follows a smooth unique trajectory. Whereas if particles are released to a turbulent flow in the carrier phase, every particle takes its random path due to interaction with the fluctuating turbulent velocity field.

As a consequence of particle-particle or particle-wall interaction produced by fluid-dynamic forces acting on the dispersed particles, it causes them to break up into

smaller particles. On the contrary, collisions between particles can also produce the opposite effect where there is an increase in size due to coalescence or formation of agglomerates. When dispersed particles hit a wall/boundary, it could either result in the particle sticking to the wall, bouncing from the wall or escaping the collision depending on the impact conditions [22].
Include Illustration for particle boundary conditions.

One of the objectives of this thesis is to study the behaviour of particles when subjected to different boundary conditions and for varying diameter classes of particles.

2.5.3.1 Governing Equations of Particle Motion

In the Lagrangian framework, the field properties (position, velocity, acceleration) associated with a particular particle are solved for. Various forces acting on the particle are modeled and the equation of motion is solved individually for each particle or parcel (see Section 2.5.3.2) to update its position step-wise [23].

The first analytic solution for the flow around a sphere at low Reynolds numbers (the order of unity or less) in a uniform, the steady flow was provided by Stokes in 1851 [24]. For an incompressible unbounded flow with a translational velocity of particles (assumed to be small spheres) and a slow variation of characteristics, the particle trajectory equation is given as [25] :

$$\sum \vec{F_i} = m_p \frac{\hat{d}\vec{v}_p}{\hat{d}t} \tag{2.17}$$

where $\sum \vec{F_i}$ is the net force acting on the body. Equation 2.10 can be further written as:

$$m_p \frac{\hat{d}\vec{v}_p}{\hat{d}t} = \sum \vec{F}_{\text{body}} + \sum \vec{F}_{\text{surface}} + \sum \vec{F}_{\text{interaction}} \tag{2.18}$$

where $\sum \vec{F}_{\text{body}}$, $\sum \vec{F}_{\text{surface}}$ and $\sum \vec{F}_{\text{interaction}}$ are the resultant of body forces, resultant of forces acting on the particle surface and resultant of forces due to particle interaction respectively. Each of the resultant forces are constitutive of the following forces:

$$\begin{aligned} \sum \vec{F}_{\text{Body}} &= \vec{F}_{\text{Buoyancy}} + \vec{F}_{VM} \\ \sum \vec{F}_{\text{Surface}} &= \vec{F}_D + \vec{F}_{\text{Pressure}} + \vec{F}_{\text{Basset}} + \vec{F}_{\text{Saffman}} + \vec{F}_{\text{Magnus}} \\ S\vec{F}_{\text{Interaction}} &= \vec{F}_{BM} + \vec{F}_{\text{Particle-particle}} + \vec{F}_{\text{Particle - wall}} \end{aligned} \tag{2.19}$$

Important to note that the forces considered to be relevant to this context will alone be discussed in detail within this section.

Body Forces: Gravity is the most common body force which is the product of the particle mass and the vector representing the acceleration due to gravity. But there are other body forces which becomes important depending on the application such as Buoyancy force, Virtual mass force, Coulomb force and Thermophoretic force [4].

Surface Forces: Surface forces acting on a particle are mainly influenced by particle drag forces and particle lift forces and pressure gradient forces [4].

Drag Force ($\vec{F}_{\mathbf{Drag}}$) : Drag Force is the force induced due to the difference between the velocities of the carrier phase and the particle. For a spherical particle in a uniform Newtonian fluid flow, the drag force is expressed as:

$$\vec{F}_D = \frac{1}{2} C_D \frac{\pi d_p^2}{4} \rho_f \left(\vec{v}_p - \vec{v}_f\right) \left|\vec{v}_p - \vec{v}_f\right| \tag{2.20}$$

where C_D is the drag coefficient of the particle, ρ_f is the density of the particle, $\vec{v}_p - \vec{v}_f$ is the slip velocity with $\vec{v}_p$ being the particle velocity and $\vec{v}_f$ being the velocity of the fluid.

The drag coefficient C_D is dependant on the small-scale flow features around a given particle. Hence, it is often determined through correlations from experimental or theoretical studies. Few of the most commonly referred correlations include *Schiller-Naumann correlation*, *Liu dynamic drag coefficient* and *Haider and Levenspeil drag coefficient.*

Importantly, factors such as nature of the dispersed phase, shape of the particle, inter-phase mass and energy transfer influences the choice of correlations [22]. The *Schiller-Naumann correlation* being the most suited one for spherical snow particles, has been chosen in the light of this thesis.

Pressure Gradient Force ($\vec{F}_{\mathbf{Pressure}}$): It is a force along the direction of the pressure gradient which is a resultant of the local pressure distribution. This force becomes predominant for increasing Reynolds number flows [25]. It is computed as:

$$\vec{F}_{\text{Pressure}} = \frac{\pi}{6} d_p^3 \nabla p \tag{2.21}$$

Where d_p is the diameter of the particle and ∇p is the pressure gradient.

Lift Forces: Particle Lift forces are primarily due to the pressure distribution developed on a particle in a velocity gradient. A higher velocity on one side of the particle gives rise to a low pressure while the high pressure on the low velocity side gives rise to a lift force. This is called the Saffman lift force. A lift is caused by a pressure differential between both sides of the particle resulting from the velocity differential due to rotation. So, Particle lift forces due to the rotation of particles is known as the Magnus force [4]. Mathematically, they are expressed as:

$$F_{\text{Saff}} = 1.61 \mu_c D \left|u_i - v_i\right| \sqrt{Re_G} \tag{2.22}$$

$$F_{\text{Mag},i} = \frac{\pi}{8} D^3 \rho_c \left[\varepsilon_{ijk} \omega_{d,j} \left(v_k - u_k\right)\right] \tag{2.23}$$

History/Basset Force: This force accounts for the temporal delay in boundary layer development as the relative velocity changes with time. Sometimes, this force is also called the *history term.* It is called the history force as it depends on how the particle has behaved up to a particular time instant.

Particle–Particle Interaction Forces: Particle–particle interaction forces are necessary to be considered for dense particle suspensions. Hard sphere model and soft sphere model are the two models which are widely used for numerical simulations [25].

2.5.3.2 Concept of Parcels

When analysing particle flow within a domain, it is easy to track the properties of the given particle at each point by solving for the equations of motion of that particle. But as the number of particles increases in the domain, it becomes computationally expensive and time-consuming to track every single particle Instead, a cloud of particles or commonly referred to as 'parcels' is simulated to save both time and expense. Particles with identical properties are grouped into parcels such that the dynamics of a parcel represents the behaviour of all the particles it represents [22].

It is also important that the number of particles in a parcel must be large enough such that the properties of the entire population of particles are well represented. Also, the number of parcels in the simulation as a whole must be large enough to represent the properties of the full population of particles.

2.6 Brief Overview of Snow

2.6.1 Formation of Snow

The Nakaya snow crystal diagram as shown in Figure 2.5 describes how the snow is formed and the factors affecting its formation studied by physicist Ukichiro Nakaya [5]. As seen in the figure, the morphology of snow crystals has a complex dependence on the temperature and water vapour supersaturation density. Plates are formed at a temperature range of 0 to $-2°C$, prism-like shapes to sheath and needles with an increase in supersaturation around $-5°C$. Thick plates to dendrite shaped structures are formed as we go lower in temperature. With temperatures lower than $-25°C$, prisms are observed in low supersaturation while columns are observed in higher supersaturation.

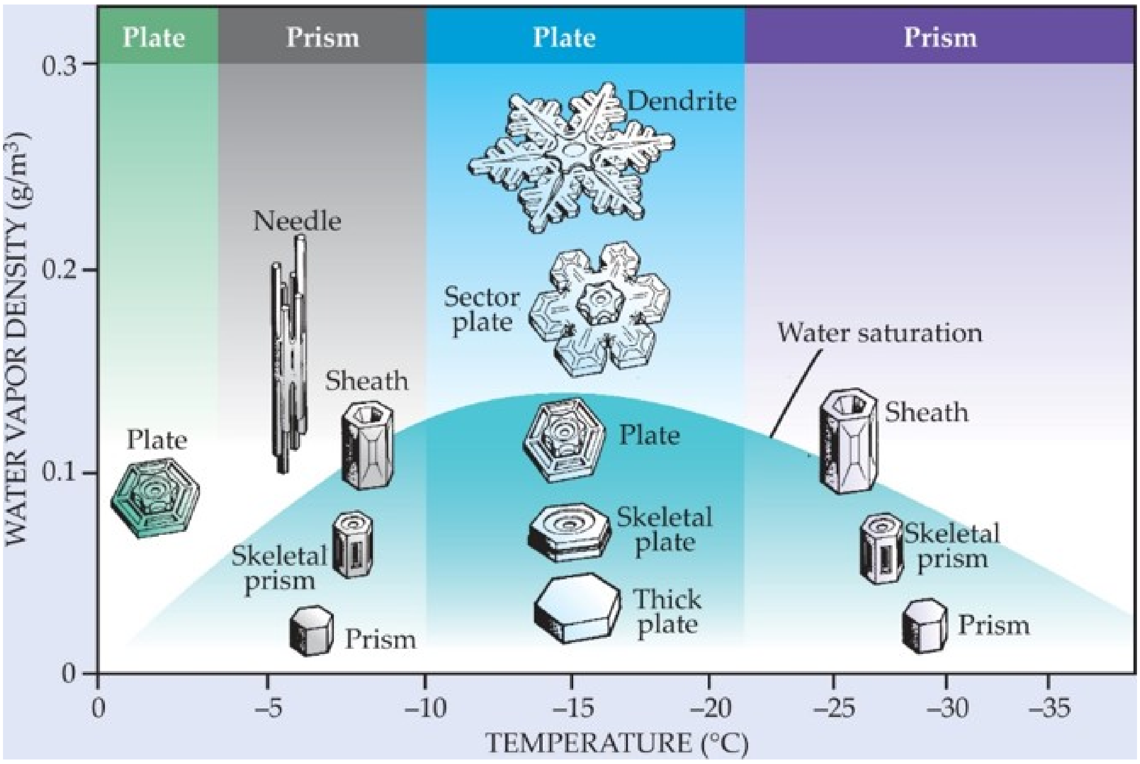

Figure 2.5: Nakaya snow crystal morphology diagram depicting snow crystal growth based on temperature gradient and water vapor supersaturation density [5]

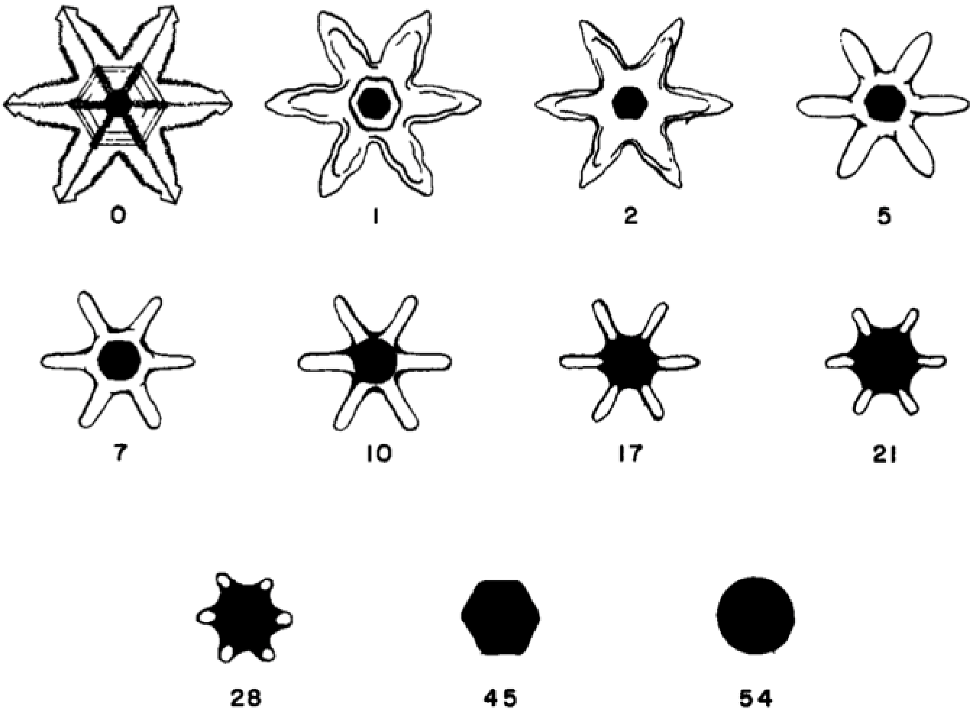

Figure 2.6: An overview of seasonal snow metamorphism without temperature gradient [6]

Bader et al. observed the seasonal snow metamorphism in Figure 2.6 which took longer time than natural scenario since it was conducted in idealised conditions with no temperature gradients [6]. In natural scenarios such as that on a road, the metamorphism is fast and sensitive due to the movement of cars and trucks which break down the snow lying on the ground.

Hexagonal and spherical grains are the two common structures of snow that can be seen. But the structure of this is dependant on various factors, such as how long has the snow been lying on the ground, the temperature difference of snow and also the amount of water or moisture present in the snow due to the temperature difference. But the most common type of snowflake is of hexagonal shape on a thin plate [5] [26] [27]. In this thesis however, morphological age of snow grains are considered to be old enough. Thereby, spherical shaped grains are considered which also aids in reducing modeling complexity.

2.6.2 Types and Characteristics of Snow

Snow can be categorized into mainly two types, namely: natural and artificial snow. Natural snow is created by the natural transpiration by nature while artificial snow is man-made snow which is very often seen in wind tunnels of industries. Natural snow is further categorized into falling snow and untouched snow on the ground. Field studies have been performed by VCC on test tracks covered in snow in Northern Sweden to understand how contamination occurs on cars due to falling snow and untouched snow on the ground.

Various layers of snow accumulate to form a snowpack due to irregular precipitation, movement of wind and the non-stop metamorphism. These layers are different to one another due to one of the following characteristics: microstructure, grain shape, grain size, snow density, snow hardness, liquid water content, snow temperature, impurities and layer thickness. Grain size must be regarded as a property of one of the layers of snowpack and not of the grain shape. Grain sizes vary from lesser than $0.2mm$ to greater than $5mm$. Snow can be classified into dry, moist, wet, very wet and soaked snow based on the amount of liquid water content present in the snowpack. Machine-made snow is formed by a physical process where small water droplets are frozen from the surface inward or by crushing the ice. They are usually spherical with projections or ice plate-like structures [28].

2.7 Particle-wall Modeling of Snow Particles

One of the important properties of snow is that it adheres to surfaces and tend to accumulate on them eventually [15]. Avid amount of research is being done within powder technology, to understand the energy dissipation during collisions between ice particles and surfaces [14]. This is thus an important part of understanding on how actually snow or ice accumulates onto surfaces. A standard metric to measure this is given by the coefficient of restitution (e_n) which determines the elastic properties of the . It is defined to be the ratio of rebound velocity(V_r) of the particle to its impact velocity(V_i) which as expressed as [13]:

$$e_n = \frac{V_r}{V_i} \tag{2.24}$$

2.7.1 Factors Affecting the Adhesion of Snow

Significant work has been performed in [29], [15] and [7] previously that account for the adhesive interaction of spherical particles due to Van der Waals forces. Results from this work has been used for the particle tracking model in this thesis which is coupled with external aerodynamic simulations to predict the accumulation of snow on bluff bodies more accurately . Few important factors affecting the adhesion of snow include the following:

2.7.1.1 Effect of Van Der Waals Force

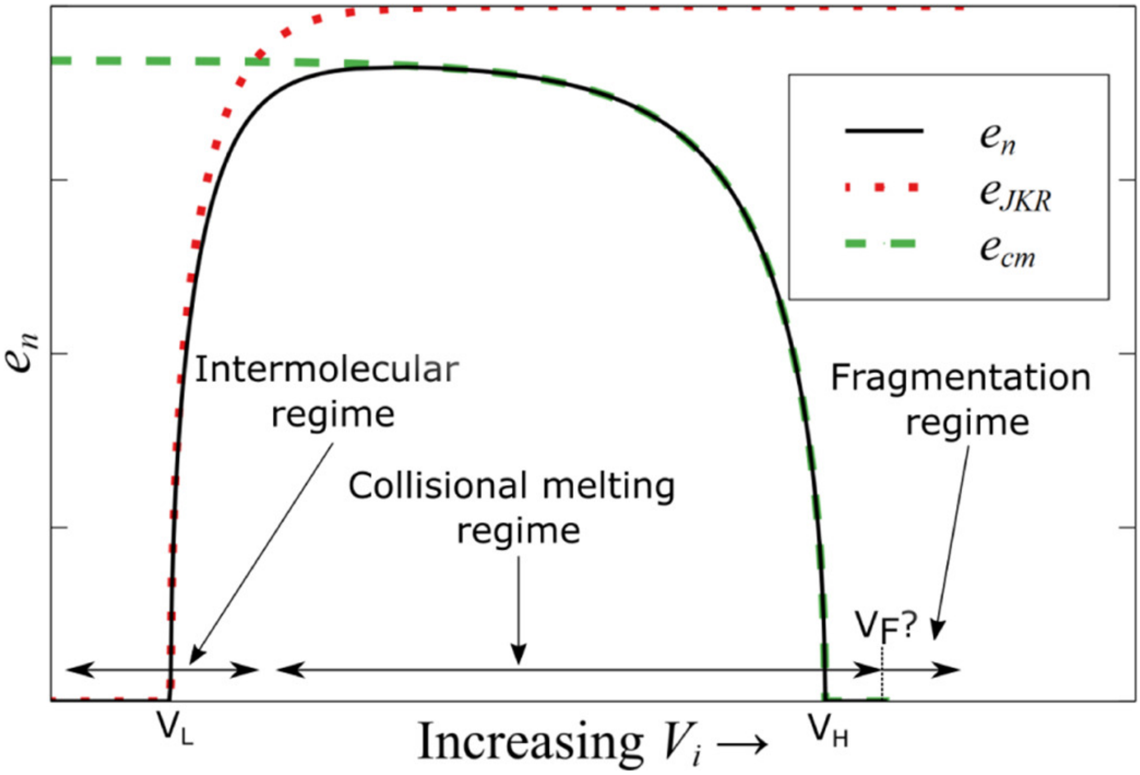

Figure 2.7: Regime map for coefficient of restitution of ice particles.(Adopted from Eidevåg et al. [7])

Inter-particle forces such as Van der Waal forces, play a key role in adhesion as well as in the formation and breakage of agglomerates of particles. Previous experiments and studies have proposed the usage regime map for ice collisions based on the Johnson-Kendall-Roberts (JKR) model for the same [15]. This model describes three different regimes for ice particle collisions, namely, an intermolecular adhesive regime, a collisional melting regime, and a fragmentation regime. Figure 2.7 shows the regime map of the coefficient of restitution for increasing impact velocity. The intermolecular adhesive regime is characterized by damping due to intermolecular forces and ice particles colliding with a surface will have a rapid increase in energy loss for increasing V_i until the particle begins to adhere to the surface. Collisional melting of ice is not expected since the velocities are well below the critical velocities for the particle studied in this work. Hence, intermolecular adhesive regime would be the sole area of interest in the context of this thesis.

The model involves contact mechanics in the normal and tangential directions. Single particles, as well as agglomerates, are simulated to impact with walls of four different material types. The particles sizes are based on experimental measurements performed on test tracks in northern Sweden.

At low impact velocities, coefficient of restitution is defined as:

$$e_n \ = \ \sqrt{1 - (\frac{V_S}{V_i})^2} \tag{2.25}$$

Where e_n is the coefficient of restitution, V_i is the velocity at impact (collisional velocity) and V_S is the critical sticking velocity below which particles will stick due to intermolecular adhesion, where V_S is given as:

$$V_S = \frac{3\sqrt{3}}{4}\sqrt{\frac{K_1}{\rho_s}}\left(\frac{\pi^2 W^5}{R^5 E^{*2}}\right)^{\frac{1}{6}} \tag{2.26}$$

With $K_1 \approx 0.9355$ is an integration constant, E^* is the effective Young's modulus, W is the work of adhesion and R is the radius of the particle. In reality, snow buildup occurs upon an initial ice layer formation on any wall/surface. Hence, $W = 0.218$ and $E^* = 5.4$ $[GPa]$ is chosen [15], which corresponds to ice.

It is also evident from the above equation that e_n is dependant on both the impact velocity and size of the particle. Hence, it is important to determine appropriate values for e_n corresponding to the chosen particle size distribution.

2.7.1.2 Choice of Collisional Damping Regime

From Figure 2.7, it is seen that the velocity dependence of e_n distinguishes between three different collisional damping regimes. The velocity dependence of e_n is mainly classified into Quasi-elastic and inelastic regimes respectively. Quasi-elastic regime corresponds to the understanding that collisional behaviour of a particle is not exactly elastic (i.e. Unity), $V_i < V_s$ and no fragmentation or plastic deformation is observed [13]. It is observed from experiments conducted by [13] that the coefficient of restitution due to quasi-elastic damping (e_{qe}) is dependant on particle size under consideration with a variation ranging between 0.71 - 0.95.

2.7.1.3 Particle Re-suspension Modeling

Particle re-suspension or particle re-entrainment corresponds to the process where particles adhering on to a surface are re-entrained or suspended away from the surface [30]. In the context of this thesis, approach taken towards treatment of particle re-suspension is based on a threshold value of particle Reynolds number for a given PSD (Refer Section 3.2.6.5).

2.8 Analysis of Bluff Bodies

It is often that high resolution of geometric details within less relevant areas contribute towards unexpected problems or complexities in analysis. Hence, a wise alternative would be to choose a simple geometry which mitigates the risk of unprecedented errors during analysis as well as displays good resemblance with the parent geometry (car model in this case). Such a geometry is commonly known as a bluff body. In this thesis, two different bluff bodies are chosen for investigation.

2.8.1 The Wedge

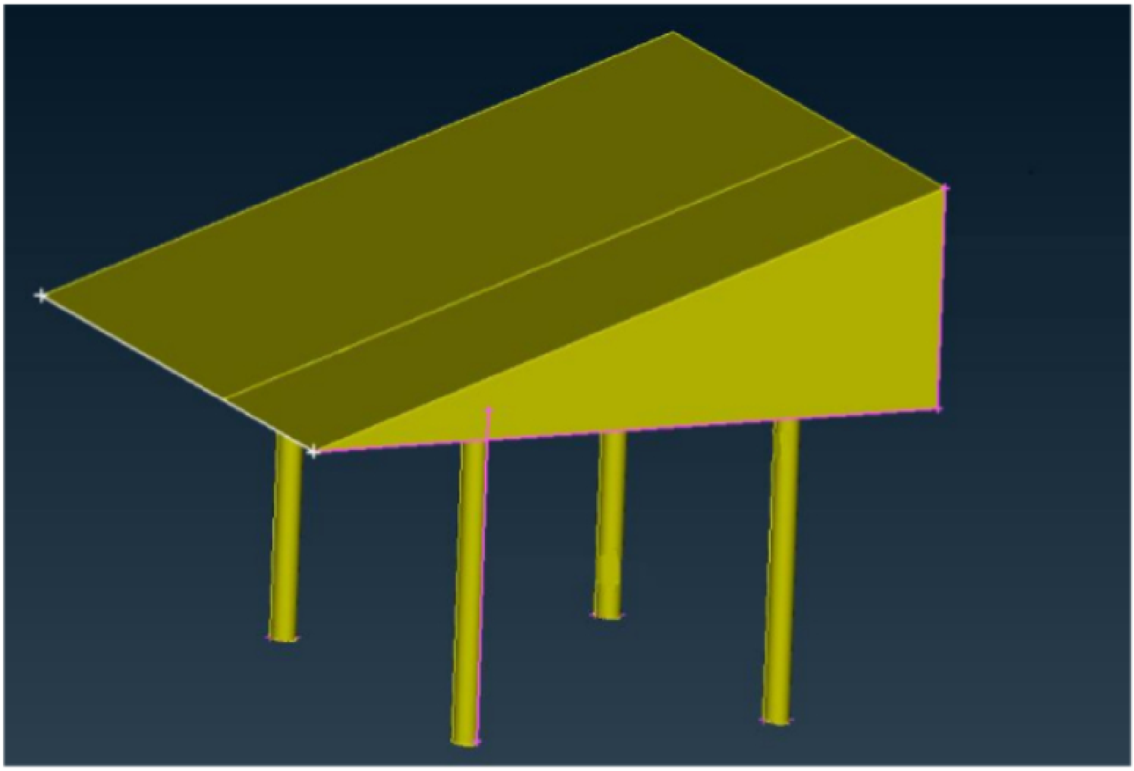

Figure 2.8: CAD geometry of the Wedge (Adopted from Enmark et al. [8])

Wedge is a classical utility that has been previously used to understand the aerodynamic flow and behaviour of snow deposition over an external surface in terms of both, wind tunnel testing and CFD simulations. Various works in this regard, comprising of different modeling approaches have been studied previously. One such work having performed analysis over the Wedge can be referred back to Enmark et al. [8]. Figure 2.8, shows the geometric description of the Wedge. This geometry has proven to give a fair understanding of different aerodynamic features over an external flow and resultant snow deposition depending upon the modeling approach considered. It has also been used as the starting point for this thesis to learn about the different aspects of aerodynamic flow and to analyse snow deposition further on.

2.8.2 Ahmed Body

To assess the snow deposition pattern on a real car, conducting a study on something that exhibits the essential features of a standard automobile design without rotating wheels, surface projections, interior compartment and the such is important [31]. The Ahmed body is a better suiting alternative when compared to the Wedge, although challenging due to the formation of complex turbulent structures such as the re-circulation region resulting from the combination of strong separation and a pair of counter-rotating vortices to name a few. Figure 2.9 shows the geometry of the Ahmed body with the table designed in Catia.

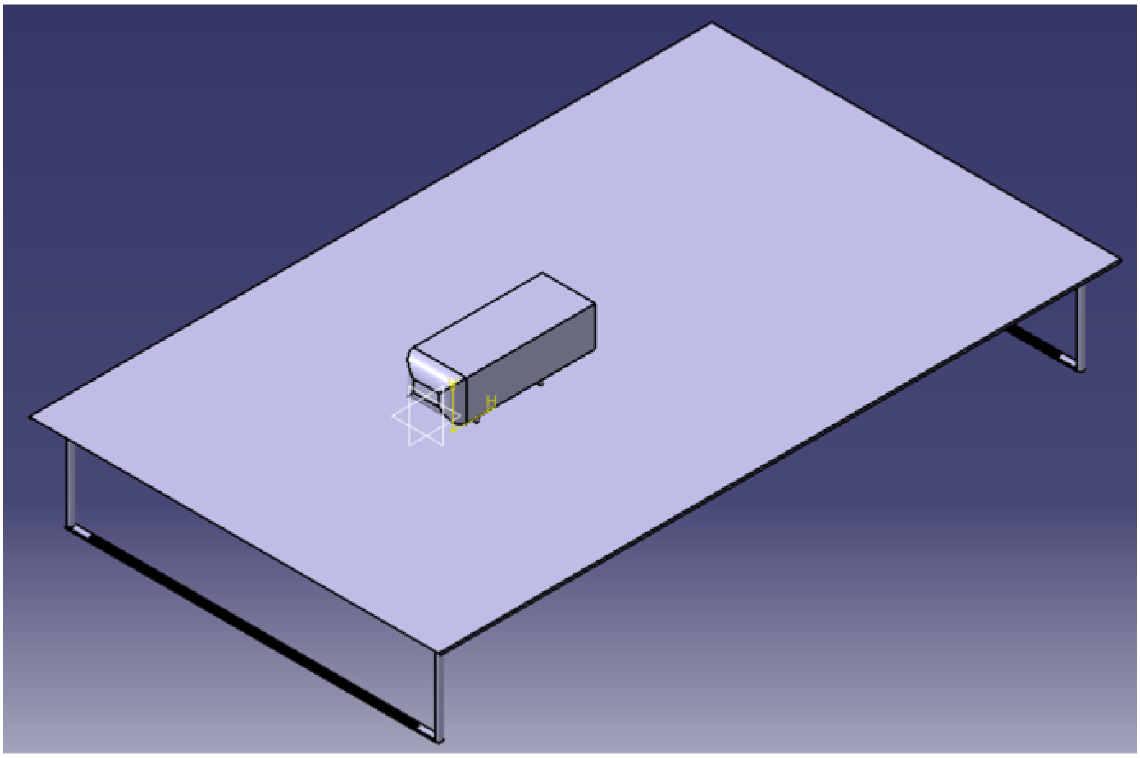

Figure 2.9: CAD geometry of the Ahmed Body with the table

2.8.2.1 Slant Angles

Angle of the rear slant surface plays a significant role in the flow analysis downstream of Ahmed body. Ahmed et al. found that most of the drag was caused by pressure drag which is directly depending on the rear slant angle [31]. A lot of experiments and simulations have been conducted for varying slant angles and it was observed that there was an increase in pressure drag at the rear with increasing slant angle and at 30° slant angle, maximum drag is achieved. The reason for maximum drag is due to the separation of flow at the beginning of slant surface and reattachment near the end of the slant surface. Two strong counter-rotating vortices were observed as a result of this flow separation and attachment. At angles below 30°, the strength of these vortices were found to be low. Hence, it was concluded that rear slanted surface with an angle of 30° to be the critical slant angle. There is however one more critical angle of 12.5° where the flow remains attached throughout the slant surface for any angle below this with 2 counter- rotating longitudinal vortices at the rear end [32] [33].

Many studies have been conducted for slant angles of 25° and 35° to understand the flow behaviour below and above the 30° critical slant angle. Conan et. al. has conducted study on 10° slant angle [34]. Therefore, in this thesis 10°, 25° and 35° slant angles have been chosen for studying the snow deposition patterns on the Ahmed body.

3

Methodology

This section describes the methods incorporated within the two sections: experimental approach and CFD approach. The experimental approach taken towards studying snow deposition on the Wedge and the Ahmed body will be presented. Later, the CFD approach to simulate the same will be described.

3.1 Experimental Approach

A car's exterior often has a complex geometry. Correspondingly, analysis of external aerodynamics of the car and snow build-up gets difficult. Flow patterns that are not significant in the problem under investigation occur because of these geometric complexities. This would result in a more time-consuming CFD simulation. Hence, to simplify the process and still achieve the purpose, it is better to consider a much simple model such as a bluff body. The Wedge was initially utilized by [35] to avoid the problems mentioned above. This model has been previously manufactured at VCC to run snow accumulation tests at the Volvo climatic wind tunnel. Furthermore, the analysis is extended over an Ahmed body, the reason being that it resembles most of the principal aerodynamic features of a real car.

3.1.1 The Wedge

Table 3.1: Geometric dimensions of the wedge

Parameter	**Dimensions [m]**
Wedge dimensions	
$Length(l)$	1.5
$Height(h)$	0.5
Stint dimensions	
$Diameter(d)$	0.25
$Height(h_s)$	0.75

The dimensions of the wedge are given in the Table 3.1 and the manufactured model subject to a wind tunnel experiment is shown in the Figure 3.1. The model was subject to wind tunnel experiments in two ways to make a good comparison between the experimental and the simulation methods. One being the slant face facing the wind tunnel test section entry while the other with the back face facing the test section entry with the flow from left to right as shown in Figure 3.1. The slant face experimental data was obtained from [35] while the back face experiment was performed during this thesis.

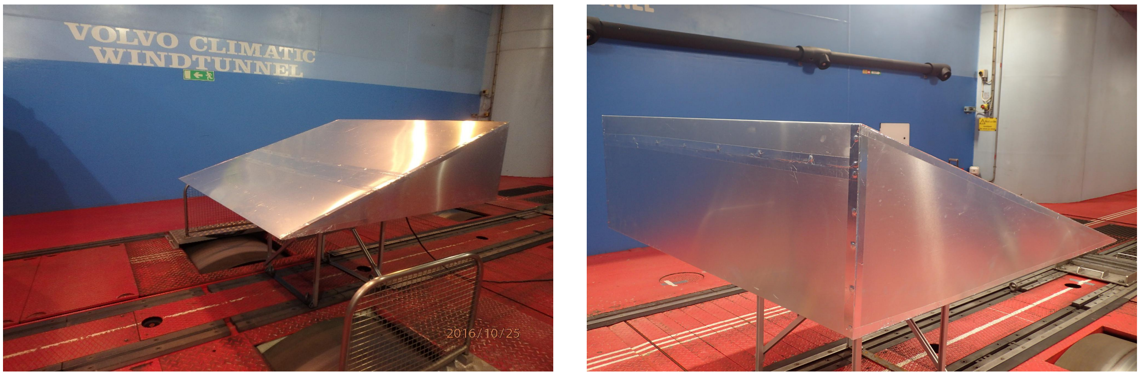

(a) Case A **(b)** Case B

Figure 3.1: Wedge set-up in the climatic wind tunnel. Case A refers to the slant face facing the fan of the wind tunnel and Case B refers to the back face facing the fan of the wind tunnel.

Initially, the Wedge is placed in the wind tunnel as shown in the figure. An operating temperature of $-15°C$ is allowed to reach. A snow cannon is employed for the injection of snow onto the test object. Until significant snow deposition is visible, the snow cannon continues to impinge snow onto the wedge. After all the necessary observations corresponding to snow accumulation are recorded, all contamination on the wedge is removed. simultaneously, the wind tunnel is allowed to cool down and the above procedure is repeated for all the following test runs.

3.1.2 Ahmed Body

Table 3.2: Geometric dimensions of the Ahmed Body

Parameter	**Dimensions [mm]**
Length(l)	1044
Width(w)	389
Height(h)	288
Ground Clearance	50
Slant Angles	10°, 25° and 35°
Slant Length (l_s)	222

The Ahmed body from Ahmed et al. [31] is the inspiration for the geometric measurements taken to design it. The model had a length of 1044 mm, width of 389 mm and height of 288 mm. The clearance from ground to the bottom surface is 50 mm with four small legs of radius 30 mm. We can divide the Ahmed body into 3 sections, the front, middle and rear section. The front section is rounded along all four sides with a radius of 50 mm. The edges of the middle section is rectangle in cross section and sharp edges. The rear body has 3 slant angles - 10°, 25° and 35°. A constant slant length of 222 mm with sharp edges is maintained at all rear sections [31]. The geometric dimensions of the Ahmed body is given in the Table 3.2.

CATIA V5 was utilized for designing the CAD model of the test object and has later been fabricated at Volvo Cars.

Since the ground section the PVKA wind tunnel was not very smooth, a table of resembling the ground dimensions considered in [31] was used for experimental analysis. The Ahmed body was later installed on it as shown in the Figure 3.2. A moving ground effect is an ideal scenario to replicate the real-world road conditions where there is no development of the boundary layer. Since setting up such an apparatus for a scaled model is expensive, we choose to consider a stationary ground in this thesis work.

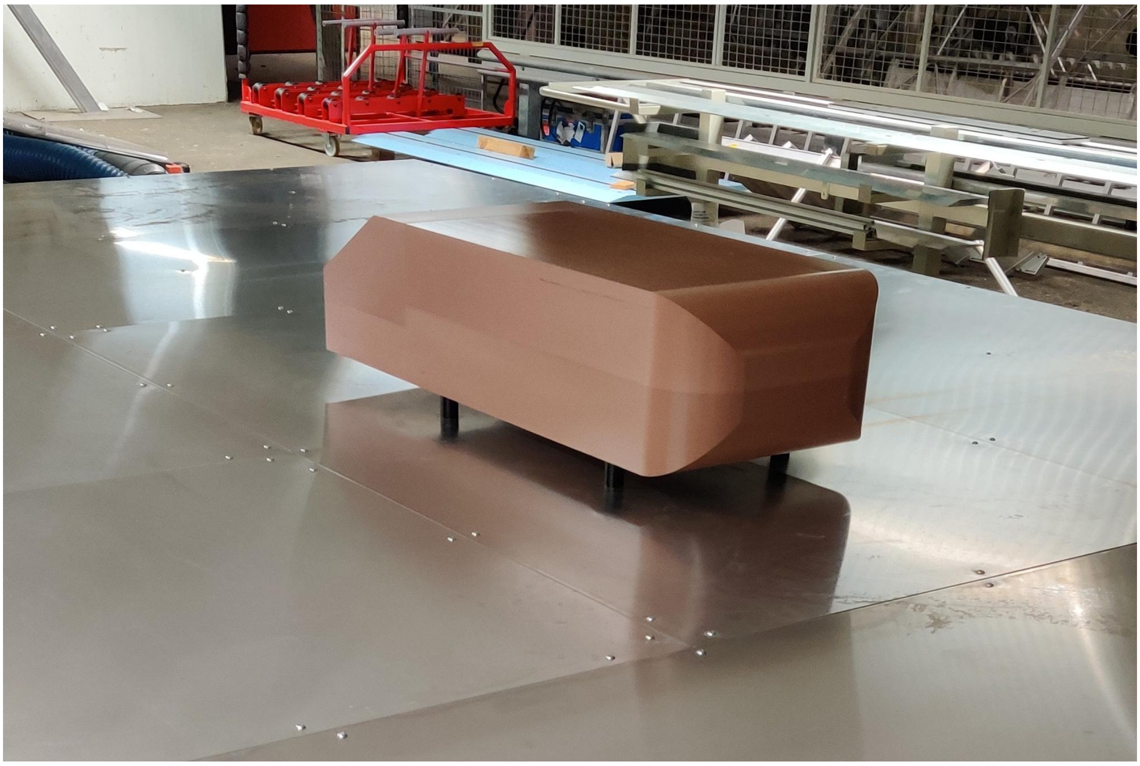

Figure 3.2: Ahmed body set-up with table

The Ahmed body experimental setup is placed in the wind tunnel as shown in the Figure 3.3. An operating temperature of $-15°C$ is consistently maintained throughout. Experimental procedure as described in section 3.1 has been followed here as well. In total, eight trials were conducted (three for 35° configuration, three for 25° configuration and two for 10° configuration) on the Ahmed body to observe the snow deposition pattern. Initially, three trials were conducted with the 35° slant angle rear block attached to the Ahmed body. The next three trials are conducted on the 25° slant angle rear block. The subsequent two trials were repeated for 10°

slant angle rear block. Multiple trials for each configuration has been conducted to ensure repeatability which was a concerning issue with the Wedge.

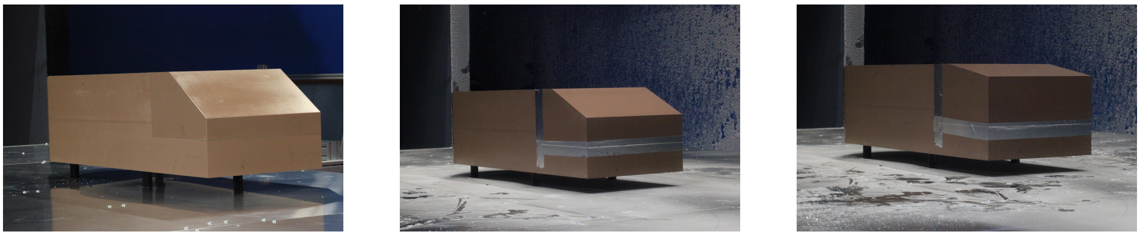
(a) Slant angle 35° **(b)** Slant angle 25° **(c)** Slant angle 10°

Figure 3.3: Ahmed body set-up with table in the climatic wind tunnel with 3 slant angle rear block configurations

3.1.2.1 Tuft Experimental Setup

Upon performing all the trials for all the three slant angle configurations, snow deposition was observed in less expected areas like the one very close to the leading edge of the top and side surfaces where the flow was expected to separate. Hence, an experiment using Tufts were conducted to check the flow attachment and separation zones along the top and side surfaces. Tufts or small thread strands were installed on top, sides and slant faces of the Ahmed body using tapes as seen in Figure 3.4.

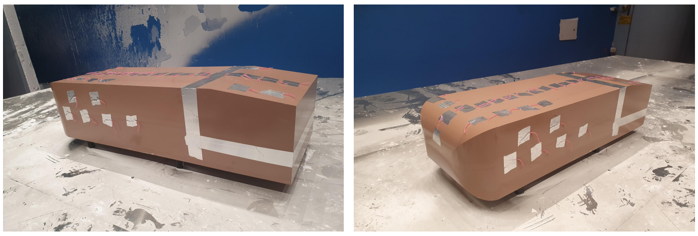

Figure 3.4: Experimental setup using tufts on Ahmed body with slant angle 10° in the wind tunnel

3.2 Simulation Approach

In this section, the CFD approach towards simulating this phenomenon will be described. Construction of the computational domain, meshing strategy, choice of solver settings and different boundary conditions that were implemented on the Wedge and the Ahmed body will be discussed in detail. All the simulations have been carried out using StarCCM+ version 2020.3, which was originally developed by CD-adapco and has later been developed by Siemens. The post-processing has been carried out using Python, Paraview and StarCCM+.

3.2.1 Simulation of Aerodynamic Flow Field

To perform analysis of the particle deposition over the bluff bodies, it is quintessential to have a fully developed aerodynamic flow field around the bluff body initially.

This provides us with the necessary knowledge about the various turbulent flow structures around it that can influence the deposition pattern. In this section, the methods incorporated to simulate the aerodynamic flow field around the Wedge and the Ahmed body will be discussed. First, the Wedge section is chosen, presented as configuration A and configuration B where the former consists of the wedge section oriented with its slant face along the leading edge and the latter with its flat face along the leading edge respectively. Later, the Ahmed body was considered with 3 different slant angle configurations (10°, 25° and 35°)

3.2.1.1 Geometry

The first step in the simulation process involves the creation of an accurate CAD geometry of the Wedge and the Ahmed body. The CAD geometries were created using the *Design Modeler* module within StarCCM+. Note that for the Wedge, a similar geometry (Wedge) has been previously used in a thesis work (Refer [8]) to study the snow deposition but in a different orientation. As seen in Figure 3.5, the bluff body consists of the Wedge section which is supported by uniformly spaced stilts at the bottom. The dimensions of the Wedge are same as previously presented in Table 3.1.

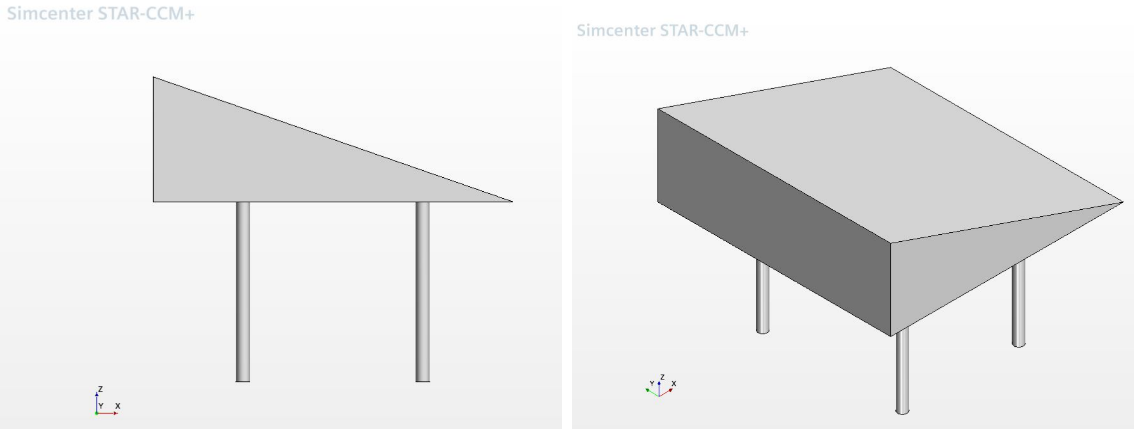

Figure 3.5: Front and side view of the wedge

Meanwhile, the Ahmed body dimensions were obtained from Ahmed et al. [31] and their CAD geometries were created as seen in Figure 3.6. The dimensions of it for all three configurations have been described in Table 3.2.

Figure 3.6: Ahmed body with slant angle configurations 10°, 25° and 35°

3.2.1.2 Meshing

To ensure the computational domain is sufficiently large with concerning the size of the body, the Blockage Ratio (BR) is used as the indicator to verify that the applied boundary conditions does not affect the computational domain. BR is computed to be the ratio between the size of the body to the size of the overall domain. Furthermore, the body is placed approximately about 1/4 times the length downstream from the inlet. The dimensions of the domain are as presented in Table 3.3.

Table 3.3: Computational domain dimensions

Section	Length [m]	Width [m]	Height [m]
Outer Domain	70	40	30
Refinement Box 1	11	3.4	1.5
Refinement Box 2	18	5	3.5

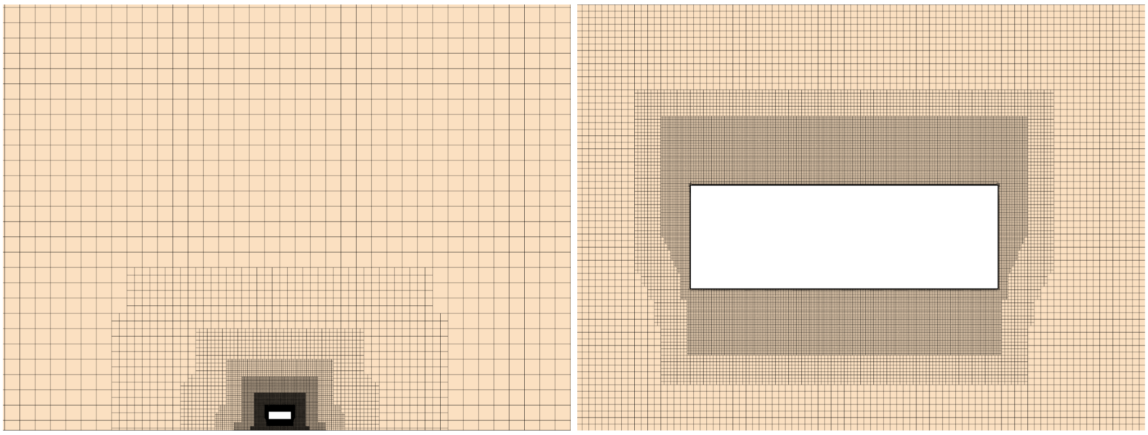

(a) Front section view **(b)** Close-up view

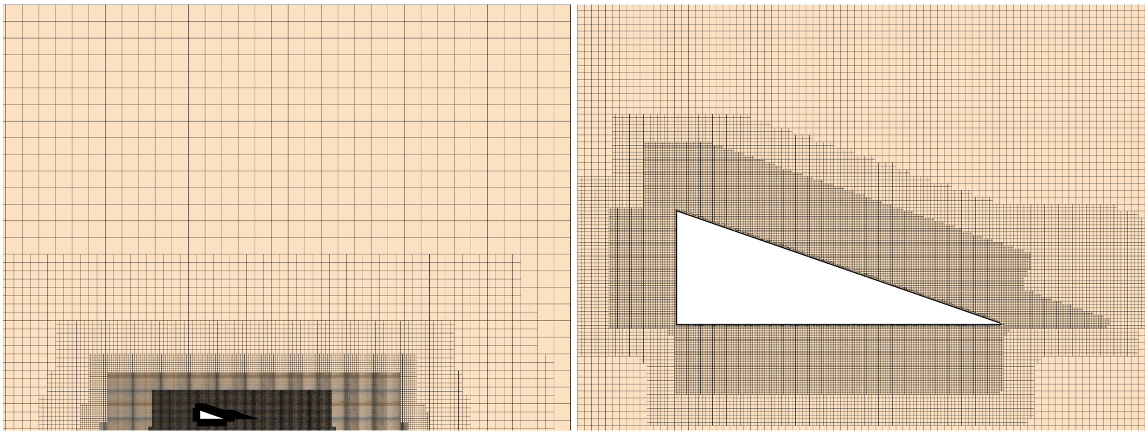

(c) Side section view **(d)** Close-up view

Figure 3.7: Meshed Computational domain: Wedge

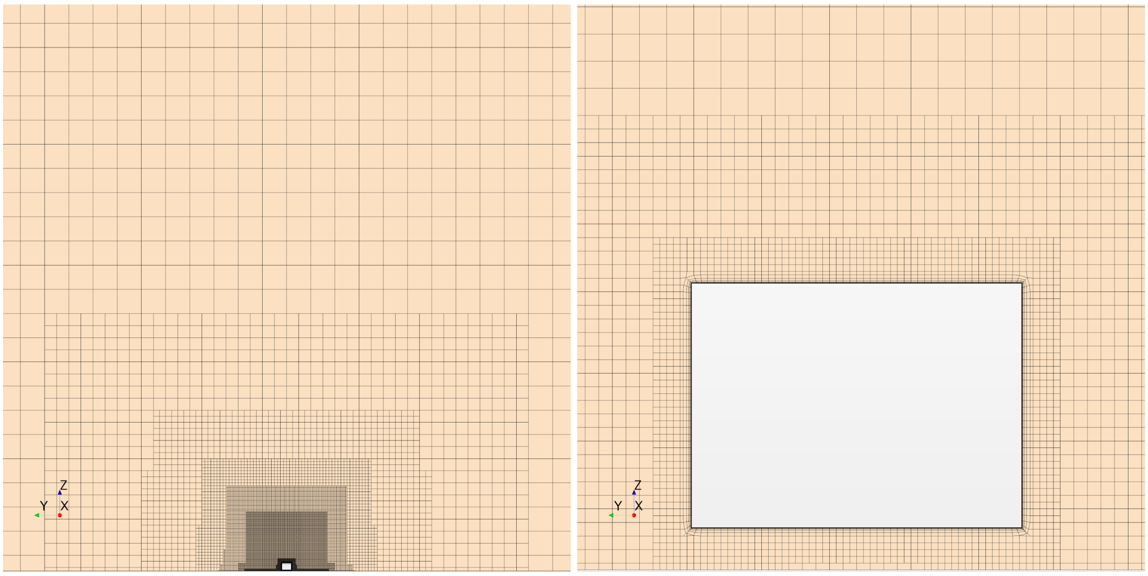

(a) Front section view **(b)** Close-up view

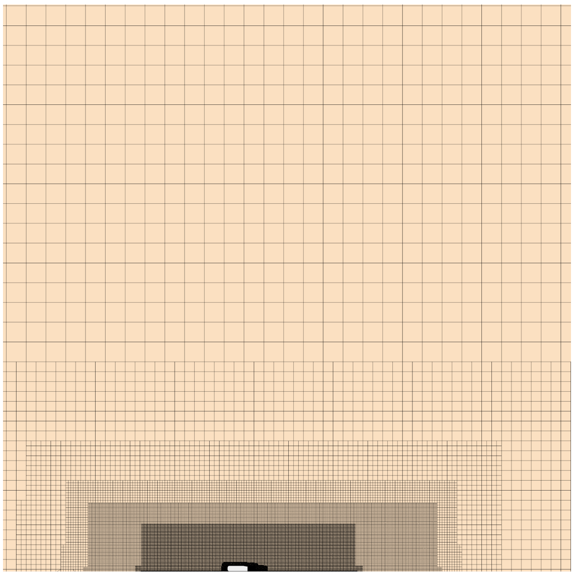

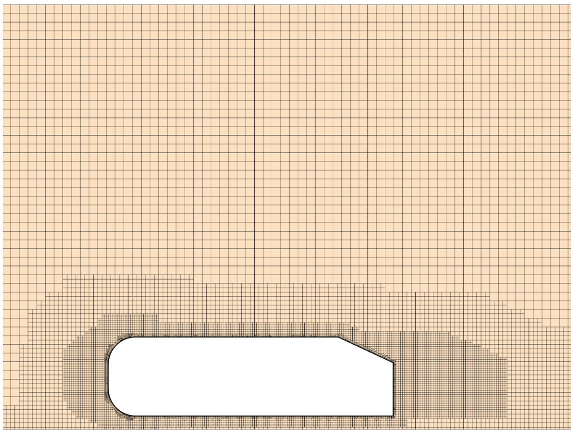

(d) Close-up view

(c) Side section view

Figure 3.8: Meshed Computational domain: Ahmed Body

To solve for the above-established domain, a numerical grid is necessary. The next step is to decompose the entire domain into a finite volume representation. In this thesis, all of the meshing operations have been performed using the meshing module (*operations*) within StarCCM+. So, the Wedge and the Ahmed body surfaces were initially surface wrapped. Surface wrapping can be related to wrapping up the entire CAD geometry with a layer of fabric/skin. Technically, this made the geometric part computationally much lighter by wrapping multiple interconnected parts with a single outer layer or when the quality of the initial CAD geometry is low or to patch gaps if any, between adjoining surfaces and to also prevent the creation of any volume meshes within it. On the contrary, to obtain even more accurate results it was necessary to have a fairly high quality of the surface mesh. This was achieved by implementing the following meshing features:

- Surface wrapping the geometry with a low value for minimum mesh size of 2 mm.
- Using contact prevention to prevent merging of two or more adjoining part surfaces, especially sharp corners and edges.
- Using gap closure to fill volume between two adjoining part surfaces.
- Performing curvature refinement along curved surfaces.

Since external flow being the computational interest here, the fluid volume between the surface wrapped CAD geometry and the outer domain is then volume meshed. The volume mesh generated is as presented in Figures 3.7 and 3.8.

To capture the wake formations accurately, refinement volumes are separately defined. These refinement zones are volume enclosures around the body under consideration with relatively finer meshing which enables to capture of the flow with much accurate details. Also, to capture the near-wall effects for wall-bounded flows, prism layer meshing was implemented. To achieve the desired y^+ values at the wall, the relevant number of prism layers with suitable near-wall thickness and total height has been chosen. Also, precautions has been taken to avoid y^+ values within the buffer layer (i.e. $5 < y^+ < 30$) for wall immediate cell layer.

Hence, a low y^+ value around unity was aimed for first cell. Trimmed cell mesher has been employed for the rest of the domain which is most desirable for volume meshing due to its high robustness and minimal cell skewness. Additionally, custom meshing was defined at certain places such as wake and near wall regions just around the body under consideration to ensure multi-directional mesh refinement.

After volume meshing the domain, the same was checked for the poor quality of cells to minimise meshing errors. This was implemented using the *surface repair* tool on StarCCM+. Local cell quality metrics including negative volumes, face validity, cell skewness angle, volume change and cell quality were considered. A threshold for each of these metrics was compared with each of the volume cells within the domain for bad cell detection. The different cell quality parameters assessed here were as presented in Table 3.4

Table 3.4: Local cell quality metrics

Parameter	Threshold value
Negative volume cells	Face validity<0.5
Face validity	$>= 1.0$
Cell skewness angle	$< 85°$
Volume change	> 0.01
Cell quality	$>= 1.0 * 10^{-5}$

3.2.1.3 Boundary Conditions

Boundary conditions specify the required constraints that are to be satisfied at a given boundary, for a boundary value problem. In this section, different boundary conditions specified within the domain will be discussed.

For the Wedge and the Ahmed body, a no-slip wall boundary was considered. At the outlet, pressure boundary was specified. The ambient temperature was assumed to be a constant value (-15°) throughout. A turbulent intensity of 0.1 % was supplied at the inlet of the domain. The treatment of various boundaries was as tabulated in Table 3.5.

Table 3.5: Boundary conditions

Section	Boundary condition
Bluff body	Wall
Inlet	Velocity inlet
Outlet	Pressure outlet
Ground	Stationary wall (no-Slip)
Top	Symmetry plane
Side-walls	Symmetry plane

For the Wedge, a fluid velocity of 70 km/h (approximately 19.44 m/s) was supplied at the inlet boundary of the domain. As mentioned earlier, Enmark et al. had performed the experiment and simulation for Case A at this speed. So in order to get a good comparison for Case B, this speed was chosen [8].

For the Ahmed body, a fluid velocity of 115 km/h (approximately 31.94 m/s) was supplied at the inlet of the domain. Lienhart et al. had maintained a height based Reynold's number of 2.78 million in their study [36]. So it was decided to maintain the same Re for this thesis and then use this to calculate the fluid velocity for -15°. The Re equation is given below:

$$Re = \frac{\rho u L}{\mu} \tag{3.1}$$

For a Lagrangian Particle Tracking simulation, it is most important to define appropriate boundary conditions at every wall surfaces. Particle-wall modeling being one of the topics under evaluation, no criterion is imposed at this point which controls the particle stick or bounce. Hence, particle-wall interactions along all surfaces of the bluff body are set to rebound, with a pre-defined value of restitution coefficient.

3.2.1.4 Physics models and Solver settings

Appropriate physics modeling and choice of solver settings are necessary to arrive at a converged solution. This section explains the various physics models involved in this analysis and preferred choice of solver settings to solve the numerical system of equations, until the specified stopping criteria are met.

As for the flow characteristics, a turbulent flow domain has been considered with the IDDES turbulence model. SST-Menter $k - \omega$ model has been chosen along with all y^+ wall treatment for near-wall turbulence. Solution dependency on density changes are assumed to be negligible, hence a constant density solver is chosen.

To solve for the pressure-velocity coupling, a segregated flow solver is chosen. Segregated flow solver solves for the mass and momentum conservation equations in a sequential procedure. An algorithm is employed for Pressure-velocity coupling where the velocity field is continually solved until convergence, taking solution from the pressure correction equation. Here, the SIMPLE algorithm is used to solve for the pressure-velocity coupling. This algorithm solves several inner iterations for pressure correction values at each time step to solve for the velocity field. A sufficient number of inner iterations with appropriate under-relaxation factors prescribed for this application have been chosen to ensure accurate results.

As for the discretization schemes, a hybrid second-order upwind / bounded central differencing scheme is used for spatial discretization and a second-order scheme for temporal discretization. In addition to field variable values, their gradients are required at cell centres and cell-face centres for the construction of variable values at the cell faces. This further facilitates secondary gradients in the calculation for diffusion terms, pressure gradients for pressure-velocity coupling and strain-rate and rotation-rate calculations for turbulence models. So, To compute these gradients, a hybrid Gauss Least-Squares (LSQ) method is used. Also, to limit these gradients within reasonable bounds, the Venkatakrishnan gradient limiter is employed.

Table 3.6: Choice of Physics models

Continuous phase	Physics Model
Flow characteristics	Turbulent flow, incompressible flow
Temporal discretization	Implicit-unsteady
Equation of state	Constant density
Turbulence model	IDDES SST Menter k-ω model

Table 3.7: Choice of Solver settings

Flow solver type	Segregated flow
Pressure-velocity coupling	SIMPLE algorithm
Spatial discretization	Hybrid second order upwind/BCD
Temporal discretization	Hybrid second order upwind
Variable gradients	Hybrid Gauss-LSQ method
Gradient limiter	Venkatakrishnan gradient limiter

3.2.2 Mesh Resolution Study

To obtain a reliable solution it is important to have an appropriate mesh that can capture the important details of the flow field accurately. To verify the same, the ratio of resolved Turbulent Kinetic Energy (TKE) to the total TKE, (M) parameter is looked upon. Essentially, this parameter gives an estimation of how much turbulent kinetic energy is resolved within the LES operated regions. The M parameter is computed as :

$$M = \left(\frac{K_{resolved}}{K_{resolved} + K_{sgs}}\right) \tag{3.2}$$

where $K_{resolved}$ is the resolved turbulent kinetic energy, K_{sgs} is the modeled turbulent kinetic energy.

3.2.2.1 The Wedge

From Figure 3.9 it can be seen that the blending function is around unity very close to the wall and eventually tends to zero in the outer sections. Here, unity value refers to RANS operated regions while the solution is LES as it tends to zero.

Furthermore, the M parameter along the centre plane is visualized in Figure 3.10. A sufficiently fine mesh must resolve atleast eighty percent of the turbulence. From the side view, it can be observed within the LES operated regions that the turbulence resolution around the Wedge section is very close to unity or more than eighty percent at the least, except at the extreme edges which could possibly be due to presence of prism layer cells.

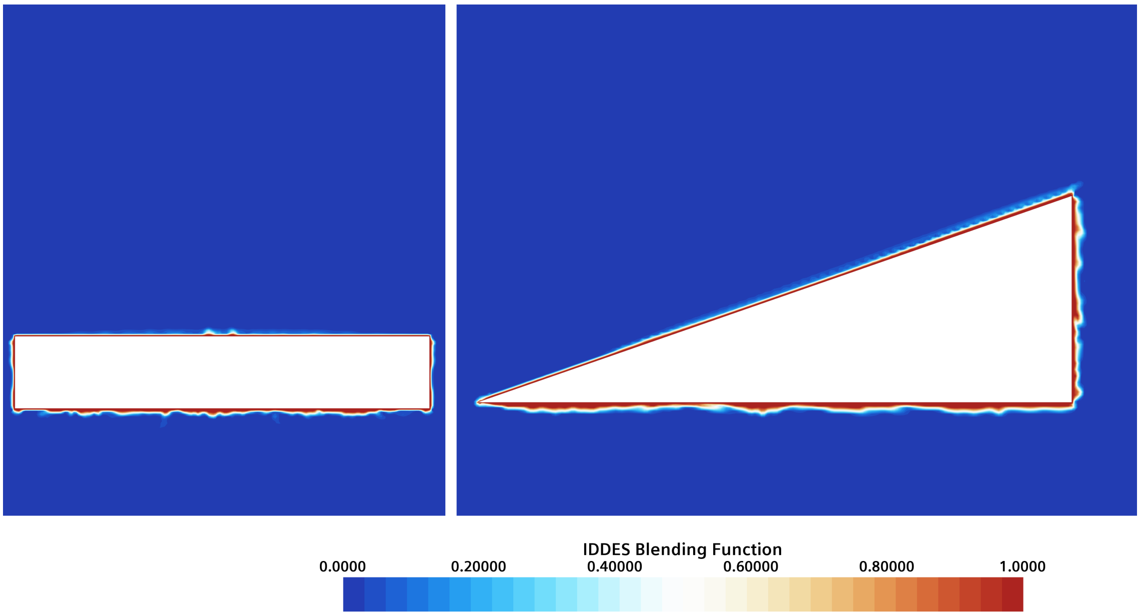

Figure 3.9: IDDES blending function for the Wedge

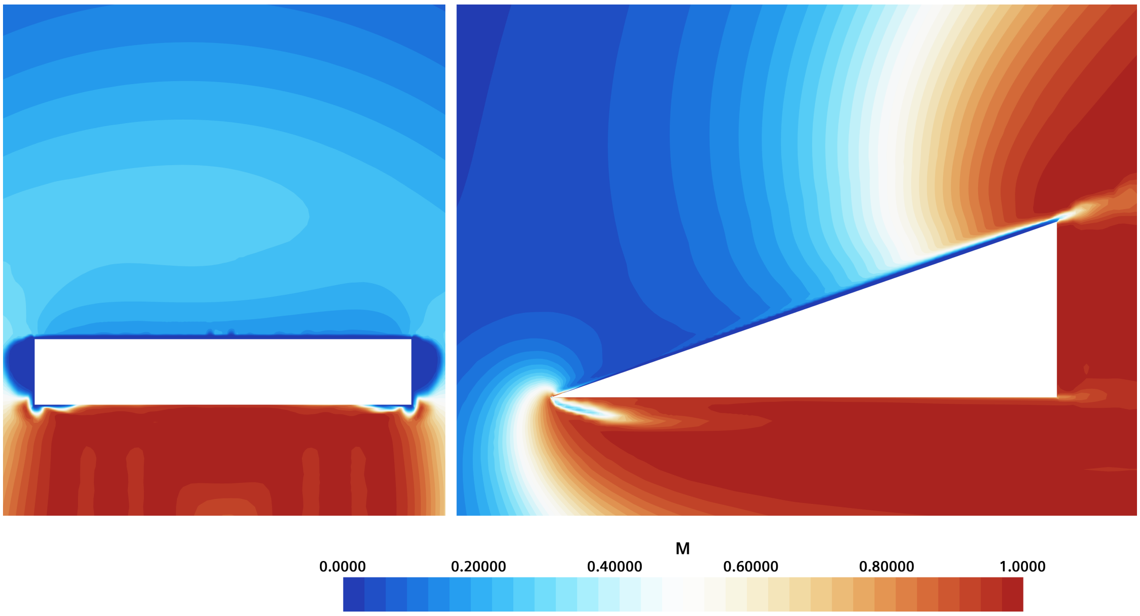

Figure 3.10: Visualization of M parameter

3.2.2.2 Ahmed Body

Figure 3.11 it can be observed that the region near the Ahmed body is operating in RANS mode throughout while the solution follows LES formulation just before the front surface and along the wake region downstream. Now contrasting the regions in Figure 3.12 with values greater than 0.8 with regions close to zero in Figure 3.11, it can be observed that the turbulence is resolved enough within the LES operated zones.

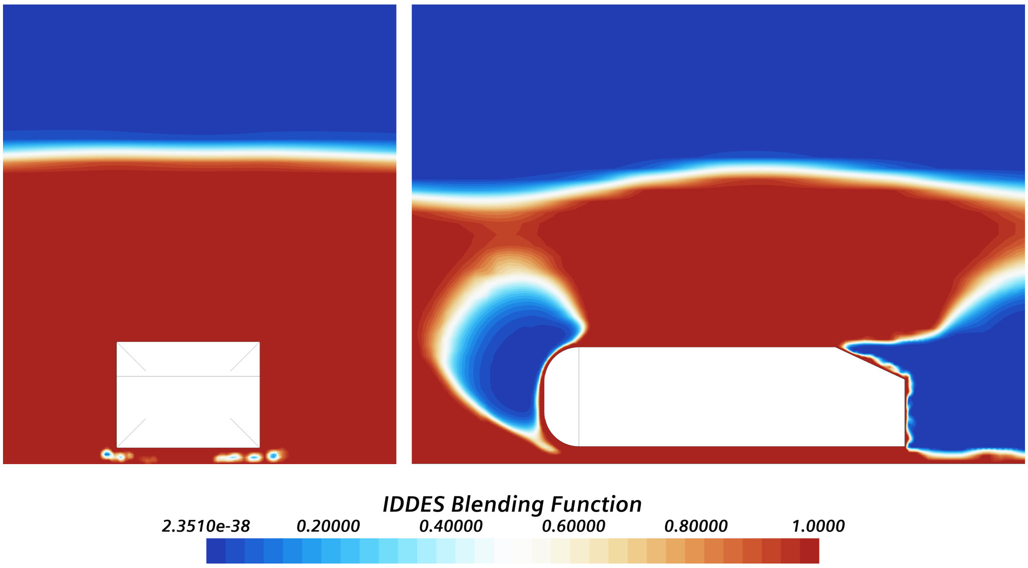

Figure 3.11: IDDES blending function for Ahmed body with slant angle 25°

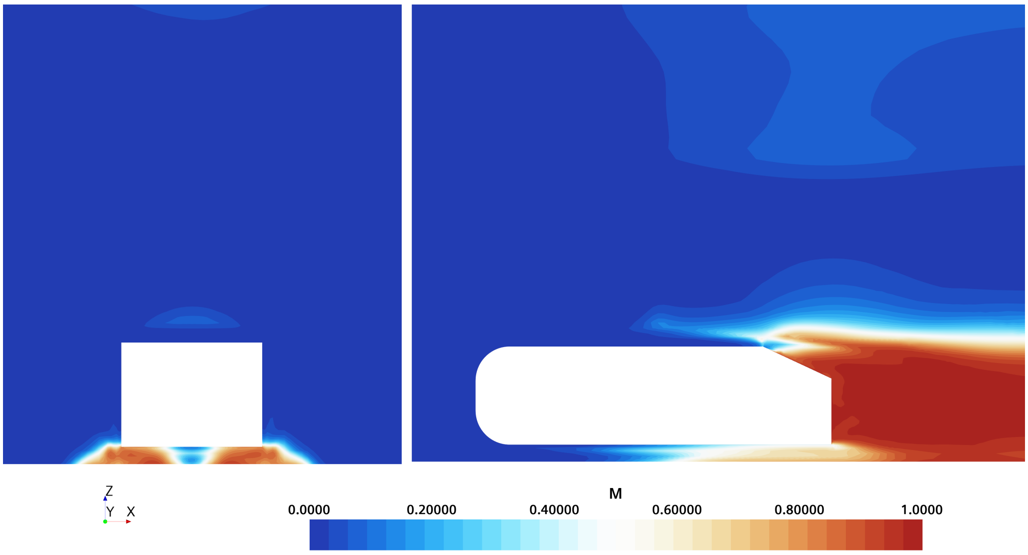

Figure 3.12: Mesh Resolution Study

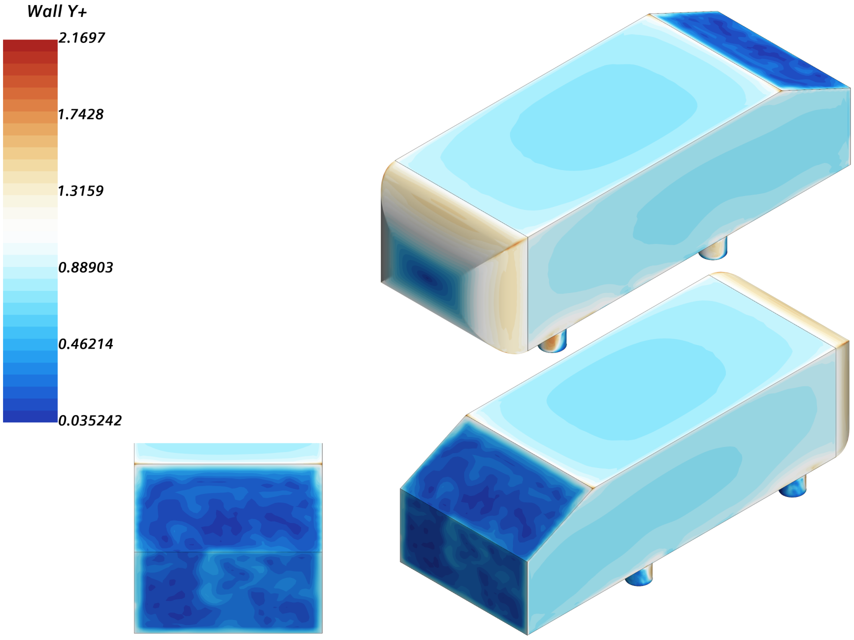

Figure 3.13: Wall Y+ on Ahmed body with slant angle 25°

To resolve the wall bounded flow, it is crucial to capture the effects due boundary layer. To achieve this, prism layer cells and correspondingly an appropriate first cell layer height are to be chosen. It is preferable to have a low wall $Y+$ treatment in our simulation to resolve the boundary layer enough. A good estimation would be to achieve wall $Y+$ values around unity. However, a common question is how many prism layers are necessary to resolve the boundary layer enough? For this application, upto 12 prism layers have been chosen along the Ahmed body surface and just one prism layer in the outer domain where they are less important. Figure 3.13 depicts the variation of wall $Y+$ along all the surfaces of the Ahmed body. It can be observed that the wall $Y+$ values are mostly around unity except for at the edges and at the curvature, which could possibly be due to the presence of very thin prism layer cells in the near-wall region.

3.2.3 Temporal Resolution Study

To verify if the chosen time stepping is fine enough, Convective Courant Number (CCN) is a useful indicator. Ideally, courant number around unity signifies a fine enough time stepping.

3.2.3.1 The Wedge

CCN along a cut plane has been visualized in Figure 3.14. It can be observed that CCN is less than unity along most of the surfaces of the bluff body, except the stilts, which is not of primary interest here. However, it is quite high at the edges, which could be the effect due to the presence of very thin cells within the prism layer. Also, CCN is between unity and two around the bluff body. This conveys that the chosen time stepping is fine enough to achieve convergence.

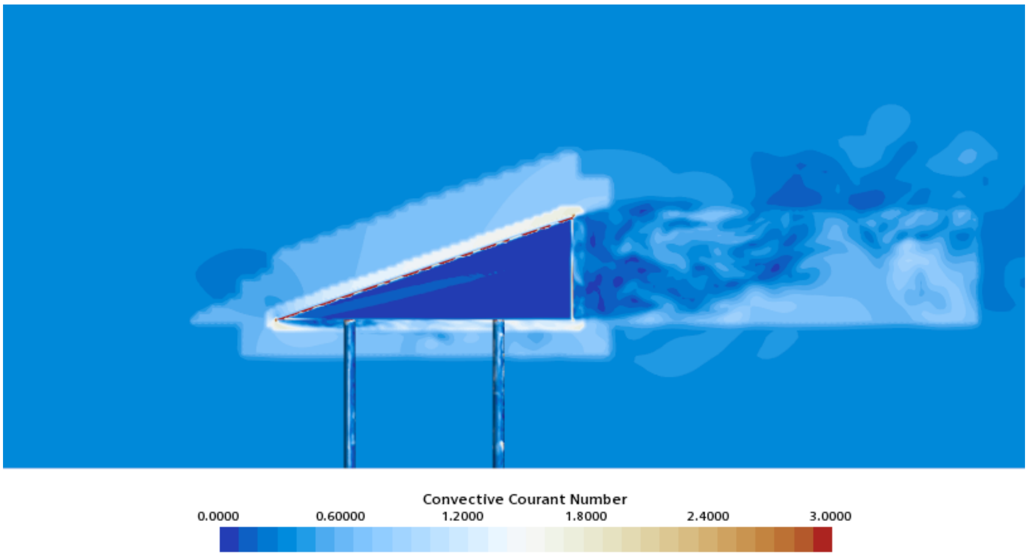

Figure 3.14: Convective Courant Number, cut-section view

3.2.3.2 Ahmed Body

To ensure temporal resolution, CCN has been visualized in figure 3.15 where the CCN is less than unity on all the surfaces of the Ahmed body except at few edges. The magnitude is highest at the top and bottom curves of the front curvature. This is due to the presence of very thin cells in the prism layer region very close to the wall. The CCN is about 0.5 near the slant and the rear wake region, while it is between 1 to 1.5 around the body as seen from the cut plane section view. With this study, it can be inferred that the time stepping chosen is sufficient enough to obtain convergence and expected accuracy of results.

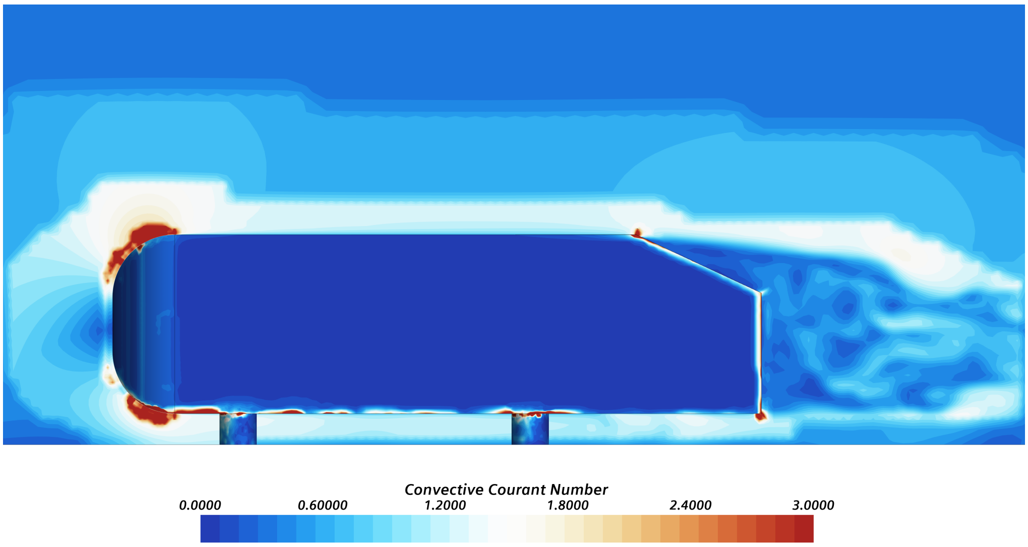

Figure 3.15: Convective Courant Number

3.2.4 Flow Development Study

To study the aerodynamic features of any object/body, it is important to obtain a completely developed flow field initially. To verify the same, probe points have been established at various locations around the bluff body and have been simulated long enough until the flow field is fully developed. This is done by solving until the mean velocity fluctuations display a stabilized trend.

3.2.4.1 The Wedge

It can be seen from Figure 3.16 that the mean velocity along each probe point along different surfaces has an eventual decrease in velocity fluctuations, meaning that the flow field has fully developed. This indicates that the simulation has been run for long enough, providing sufficient time for the development of a well-established flow field.

3.2.4.2 Ahmed Body

Figure 3.17 provides the velocity-time history which has been monitored throughout the solution using several probe points at different locations around the Ahmed body. The mean velocity fluctuations along all the surfaces eventually decrease over time indicating that the flow field has developed. Therefore, it can be assumed that the simulation has run long enough to establish a well-developed flow field.

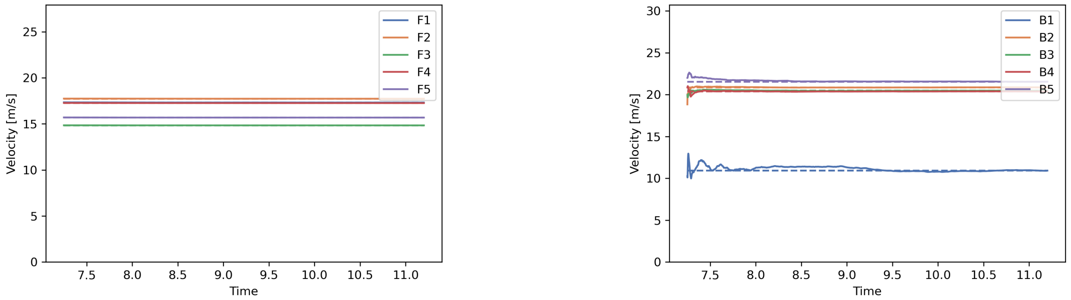

(a) Front surface **(b)** Bottom surface

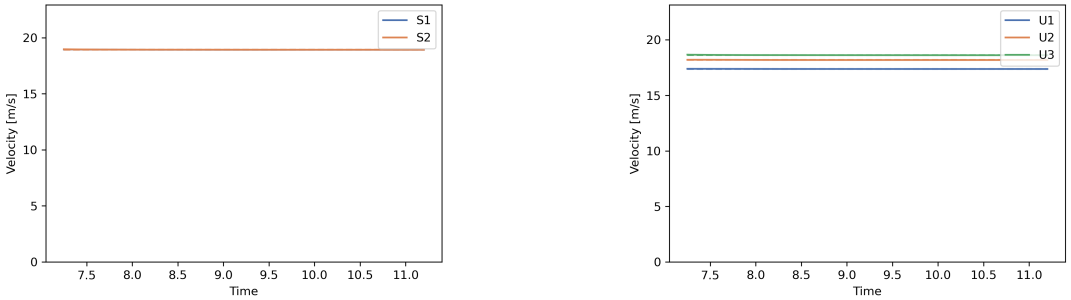

(c) Side surfaces **(d)** Upper surface

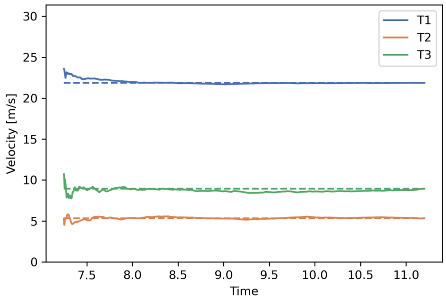

(e) Wake region

Figure 3.16: Velocity-time history in a monitor plot along various probe points

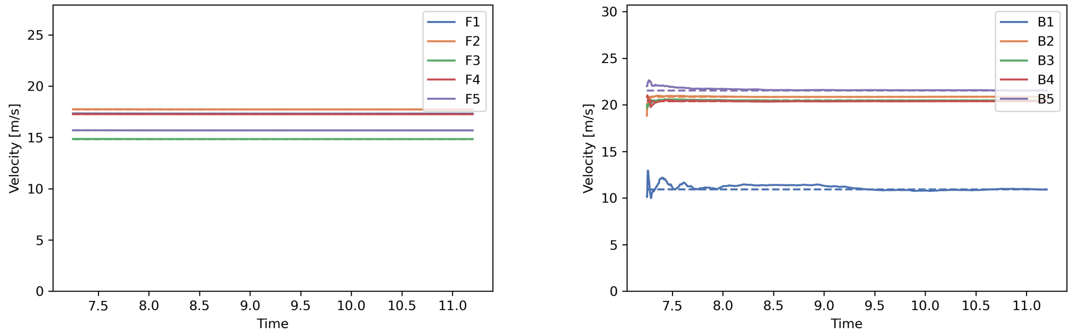

(a) Front surface **(b)** Bottom surface

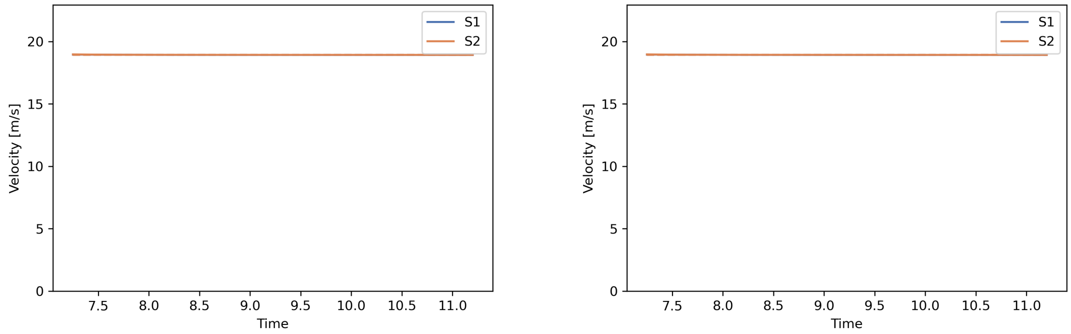

(c) Left Side surfaces **(d)** Right Side surfaces

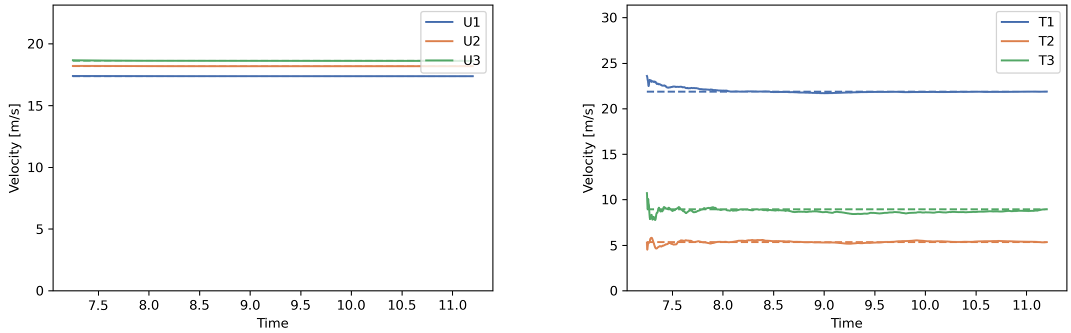

(e) Upper surface **(f)** Top surface

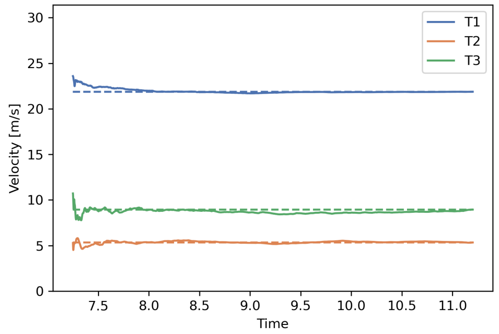

(g) Rear surface

Figure 3.17: Velocity-Time history at various locations around the Ahmed body

3.2.5 Convergence Study

To conclude any CFD study, the solution must converge well within the tolerance limits. To verify this, it is beneficial to look into indicators such as Residuals, Solver Iteration Elapsed Time (SIET) and Solver Time Elapsed Per Time-Step (STET) for any anomalies including divergence in either the continuity, momentum or turbulent kinetic energy, or even for any other solver instabilities.

3.2.5.1 The Wedge

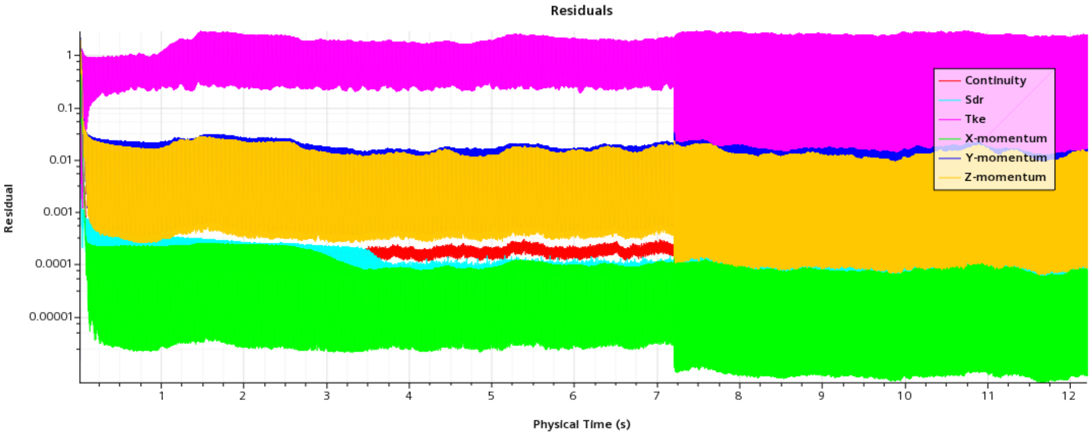

Figure 3.18: Residual plot

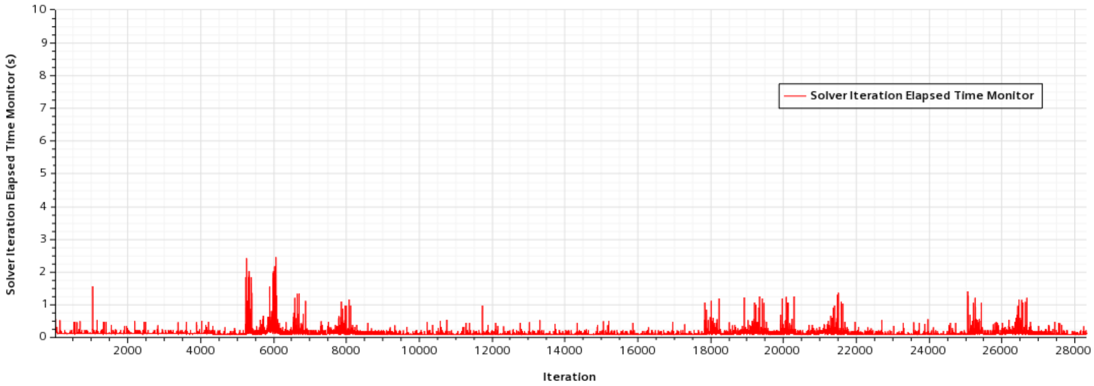

Figure 3.19: SIET monitor

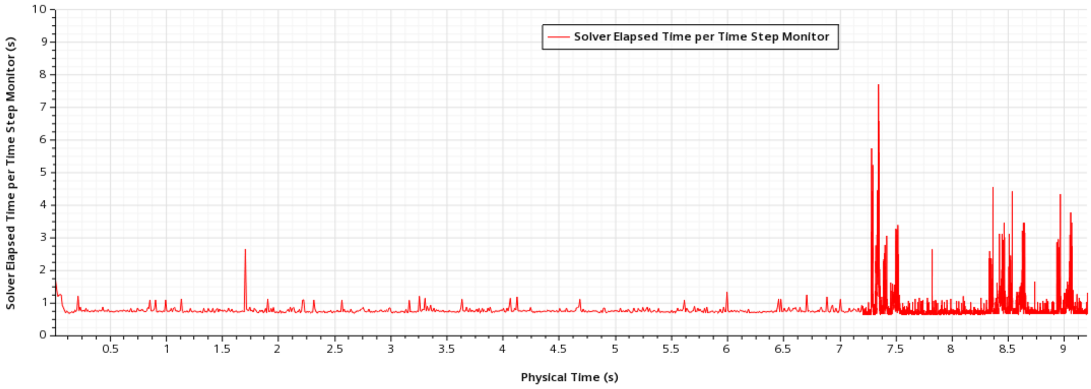

Figure 3.20: STET monitor

From Figure 3.18, it can be seen that the above listed parameters have stabilized over time and do not display any anomalies. Figure 3.19 and 3.20 show the SIET and STET monitors respectively. SIET shows the solver elapsed time to execute previous iteration while SIET shows the solver elapsed time to execute previous time-step. It can be observed that the trend is almost constant in both the cases but with occasional peaks. A non-converged solution is attributed with frequently recurring peaks, which is not the case here.These results are evidence that the solution has converged and one can expect reliable quality of results.

3.2.5.2 Ahmed Body

From Figure 3.21, it can be observed that these three parameters have achieved stability over time and there is no visibility of any anomalies. From Figure 3.22, not much spikes are observed frequently. In Figure 3.23 however, minor instabilities are observed at one point but they are not very large in comparison with rest of the time duration. Hence, it can be neglected.

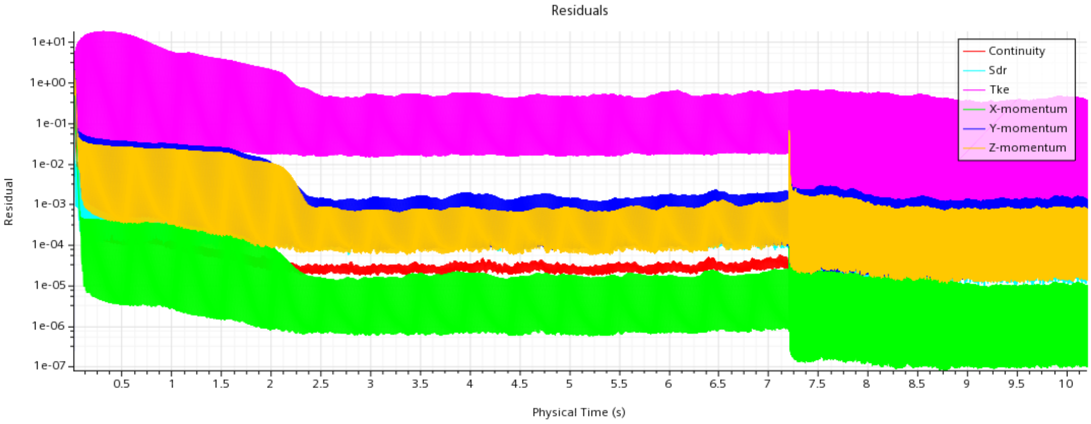

Figure 3.21: Residual plot

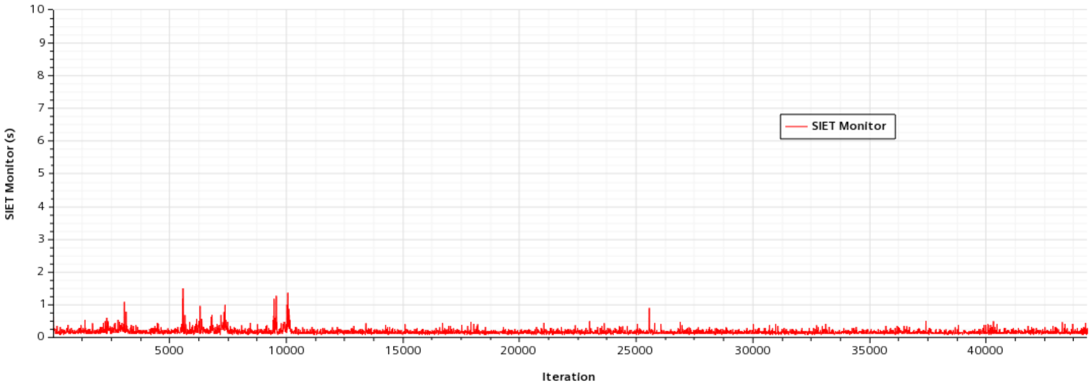

Figure 3.22: SIET monitor

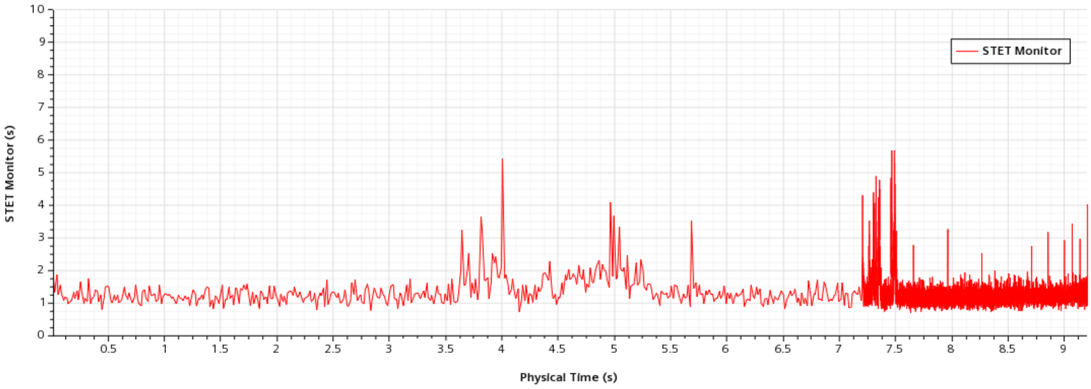

Figure 3.23: STET monitor

3.2.6 Particle Simulation Method

3.2.6.1 Particle Modeling Assumptions

Simulation of snow as in real life is by the very fact, challenging in nature. As seen from the various complexities involved in Section 2.6 , it is wise to begin with few considerations for simplicity purpose. Thereby certain modeling assumptions are initially made, corresponding to which simulating physics are defined accordingly. Few important assumptions made in this thesis are as listed below:

1. Particles are considered to be solid, spherical, material particles.
2. A constant temperature of -15° is considered throughout.
3. Particles are considered to belong to quasi-elastic collisional damping regime and contributions from that alone is considered.

3.2.6.2 Parcel Injection

Once a fully developed flow field is obtained, the domain can now be injected with particles. To do so, we make use of *Injector* in StarCCM+. While the Lagrangian phase solver settings defines the type of particles entering the domain and how they interact with other boundaries, the injector facilitates the particles to be input into the domain as to where, in which direction and at what frequency must they be injected.

A Grid-type injector is utilized to introduce particles into the domain. The injection grid is placed at about 1.5 metres from the bluff body. The particles are injected along the stream-wise direction with a unit velocity at the point of injection. The particle size specification at an injector can either be specified by diameter or mass. Here, the particle diameter is specified at the injector.

3.2.6.3 Particle Size Distribution (PSD)

A mass-weighted cumulative distribution function for a range of particle diameters were observed through microscopic image analysis. It was seen that a Rosin-Rammler type PSD is most appropriate. Hence, the PSD properties as listed in Table 3.8 shall be used for simulations.

Table 3.8: Particle Size Distribution (PSD) properties

Parameter	Value
Injector	Grid-type
PSD type	Rosin-Rammler
Mean diameter	90E-06 [m]

3.2.6.4 Particle Force Model

In order for the particles to collide with the surface, it is important for it to interact sufficiently well with the flow field. consequently, in order to have a reliable aerodynamic flow field, chosen turbulence model must function as they are intended to. The ideology behind IDDES turbulence model is mainly to treat the boundary layer with RANS and capture the outer detached eddies by using LES. To visualize the regions where each of these models would exercise, it would be beneficial to look at the regions being operated in RANS and LES modes respectively.

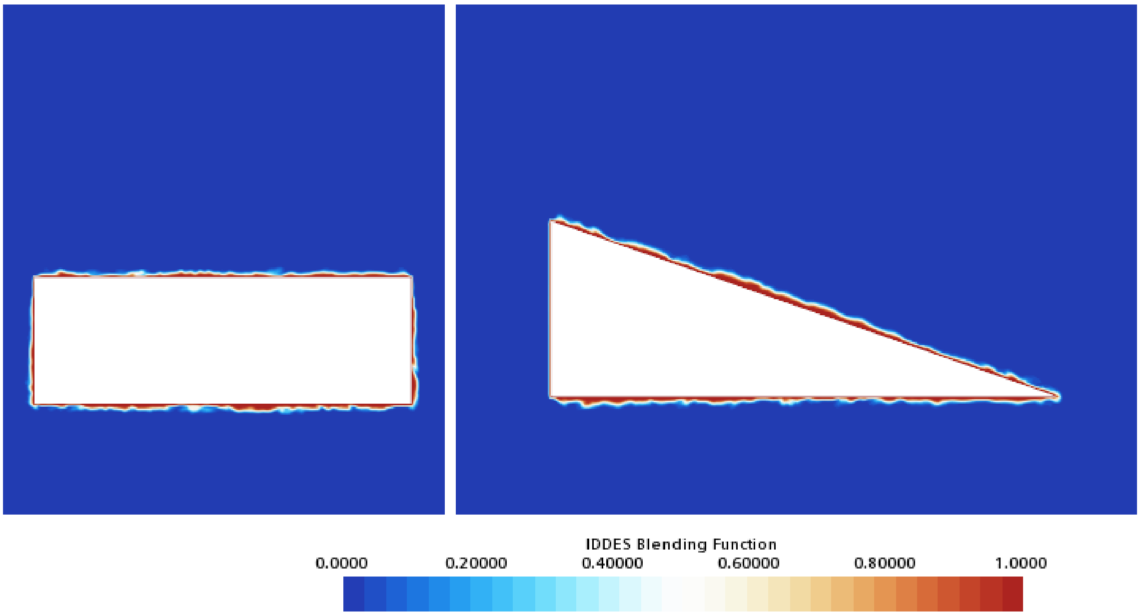

Figure 3.24: Wedge: Backward configuration

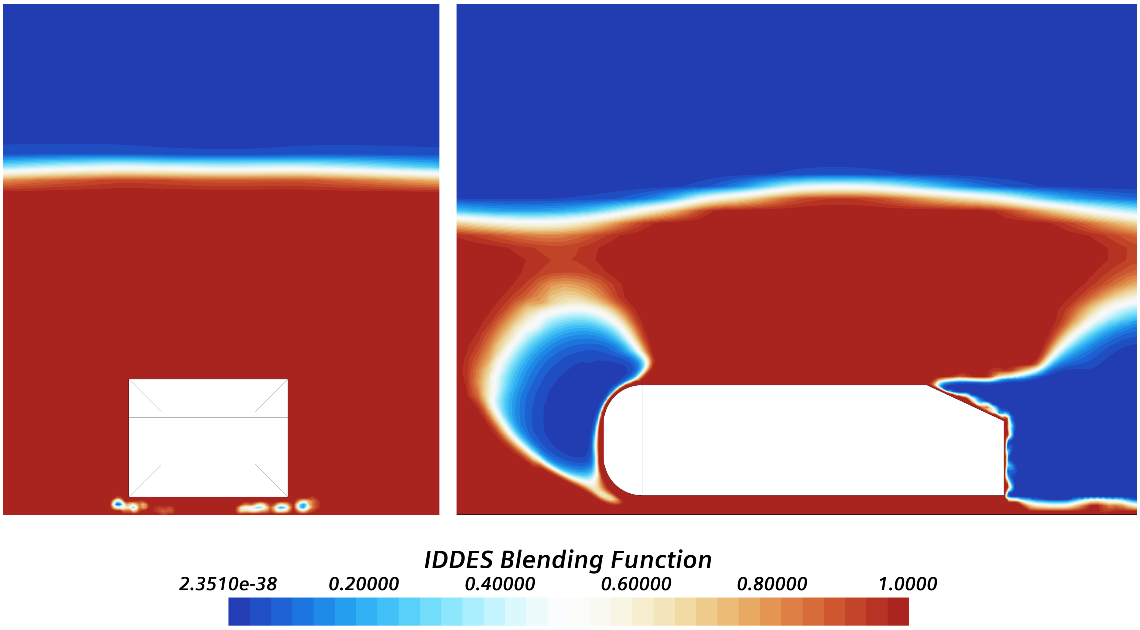

Figure 3.25: Ahmed body with slant angle 25°

Figures 3.24 and 3.25 illustrates the variation of IDDES blending function around the Wedge and Ahmed body respectively. Regions with unity value correspond to RANS operated region while the solution tends towards LES formulation for values close to zero. Closer to the wall in the viscous sub-layer, velocity fluctuations are not present within the RANS region. Hence, one could argue that the wall treatment should model everything up to $y+ \approx 30$ (i.e RANS operated region). In case of the Wedge, The turbulence model functions as discussed earlier. Interestingly, in case of the Ahmed body, it is observed that the RANS region operates in the near-wall region but also further beyond the Ahmed body.

To investigate this speculation further, velocity fluctuations along two set of locations are observed. Figure 3.26 show the probe points placed at the near wall region and outer region along the centre plane of the Ahmed body while Figure 3.27 shows a comparison of velocity fluctuations at the above mentioned two areas. One can observe that the velocity fluctuations near the wall is rather very meek as compared to that along the outer regions. This can be related to the fact that very close to the wall the flow is viscous stress dominated and the turbulent ones decrease as we go nearer [2]. Hence, not much velocity fluctuations can be expected here.

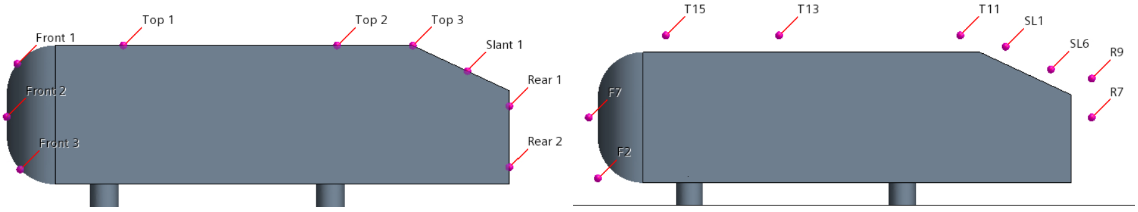

Figure 3.26: Probe points placed at near wall region vs outer region

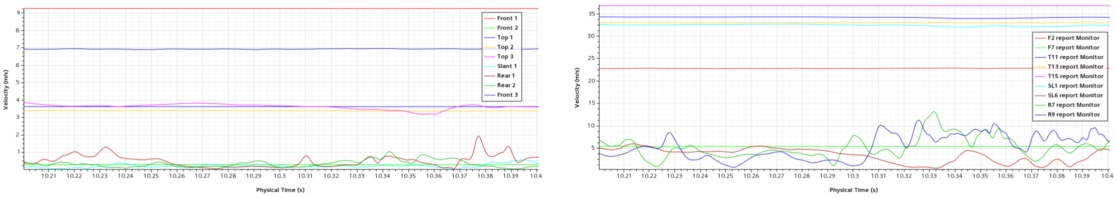

Figure 3.27: Velocity fluctuations at near wall region vs outer region

As discussed earlier, near wall region is supposedly a RANS operated region while the outer region is operated with LES. But since RANS still operates at the outer regions as seen from Figure 3.11, turbulence is being modeled all through that regime. On the contrary, velocity fluctuations at the outer regions are still meek as seen in the Figure 3.27, except for at the rear wake region where the recorded data points lie in the LES operated region.

Furthermore, this finding supports the previous assumption concerning the requirement of an additional turbulent dispersion model or discrete random walk model to induce velocity fluctuations. In the context of this thesis, we employ a discrete random walk model that includes the effect of instantaneous velocity fluctuations on the particles to account for their turbulent dispersion. A particle experiences instantaneous velocity fluctuations which are given by:

$$(u') = \zeta\sqrt{\overline{u'^2}} \tag{3.3}$$

where ζ is any normally distributed random number and the right side term is the root mean square (RMS) value of the velocity fluctuations. Given that turbulent kinetic energy is known at every location, the RMS value For $k - \varepsilon$ or $k - \omega$ models (with assumption of isotropic turbulence) can be taken as [22]:

$$(u') = \sqrt{\frac{2k}{3}} \tag{3.4}$$

Now, the total velocity experienced by the particle would be:

$$(u) = \overline{u} + u' \tag{3.5}$$

where $\overline{u}$ is the local Reynolds-averaged velocity u' is the induced velocity fluctuation. Now, this DRW model is supplied to the Particle model via *User-defined body force* on StarCCM+. The force is directed towards the geometric centre of the Ahmed Body by computing the normal vector pointing towards the respective surfaces and is enforced all through the RANS operated regions (Refer Appendix B).

3.2.6.5 Particle Re-suspension Model

Particles upon collisions with a surface, can either adhere indefinitely on to that surface or it can suspend away. So, a particle re-suspension model is implemented for the same. At the wall, the formulation of Reynolds number is similar to that of the dimensionless wall distance (y+). It is given by:

$$Re_P = y+ = \frac{U_\tau D_P}{\nu} \tag{3.6}$$

where U_τ is the friction velocity and ν is the kinematic viscosity of the fluid phase. This model is being proposed on basis that contamination prevails in those regions corresponding to a threshold value of particle Reynolds number (Re_P), less than that for which particles suspend away. The implementation of this re-suspension model is as follows:

1. A region on the bluff body for which no snow deposition persists in the experiments is identified.
2. Then, the corresponding Re_P at that location within the simulation is looked upon.
3. Now, this value of Re_P is considered to be a threshold value beyond which every other particle re-suspends while the particle below this value adheres to the surface.

In case of the Ahmed body, it is identified from the experiments that no particles deposit on the front surface. Correspondingly, the minimum value of Re_P along that that surface is chosen to be the threshold value. Particles with Re_P beyond this value along rest of the surfaces are considered suspended.

4

Results and Discussions

In this chapter, experimental (wind tunnel) results and the results obtained from the simulation will be discussed and compared, for both the Wedge and the Ahmed body.

4.1 The Wedge: Experimental Results

Snow deposition study was performed by varying the run-time of the test at an interval of five minutes, starting from five minutes to fifteen minutes keeping a consistent wind speed of $70 km/h$ maintained at a temperature of $-15°C$.

(a) 5 minutes **(b)** 10 minutes **(c)** 15 minutes

Figure 4.1: Snow deposition from the front view of the Wedge for different run-times

Figure 4.1 shows the front view of the Wedge which is facing the nozzle. The formation of a small patch of snow deposition was rather random since it occurred at slightly different locations during each trial. However, noticeable difference in frost formation with increased run-time can be observed.

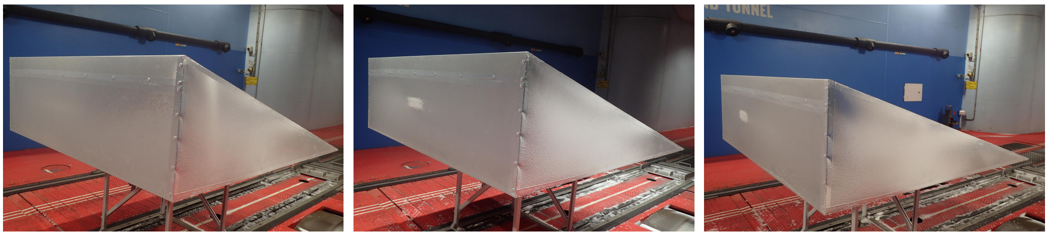

(a) 5 minutes **(b)** 10 minutes **(c)** 15 minutes

Figure 4.2: Snow deposition from the front left view of the Wedge for different run-times

Figure 4.2 shows the front right view of the Wedge. Snow deposition pattern becomes more significant at the mid-section and at the leading edge as the time duration increases. However, there are clear regions on the upper side of the leading edge and at the trailing end. This is probably due to the flow separation zones just after separation at the leading and trailing ends respectively.

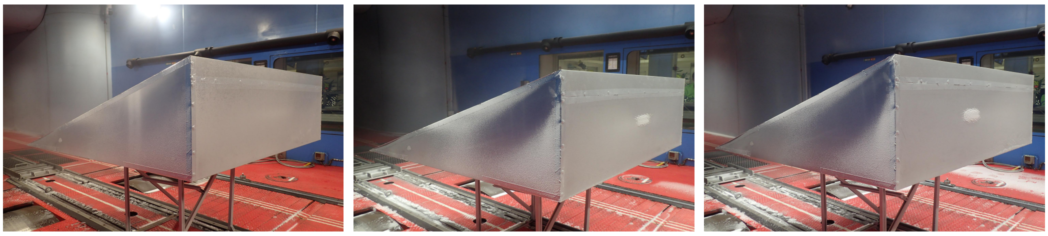
(a) 5 minutes **(b)** 10 minutes **(c)** 15 minutes

Figure 4.3: Snow deposition from the front right view of the Wedge for different run-times

Figure 4.3 shows the front left view of the wedge where there is a more distinguishable pattern with the increase in run-time. The flow separation regions are observed in a similar manner as in the front right view.

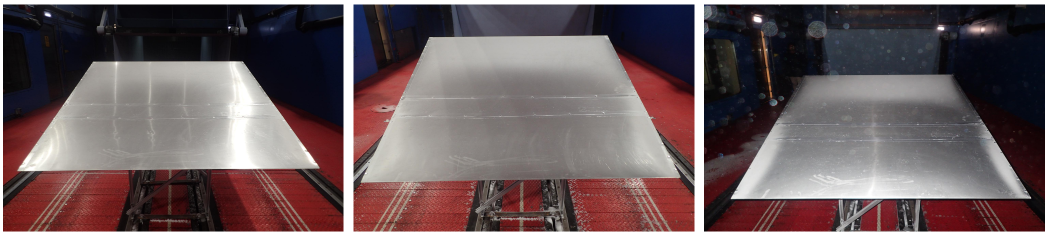
(a) 5 minutes **(b)** 10 minutes **(c)** 15 minutes

Figure 4.4: Snow deposition from the rear view of the Wedge for different run-times

Figure 4.4 shows the rear view of the wedge where there is clear visibility of snow deposition pattern with increase in run-time. Deposition throughout the upper edge, lower half of left and right edges are observed. However, the deposition at the bottom edge is more distinguishable at longer run-time.

Normally, defrosting should be conducted after every test run in order to avoid clogging of ice on the snow cannon and also to avoid the risk of damaging the wind tunnel fan blades due to the excessive build up of ice on it. However, in this experiment it was not possible.

Hence, we could not account for repeatability because of problem from defroster or the run-time of wind tunnel was very short. On the other hand, this experiment has given valuable insight about other things including minimum required run-time to obtain distinguishable deposition pattern.

4.2 The Wedge: Simulation Results

4.2.1 Baseline Configuration A

In order to be able to perform multi-phase analysis, it is important to setup a proper aerodynamic case initially. Hence, a baseline simulation for aerodynamic analysis is established to obtain a fully developed flow field.

4.2.1.1 Aerodynamic Simulation

The wedge was simulated to understand the overall aerodynamic flow field around the bluff body. Using Line Integral Convolution (LIC) technique, the mean velocity vector field around the bluff body can be visualized (4.5). From the side-view, it can be seen that there is a re-circulation zone just below the bluff body by the leading edge while they are bigger at the upper surface. From Figure 4.5, it is also evident that there is a wake formation at the front, on the bottom surface and an attached wake further downstream by the trailing end extending further downstream. From the top view, the wake is observed to be present throughout the span-wise direction. Also, there is a stagnation zone by the tip and a flow separation just after the leading end of the bluff body.

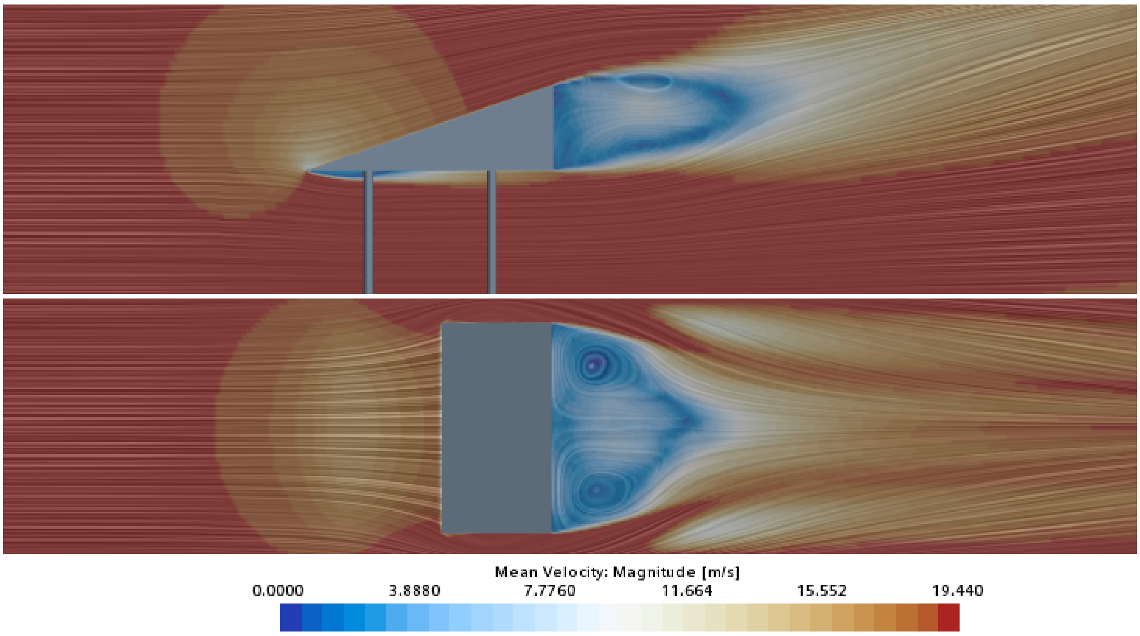

Figure 4.5: Line Integral Convolution of time averaged velocity vector fields, plane-section view

Figure 4.6 depicts the distribution of mean of total pressure. From the side view, it is seen that a negative pressure zone is formed just below the leading edge due to flow separation. It is then followed by a larger negative pressure zone at the rear section, which is indicative of the formation of wake. Further, from the top view it is visible that flow separation occurs along the sides which eventually re-attaches.

Later, upon exiting the side surface, two major re-circulation zones are formed further downstream of the rear section which gradually fades away.

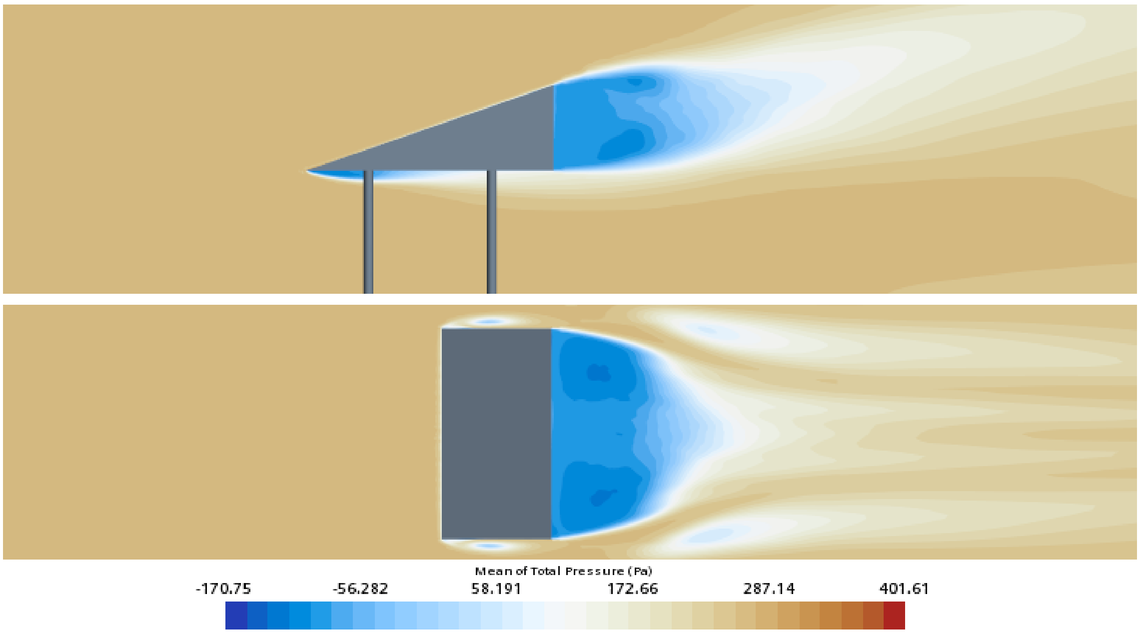

Figure 4.6: Mean of Total Pressure field

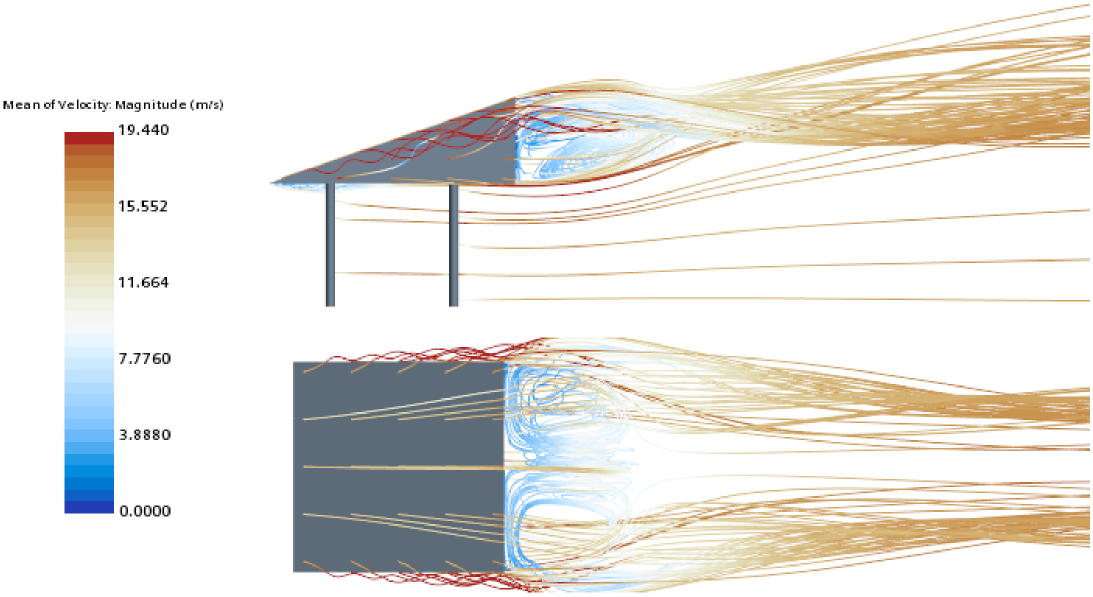

Figure 4.7: Velocity streamlines of Mean of Velocity: Magnitude

Furthermore, it would be important to look closely into the velocity streamlines to analyse the flow in detail. Figure 4.7 depicts the velocity streamlines of the mean velocity field. It is seen that the flow is attached to the slant surface as it flows past the surface and a recirculation region with less velocity is seen at the rear surface.

The flow on the sides look to be of high magnitude and is attached to the surface of the Wedge. These streamlines are generated using forward integration of the 4th order Runge Kutta (RK) method.

It is seen from Figure 4.8 that the mean wall shear stress is very low at the leading end which can be related to the flow separation in that region while it is relatively high at the corners of the rear surface and further reduces close to the centre. This shows that the wake formed at the rear is closer to the surface at the corners while the wake around the centre plane is slightly far downstream. Along the side surfaces, the flow seems to be attached along the middle portion of the surface while the flow separation induced at the beginning tends to detach the flow towards the upper and lower edges of that surface.

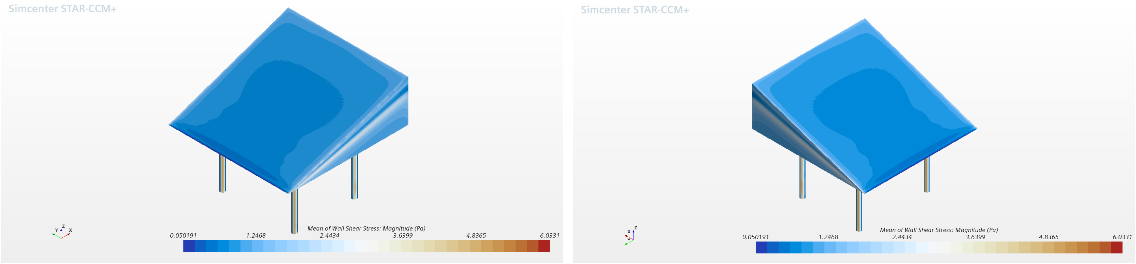

Figure 4.8: Mean of Wall Shear Stress

4.2.2 Configuration B

4.2.2.1 Aerodynamic Simulation

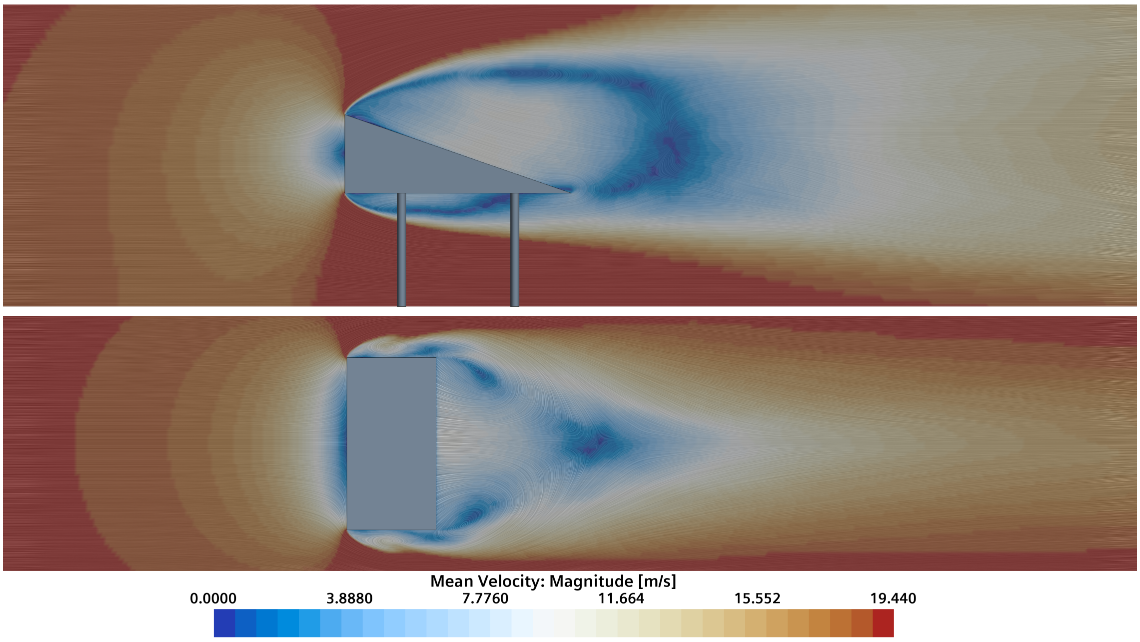

Figure 4.9: Line Integral Convolution of time averaged velocity vector fields

For the baseline simulation, the Wedge was simulated to understand the general aerodynamic flow field around the bluff body as per configuration B. Looking at the top view, two re-circulation zones are visible by the side of the bluff body and from the side-view, it can be seen that there is a re-circulation zone just below the bluff body while there is a slightly wider re-circulation zone just above the bluff body. From Figure 4.9, it is also evident that there is a large wake formation around the bluff body by the downstream, which, from the top view, is observed to be concentrated around the centre plane. There is also a stagnation zone just before the leading face of the bluff body followed by a flow separation zone.

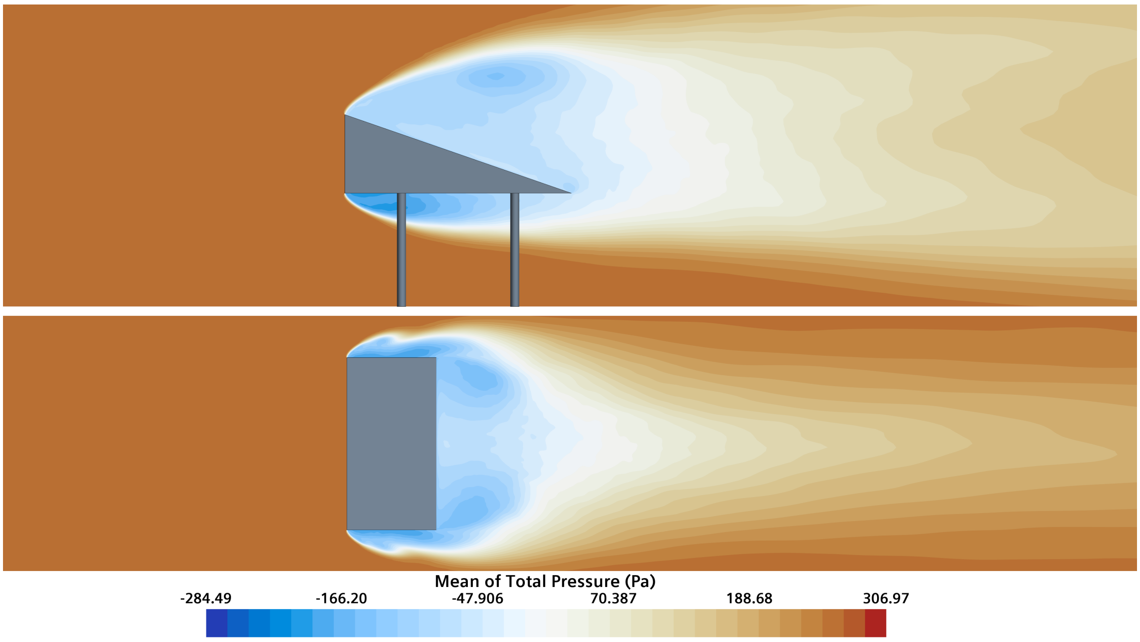

Figure 4.10: Mean of Total Pressure field

Figure 4.10 depicts the mean of total pressure field distribution. It can be seen from the top view that there is a high-pressure zone at the front surface while a negative pressure zone exists on either sides. There are two recirculation zones where the pressure is negative with relatively high intensity in the bottom half of slant surface region. Looking at the side-view, it can further be observed that there is a negative pressure zone on the entire slant surface region and also the bottom surface indicating the separation of flow from both top and bottom edges of the front surface. This flow later joins the wake and forms two recirculation regions and exits the wake.

Furthermore, it would be important to look closely into the velocity streamlines to analyse the flow in detail. Figure 4.11 depicts the velocity streamlines of the mean velocity field. It is seen that the flow hits the front surface of the Wedge and follows the surface in all directions and then separates along the top and side edges. These streamlines try to come back towards the slant surface and form two big recirculation zones and then follow the flow direction towards the bottom part of the slant surface. These streamlines are generated using forward integration of the fourth order RK method.

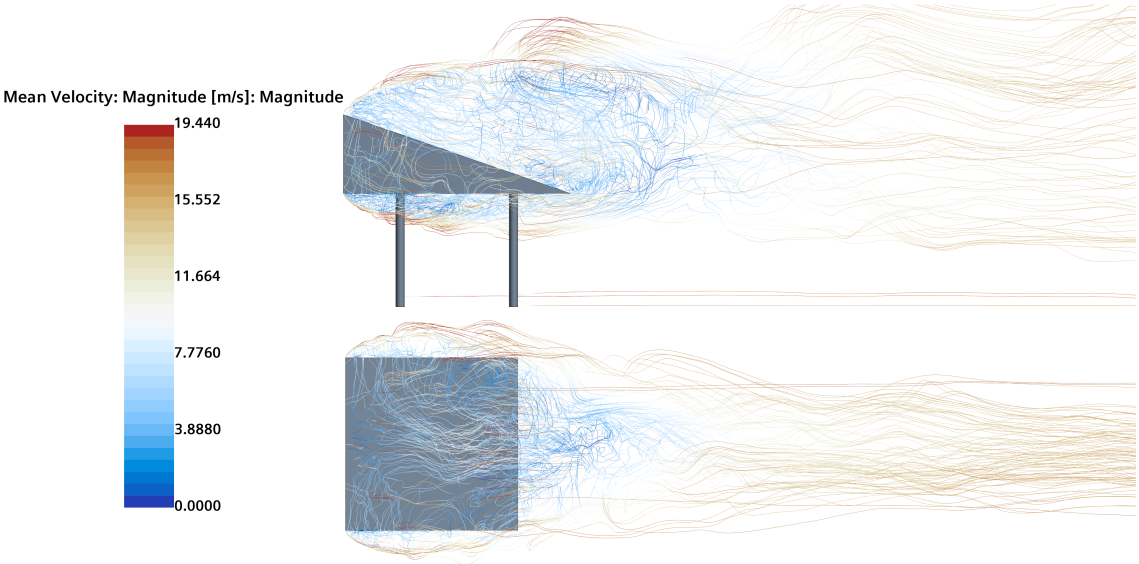

Figure 4.11: Velocity streamlines of Mean of Velocity: Magnitude

It is seen from Figure 4.12 that wall shear stress is relatively higher along with the corners of the front face, between the middle and trailing end of the side faces and along the lower half of the upper face. This seems to hold relating to our previous knowledge that there exists a flow separation zone along the front face which causes the flow to detach from the surface. Hence, higher wall shear stress gradients can be seen if either the flow is not separated or after it retracts back from separation.

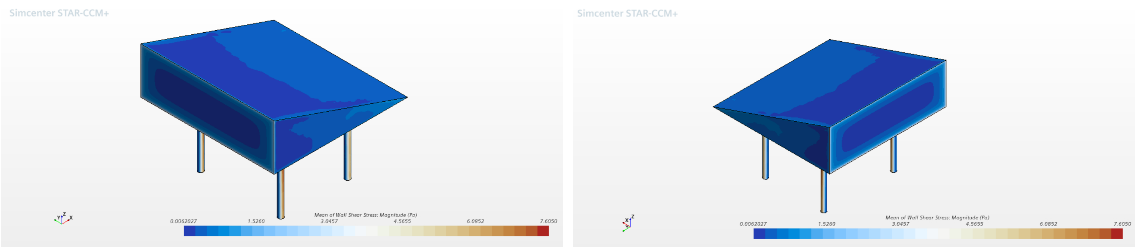

Figure 4.12: Mean of Wall Shear Stress

4.3 Ahmed Body: Experimental Results

A study was performed for different slant angles of the Ahmed body for thirty minutes keeping a consistent wind speed of $115 km/h$ maintained at a temperature of $-15°C$. Below presented are the results from one of the trials for each of the slant angle configurations (For snow deposition pictures from other trials refer Appendix..).

4.3.0.1 Slant Angle 35°

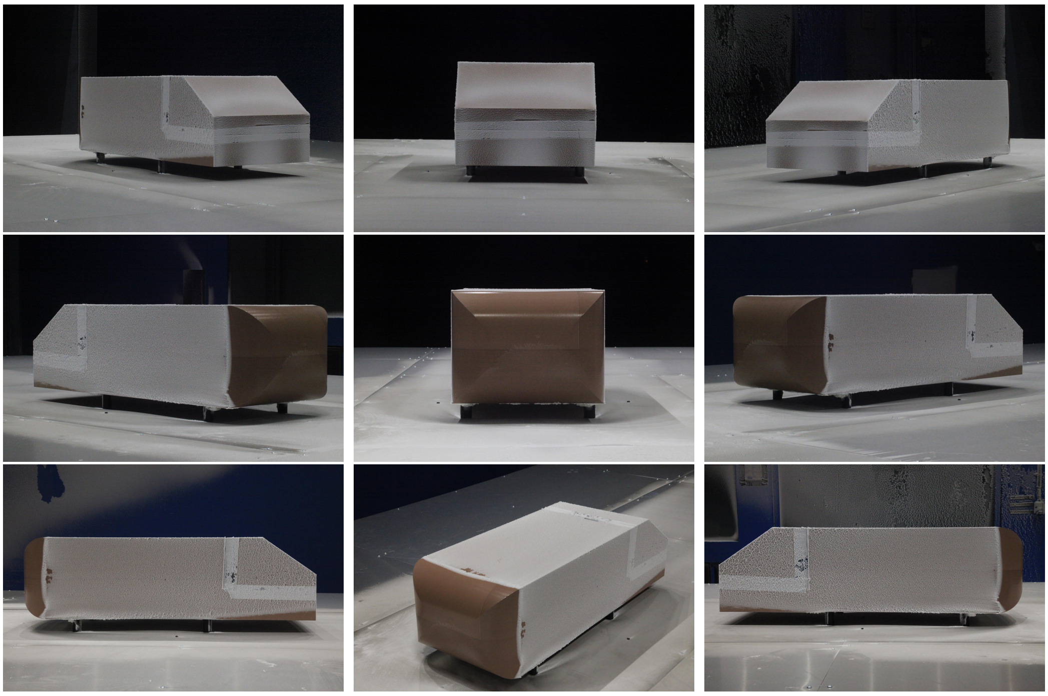

Figure 4.13: Snow deposition on Ahmed body with slant angle 35° in the wind tunnel

The slant angle of 35° was chosen for the first test. The results were observed from the below figure 4.13. The front portion of Ahmed body doesn't have any snow deposition. The sides and top are covered in snow uniformly. It can also be observed that there is no deposition of snow at the rear bottom corner on both the sides, the reason for which is still unclear.

At the rear surface, there is more deposition in the center and the corners. The reason might be due to the recirculation of snow in the wake region. There is a curved pattern on the slant face where there is more deposition of snow.

4.3.0.2 Slant Angle 10°

Similar to the 35° angle configuration, there is no snow on the front surface. The snow cover is similar to the previous case on the sides and top with uniform snow deposition. On the rear surface, the pattern of snow deposition is similar to previous case however the intensity is less in the center of the surface. On the slant face, the snow deposition is is visible throughout the entire face but there is significant snow cover along the left and right edges increasing in area from top to bottom as seen in Figure 4.14. A curved pattern is not seen here as in the previous configuration.

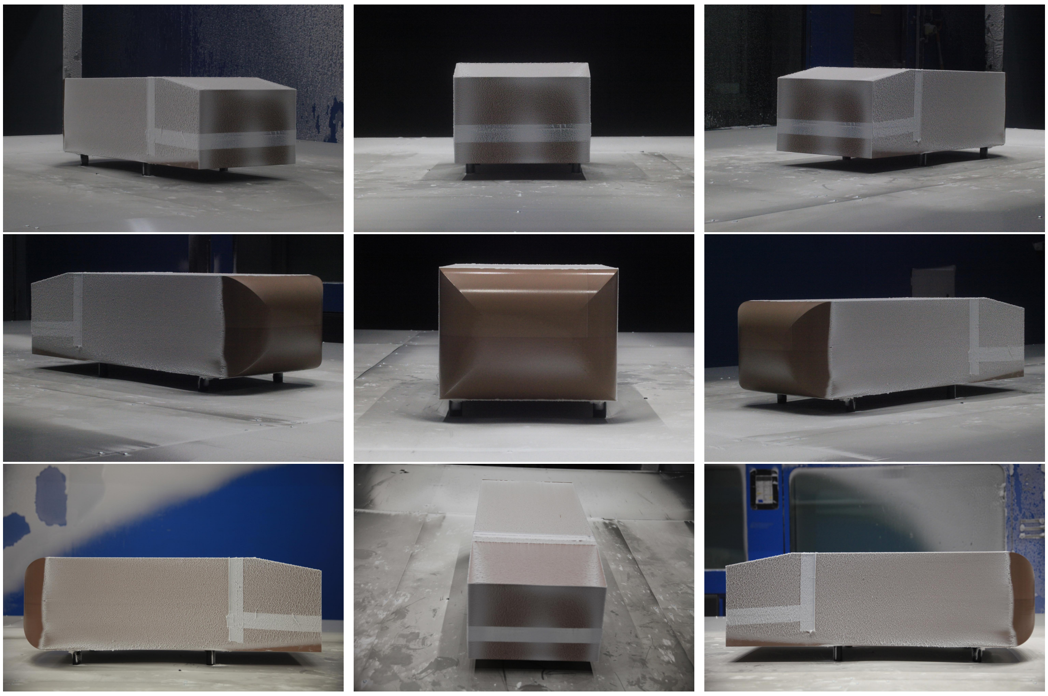

Figure 4.14: Snow deposition on Ahmed body with slant angle 10° in the wind tunnel

4.3.0.3 Slant Angle 25°

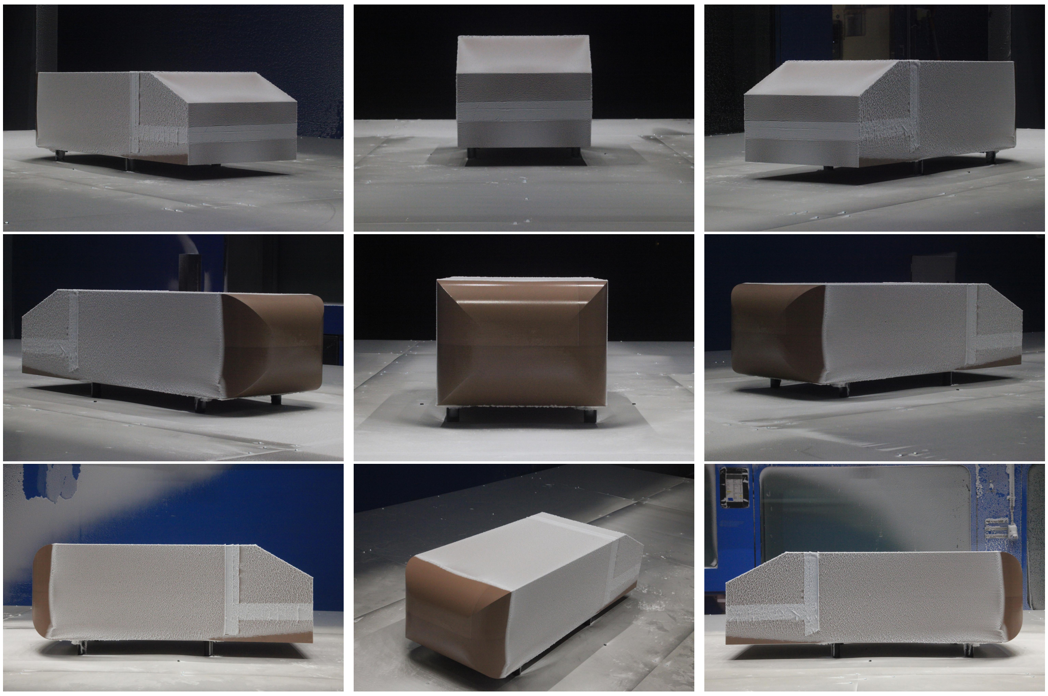

Figure 4.15: Snow deposition on Ahmed body with slant angle 25° in the wind tunnel

The snow deposition on the slant surface in this case can be seen as a blend of characteristics of the slant angles 10° and 35° configurations. From Figure 4.15, it can be seen that there is a C-shaped pattern of snow accumulation as seen in the 35° case (Figure 4.13) and also snow cover along the edges which is similar to the characteristics seen in the 10° case (Figure 4.14). The description of snow cover on the sides, top and front is similar to the previous two cases. The pattern of snow deposition at the rear is similar to the previous cases but the intensity of deposition is in between that of 10° and 35° configurations.

4.3.0.4 Tuft Experiment - Slant Angle 10°

The Ahmed body with tufts was subjected to a wind speed of $115 km/h$ for few minutes and it was observed that the tufts was attached to the surface of the body in the direction of the wind as seen in Figure 4.16. This means that the flow is attached along all the surfaces where the tufts are placed. If the tufts were not stuck to the surface and suspending in the air, then it could have been concluded that the flow was detached from the body.

Figure 4.16: Tufts on Ahmed body with slant angle 10° subjected to wind speed in the wind tunnel

4.3.0.5 Repeatability Study

Unlike the Wedge experiment, the Ahmed body experiment trials displayed really good repeatability for 25° and 10° slant angle configurations. It can be observed that there is a consistent pattern of snow deposition for these slant angles after all trials were conducted using the respective slant angle rear blocks as seen in Figures 4.18 and 4.19 representing slant angle trials of 25° and 10° respectively. However, minute snow-less patches were observed during the first two trials of 35° configuration as seen in Figure 4.17.

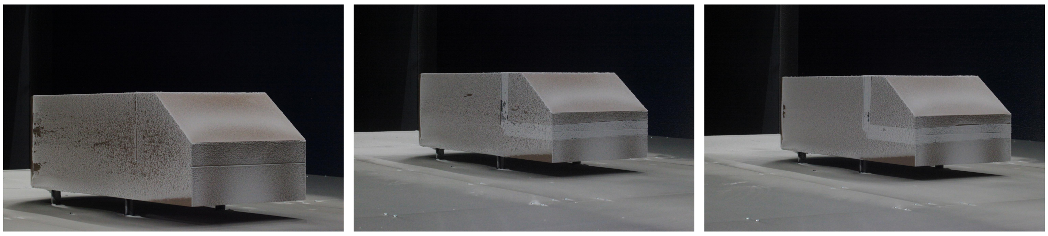

Figure 4.17: Repeatability study of snow deposition on Ahmed body with slant angle 35° in the wind tunnel of 3 trials

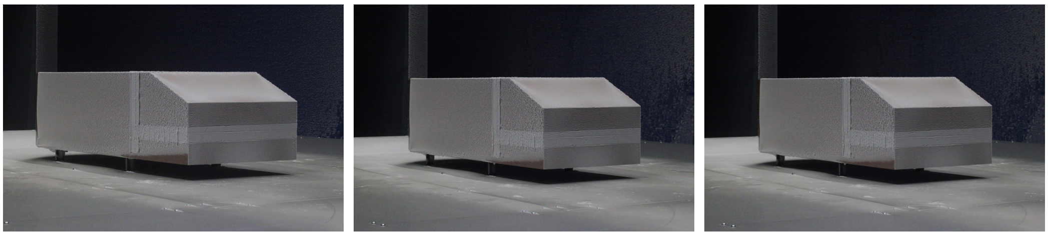

Figure 4.18: Repeatability study of snow deposition on Ahmed body with slant angle 25° in the wind tunnel of 3 trials

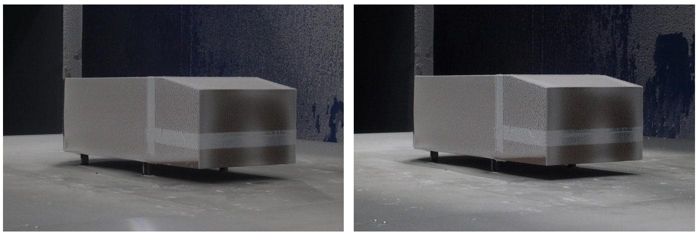

Figure 4.19: Repeatability study of snow deposition on Ahmed body with slant angle 10° in the wind tunnel of 2 trials

4.4 Ahmed Body: Simulation Results

4.4.1 Baseline Configuration: Slant angle 25°

4.4.1.1 Aerodynamic Simulation

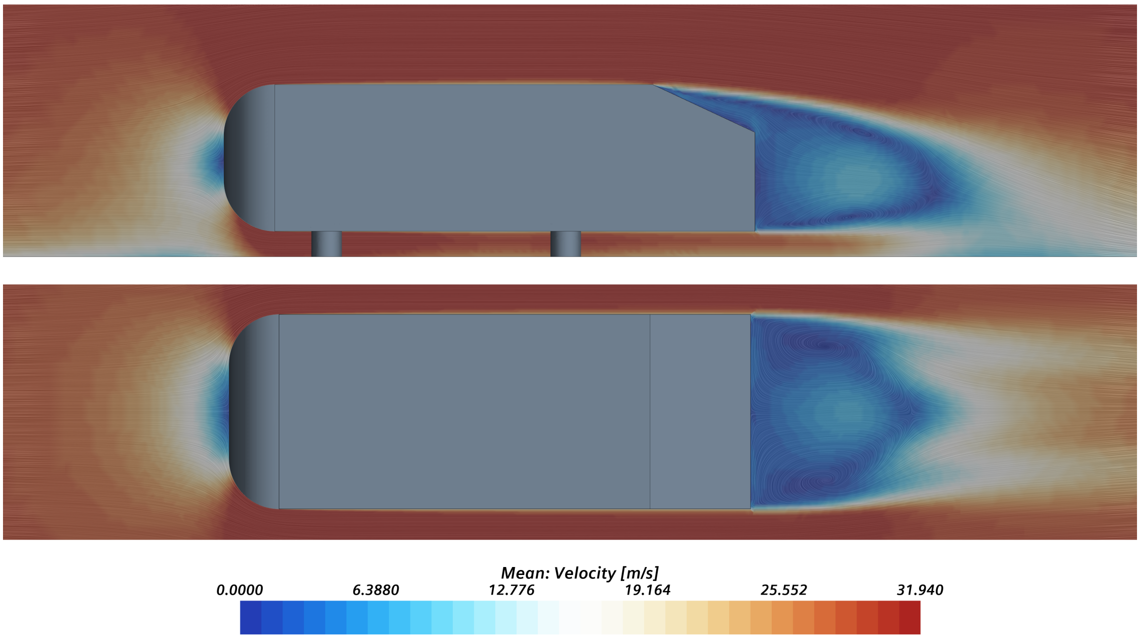

Figure 4.20: Line Integral Convolution (LIC) plot of mean velocity magnitude

The Line Integral Convolution (LIC) vector plot of Mean Velocity as depicted in Figure 4.20 is used as a visualization technique to investigate the general flow field around the Ahmed body. At the front section, it can be seen from the side view that the stream-wise flow tends to flow along the curvature initially, causing a stagnation region to be formed. The flow is however not detached and they continue along the mid-span. The slant surface causes flow separation at the rear section, which enables the formation of the wake region. Further downstream along the wake, two re-circulation regions can be observed as can be seen from the top view. Furthermore, these wake structures eventually meet far downstream. One can note that the velocity is significantly low at these regions along the front and rear section respectively.

Also, from experiments conducted in [31], it is known that for a slant angle of 25°, the flow re-attaches just before the end of the slant surface. Similar inference can be drawn for the baseline simulation when looked at the near-wall region along slant surface that a re-circulation zone is causing the flow to re-attach.

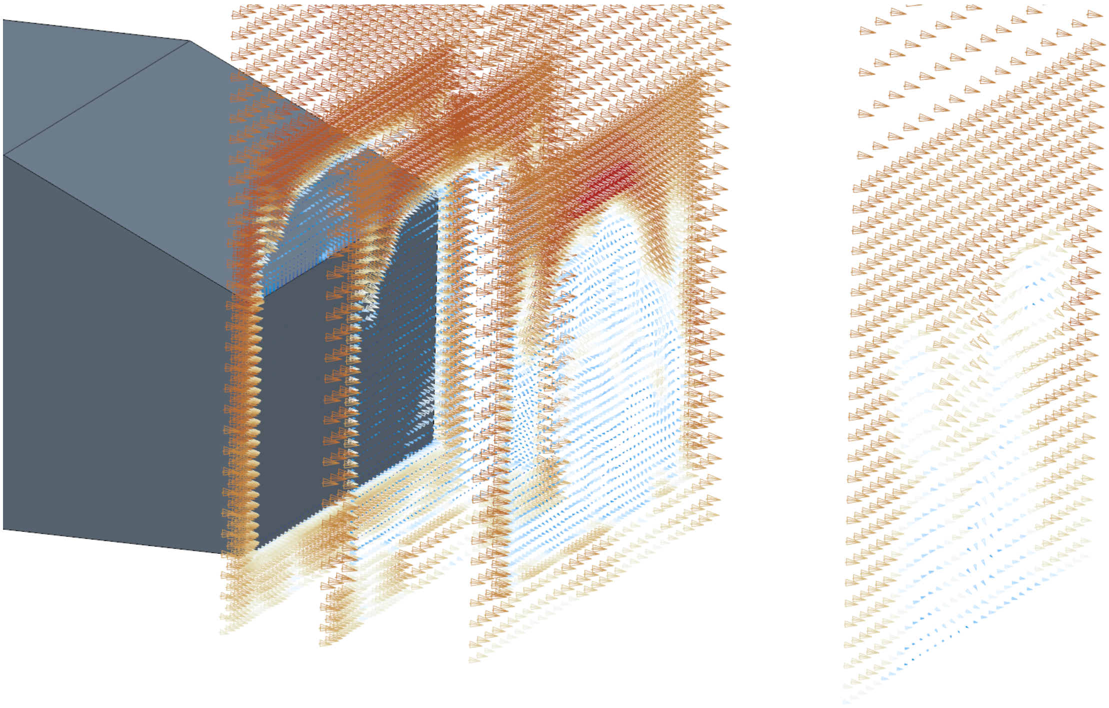

Figure 4.21: Velocity vectors at various x-locations; x = 0 [mm], x = 80 [mm], x = 200 [mm], x = 500 [mm]

Figure 4.21 shows the various yz-planes along which mean velocity vectors have been studied for visualizing the direction of wake structures. It can be clearly seen from Figures 4.22a, 4.22b, 4.22c and 4.22d respectively that the vortices along either of the top corners of the slant surface develop eventually into a cone-like structure and along counter-rotating directions w.r.t each other. These counter-rotating vortices trail along with the downstream as the wake region grows. Besides, it can also be observed that a roller-pin shaped vortex at the upper edge of the slant surface eventually develops into a U-shaped vortex or Horse-shoe vortex which is a classical flow feature in this case (i.e. with rear slant angle of 25°).

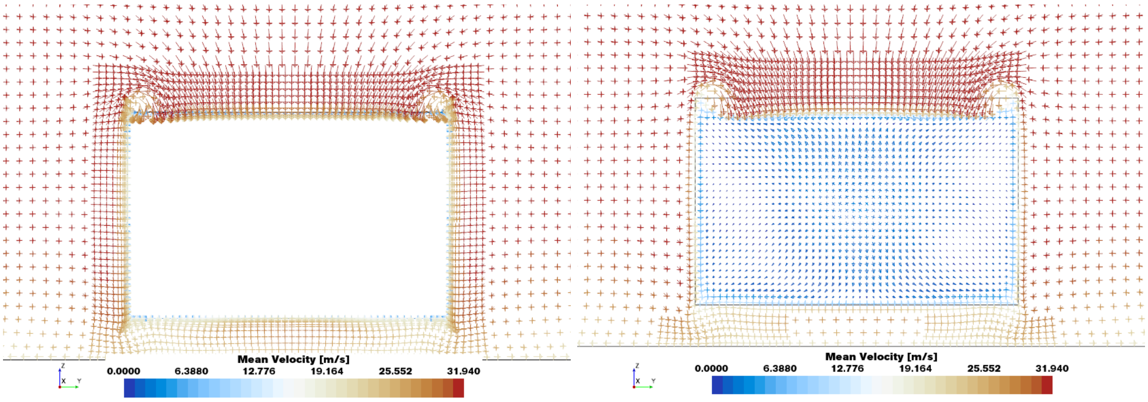

(a) x=0 **(b)** x=50

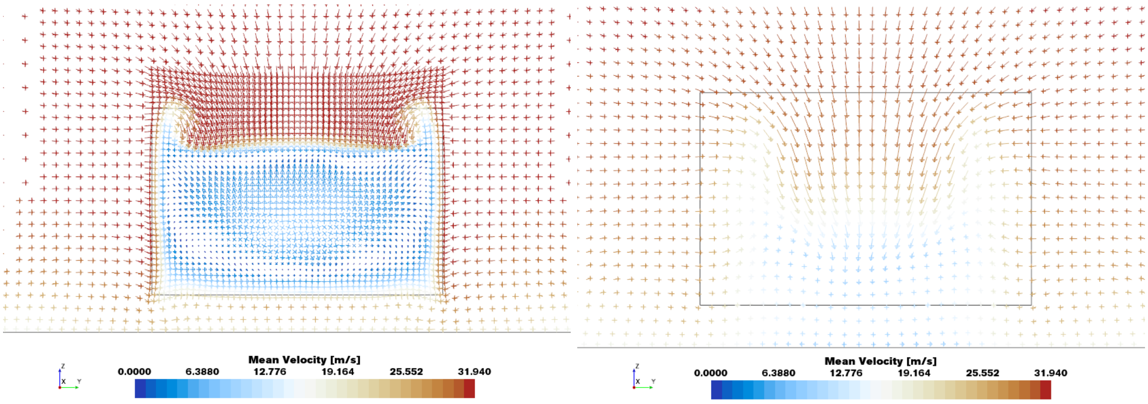

(c) x=200 **(d)** x=500

Figure 4.22: Velocity vectors along various x stations [m]

Figure 4.22 depicts the movement of fluid in the direction of flow in the rear wake region by visualizing the mean velocity magnitudes at various x-stations - 0mm, 80mm, 200mm and 500mm respectively. This is another method that gives a better idea of the variation of mean velocity magnitudes and their direction at the slant and rear surface. Using this knowledge, one can predict the turbulent structures, vortex formations and the formation of wake in the rear.

Figure 4.23 represents the contour of total pressure around the bluff body. The bluff body experiences drag primarily due the the difference in pressure between the leading end and the trailing end respectively. Larger the pressure difference, higher the drag experienced by the bluff body. It can be seen from the figure that the streamline curvature at the front induces a pressure difference closer to the surface, throughout the mid-span of the bluff body. This extends further downstream where the rear (wake) region is predominantly a low pressure region.

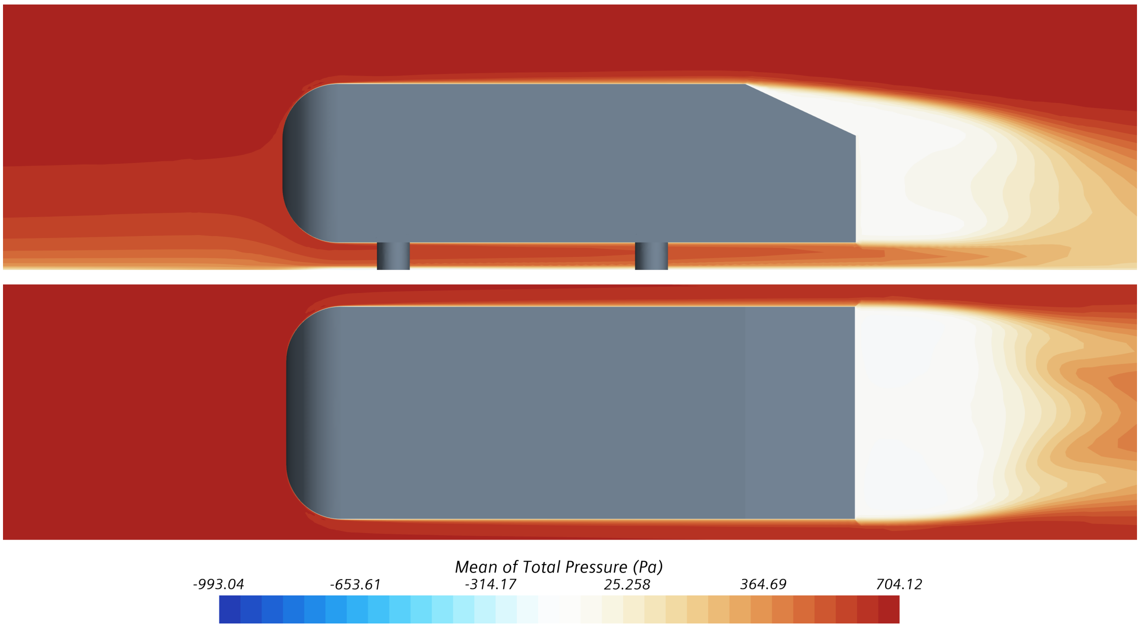

Figure 4.23: Pressure distribution around the Ahmed body visualized by contour plot of Mean Total Pressure

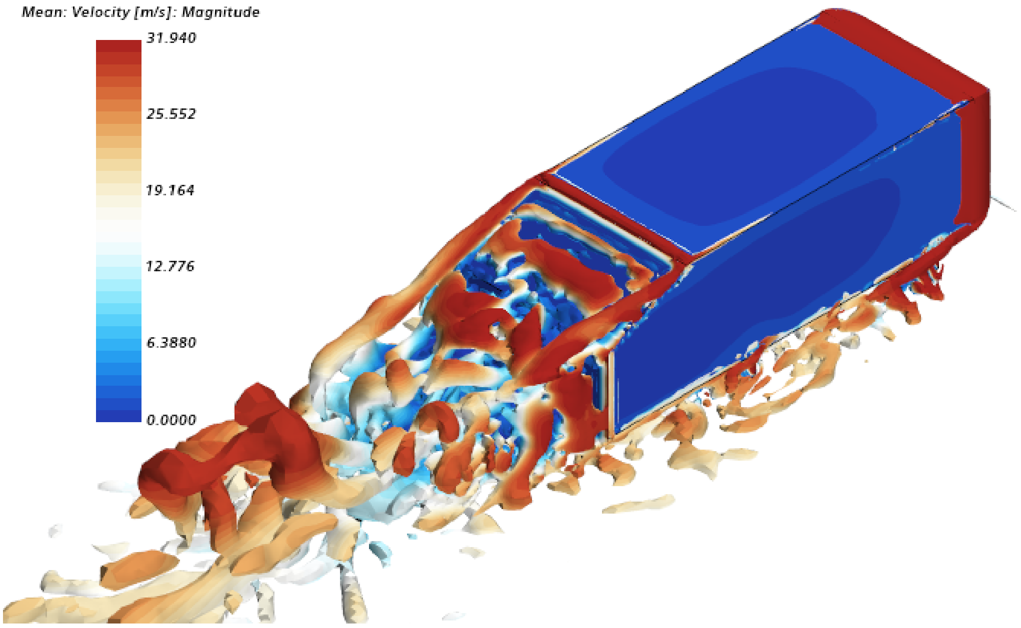

Figure 4.24: Turbulent vortices around the Ahmed body visualized by Q-criterion ($Q = 10000/s^2$)

Coherent three-dimensional vortices can be visualized by the means of Q-criterion. According to this criterion, the formation of vortex structures happens at regions where the Eucledian norm of vorticity tensor dominates the shear-strain tensor (i.e. $Q = \frac{1}{2}||\Omega^2| - |S^2||>0$). Figure.4.24 depicts the Iso-contour of Q-criterion from baseline simulation coloured by mean of velocity magnitude. Flow at the front section of the bluff body is mostly shear-strain dominated and hence there are no vortices seen. Also, the mid-span of the bluff body along the top and side surfaces are free from vortex formations. However, we can see the presence of a rolling pin like vortex by the trailing end of the roof, just before the flow separation. Further on, this vortex eventually gets bent into a U shaped structure or commonly known as *'Horseshoe vortex'*. The presence of inclined surface downstream (Here, 25°) causes the flow to separate and hence the flow is pulled back in the low-pressure zone just above the slant surface, leading to the formation of cone-shaped vortices on either edge. The development of wake due to effect of undersurface upsweep is similar to that of slant angle. The slant angle persuades the flow to go downward and inward towards the rear surface whereas the undersurface upsweep persuades the flow to go inward but in the upward direction. These observations are very similar to that recorded from experiments in Ahmed et al. [31]. Besides, it is also seen that significant vortices are present at the bottom surface, which is due to the existence of stilts but not of primary importance for this study.

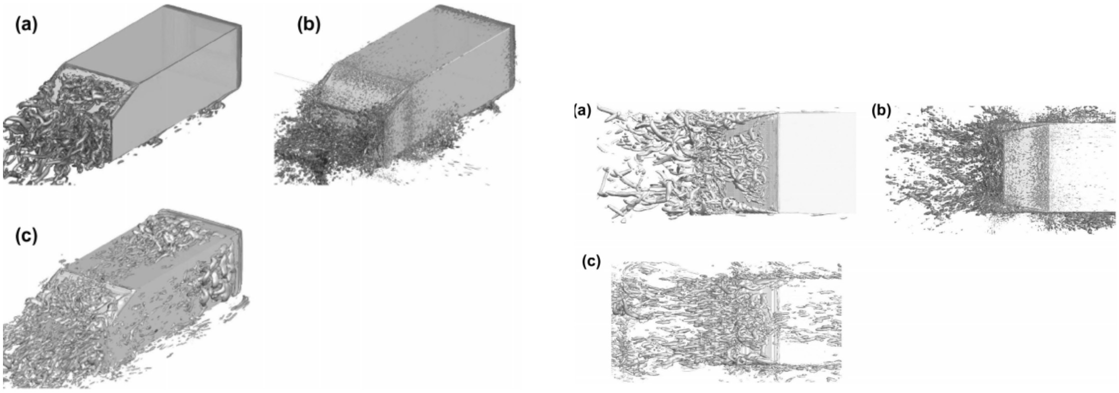

Figure 4.25: Vortex structures around the Ahmed body visualized by iso-surfaces of Q-criterion; Left and right figures represents the Isometric and Top views from Literature respectively(*adopted from [9]).

Figures 4.25 shows the iso-contours of Q-criterion for an Ahmed body with 25° slant angle. These illustrations have been adopted from [9] for reference purpose only. A comparison of vortex formations as predicted using different approaches((a) DES-SST, (b) LES-Near Wall Resolved (NWR) and (c) LES-Spectral Vanishing Viscosity (SVV) respectively) have been presented. It can be seen that rear wake structures are much similar to each other in all the approaches. However, the LES approach predicts the presence of vortex structures of much smaller size and along the side and top surfaces also. This is evident from the predictions from the LES-SVV approach, where turbulent vortices along top and side surfaces are being predicted when a finer mesh which captures turbulent structures at the smallest grid scales and lower values of effective viscosity are being used [9].

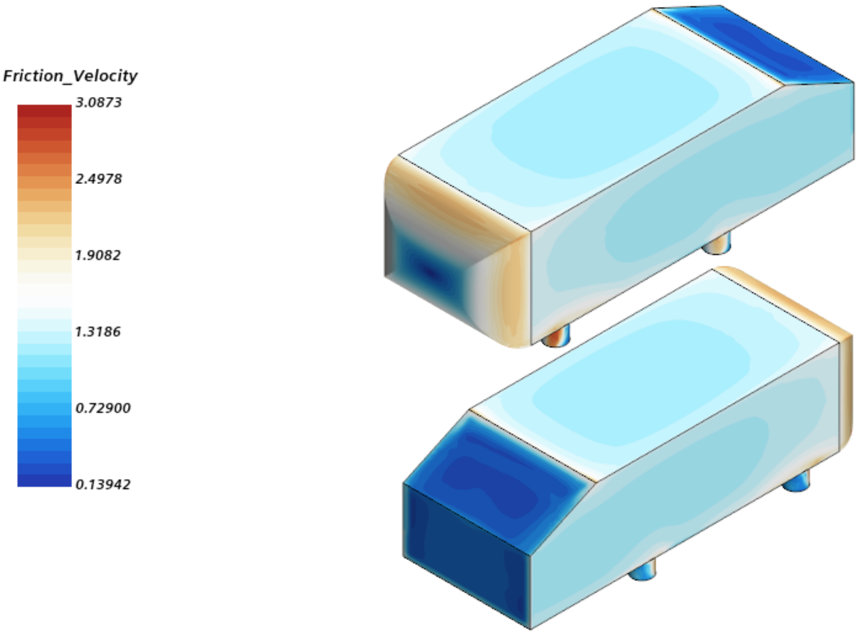

Figure 4.26: Shear velocity profile on Ahmed body with slant angle 25°

As the fluid flows over a surface, there exists a shear force between the surface and the fluid. This shear force or aerodynamically termed as Wall shear stress is that parameter on which turbulence is scaled accordingly. In order to represent the shear strength, a velocity scale is employed to characterize the shear at the boundary. This velocity scale is called the shear velocity or the friction velocity (U_τ). It is given by:

$$U_\tau \; = \sqrt{\frac{\tau_w}{\rho}} \tag{4.1}$$

Where τ_w is the wall shear stress and ρ is the density of the surrounding fluid[2]. At the front surface, shear velocity is at its highest except for a small portion at the middle section. At the sides, it is relatively high at the leading edge while it gradually decreases further downstream. It is considerably high at the edges as well. As of the top surface, it is relatively high at the edges but considerably higher towards the trailing edge or immediately before the slant surface. On the slant surface however, significantly higher values are seen at the upper corner, lowest just below and bow shaped banded region at the middle where it is lowest again. The rear surface is also similar in the sense that shear velocity is largely very less compared to other surfaces. It is lowest along the corners while slightly higher within the inner region.

4.4.2 Slant Angle 10°

4.4.2.1 Aerodynamic Simulation

In order to understand the flow field of the 10° Slant angle configuration a Line Integral Convolution (LIC) vector plot of mean velocity is visualized as seen in Figure 4.27.

As discussed above in the construction of Ahmed body, only the rear block is replaced with slant angle 10°. So the flow features at the front and mid section is the same as described in the baseline configuration. The flow is remains attached throughout slant surface. It can be observed that the velocity magnitude is very low at the rear surface region. From top and side views, it can be seen that there are two re-circulation zones in the near wake region.

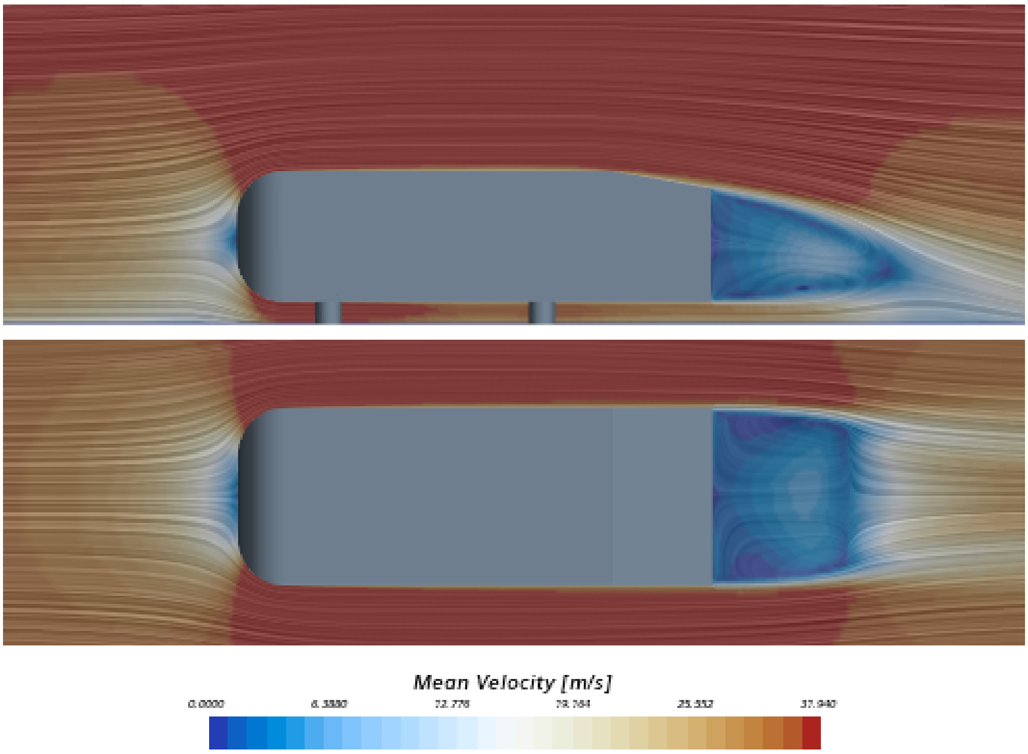

Figure 4.27: Line Integral Convolution (LIC) plot of mean velocity magnitude

Figure 4.28 gives the information of how the flow is progressing and forming wake in the slant and rear surface. Figures 4.28a, 4.28b, 4.28c and 4.28d shows the vectors of mean velocity magnitude at x stations - 0mm, 80mm, 200mm and 500mm respectively. It can be observed clearly that there is formation of vortices in the shape of cone on both the slant edges and it develops until $x = 200mm$ and then disappears at $x = 500mm$. The trailing vortices have the same magnitude of the flow velocity. At $x = 500mm$ station, the flow tends to roll inwards near the rear surface with low velocity.

Figure 4.29 shows the contour of total pressure distribution around the Ahmed body. High Pressure difference is seen very close to the surface from the front curve till the mid-span of the Ahmed body due to the streamline curvature at the front edge of the body. At the slant and the rear regions, the pressure is relatively low when compared to the other areas. The entire wake region starting from the trailing edge of the Ahmed body is a low pressure region.

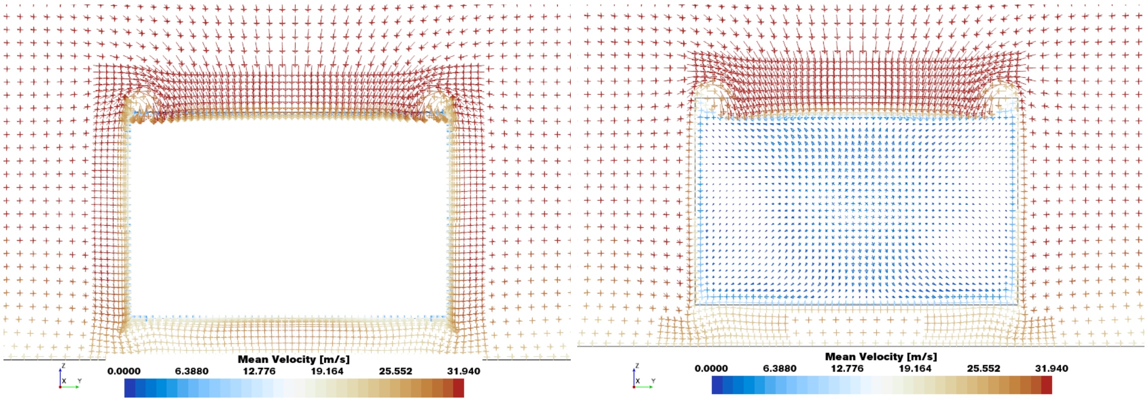

(a) x=0 **(b)** x=50

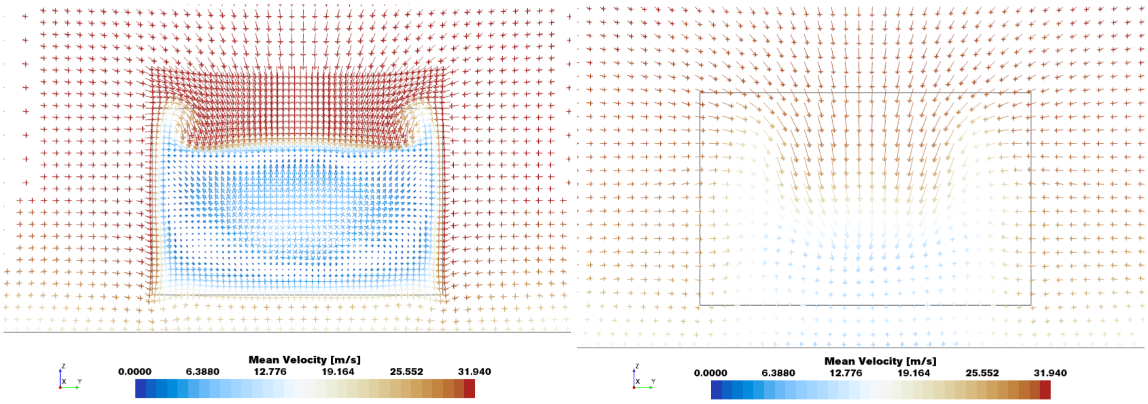

(c) x=200 **(d)** x=500

Figure 4.28: Velocity vectors along various x stations

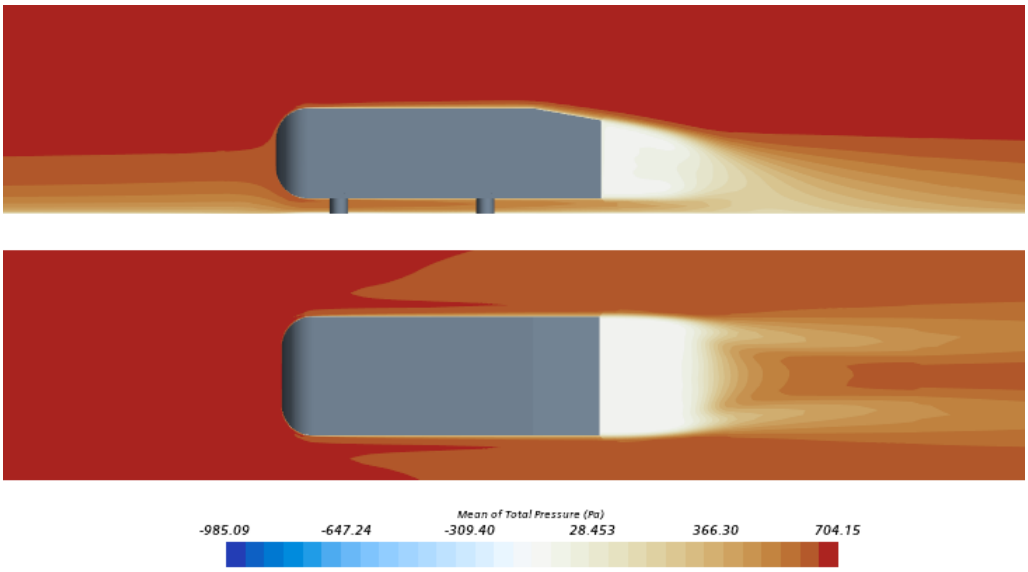

Figure 4.29: Pressure distribution around the Ahmed body visualized by contour plot of Mean Total Pressure

Visualizing the turbulent flow field is another important aspect of the aerodynamic study. In this analysis, vortex formations are seen at the rear region.

As discussed in Section 4.4.1.1, Q-criterion is used as a method to detect formation of vortex structures using iso-surfaces. In this analysis, an iso-value of $1000/\mathrm{s}^2$ is used and it is coloured by the mean velocity magnitude. Since the simulation settings is the same for all the cases, the characteristics are same at the front and mid-span regions.

It can be observed in Figure 4.30 that there is a formation of two counter rotating trailing cone vortices on each side of slant edges. This is because of the momentum generated by these strong vortices. There are horse-shoe vortices or U shaped vortices being formed at the rear wake region as well.

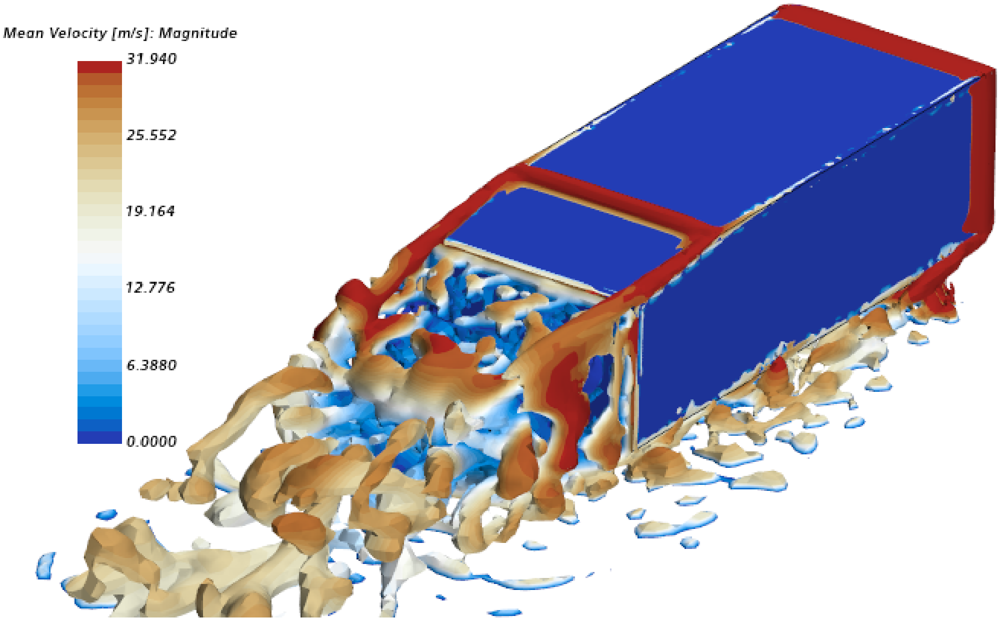

Figure 4.30: Turbulent vortices around the Ahmed body visualized by Q-criterion ($Q = 10000/s^2$)

As discussed in the baseline configuration Section 4.4.1.1, the shear velocity is used to investigate the shear at the surface of the Ahmed body. As seen in Figure 4.31, the friction velocity is comparatively high at the front curvature and also at the bottom of the side surfaces, in relation to other surfaces. The magnitude is considerably low along both the edges of the rear surface. The top and side surfaces have slightly higher shear velocity closer to the front edge while it decreases downstream. On the slant surface, the magnitude of shear velocity is lowest in the middle section and the value increases as we go outwards to the top and side edges.

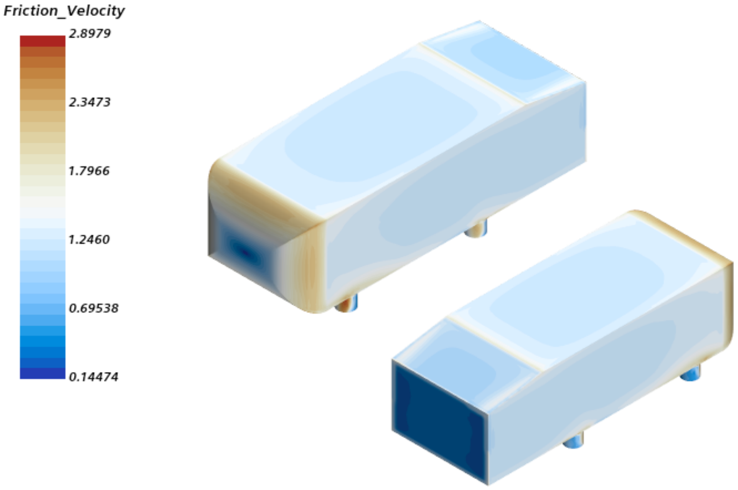

Figure 4.31: Shear velocity profile on Ahmed body with slant angle 10°

4.4.3 Slant Angle 35°

4.4.3.1 Aerodynamic Simulation

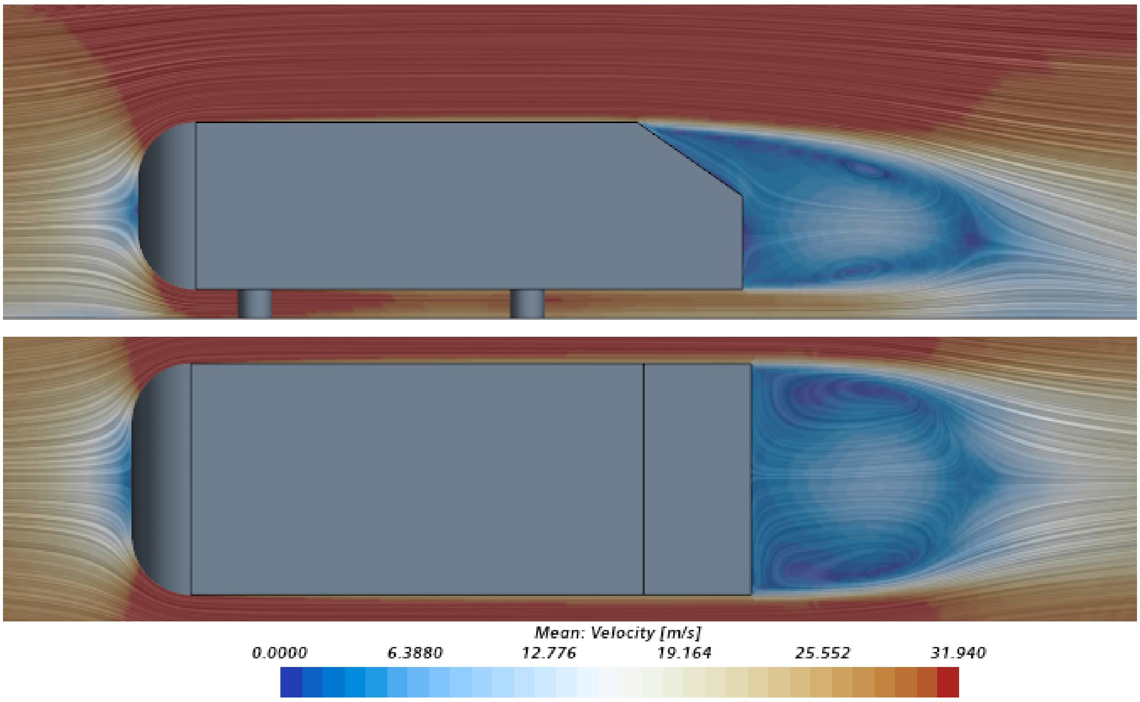

Figure 4.32: Line Integral Convolution (LIC) plot of mean velocity magnitude

In order to understand the flow field of the 35° Slant angle configuration a Line Integral Convolution (LIC) vector plot of mean velocity is visualized as seen in Figure 4.32.

As discussed above in the construction of Ahmed body, only the rear block is replaced with slant angle 35°. So the flow features at the front and mid section is the same as described in the baseline configuration. A huge separation in the flow is observed from the upper slant edge and it never reattaches to the rear surface as seen in Figure 4.32. Two big re-circulation regions are formed in the near wake region which is also extends further from the rear of the Ahmed body as seen from side and top views. These observations are made in comparison with the other two configurations. The velocity is very low in the wake region at the slant and rear surfaces in comparison to that along other surfaces.

Figure 4.33 gives the information of how the flow is progressing and forming wake in the slant and rear surface. Figures 4.33a, 4.33b, 4.33c and 4.33d shows the vectors of mean velocity magnitude at x stations - 0mm, 80mm, 200mm and 500mm respectively. It can be observed clearly that the velocity vectors have high magnitude at top edge of the slant surface but there is very low magnitudes of mean velocity throughout the rest of the slant and rear surfaces on the 1st three stations. This indicates a bigger separation region as soon as the slant surface is reached when compared with the other two configurations. At $x = 500mm$ station, the flow tends to roll inwards near the rear surface to form two big re-circulation zones in the wake region.

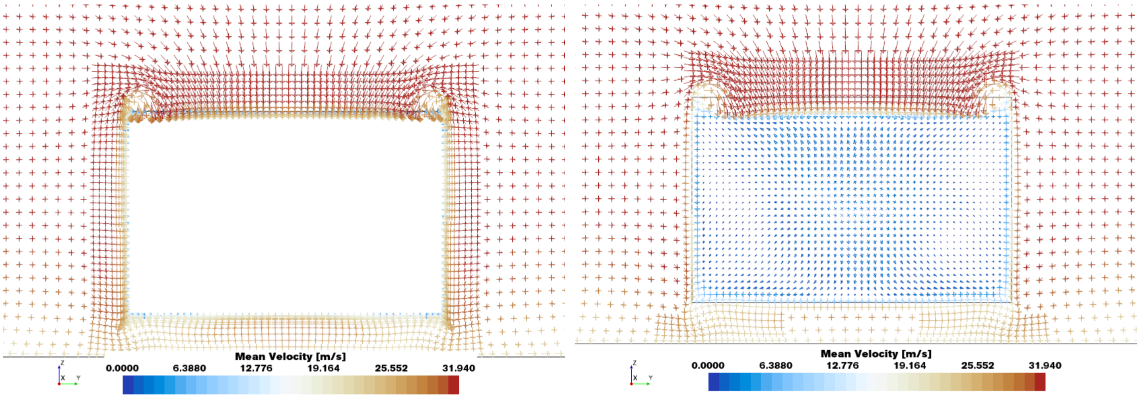

(a) x=0 **(b)** x=50

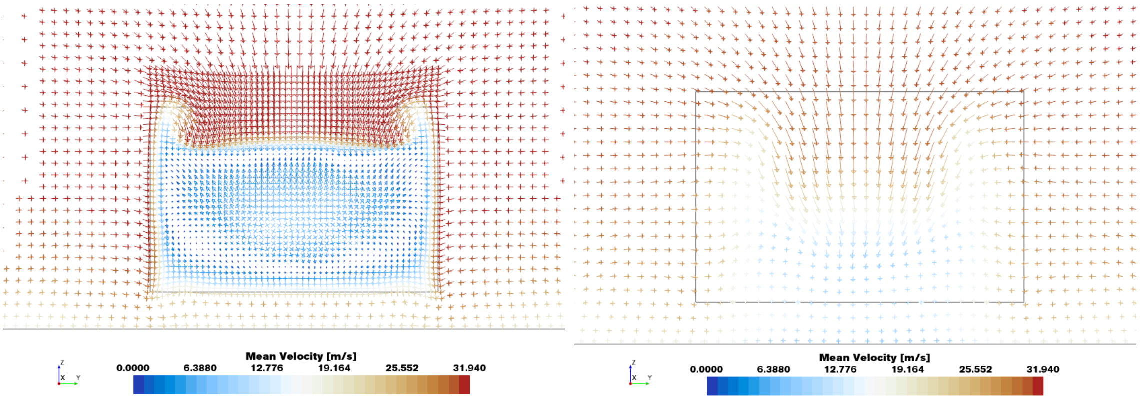

(c) x=200 **(d)** x=500

Figure 4.33: Velocity vectors along various x stations

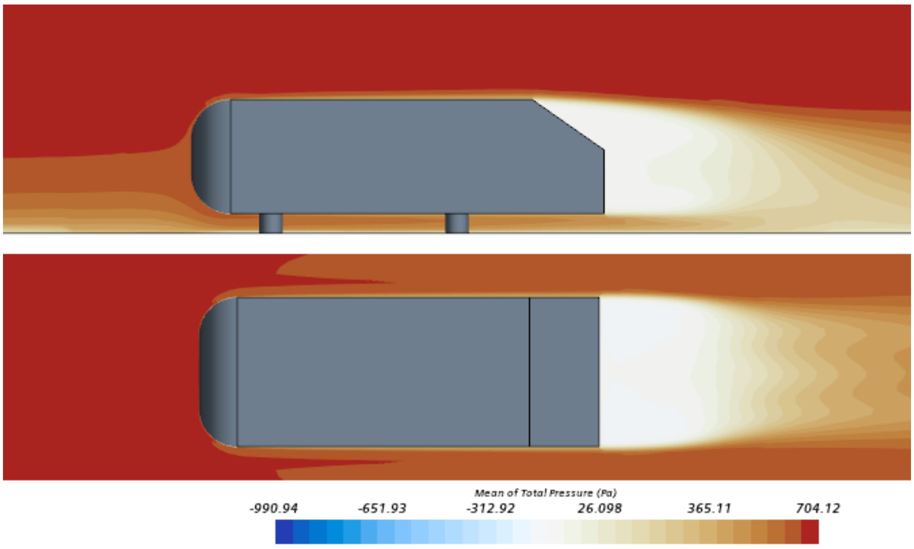

Figure 4.34: Mean Total Pressure distribution around the Ahmed body

Figure 4.34 shows the contour of total pressure around the Ahmed body. Pressure difference is seen very close to the surface from the front curve till the mid-span of the Ahmed body due to the streamline curvature at the front edge of the body. At the slant and the rear regions, the pressure is significantly low compared to other areas. This difference in pressure causes drag and since the difference is high, the drag is also high. The entire wake region starting from the upper slant edge is a low pressure region.

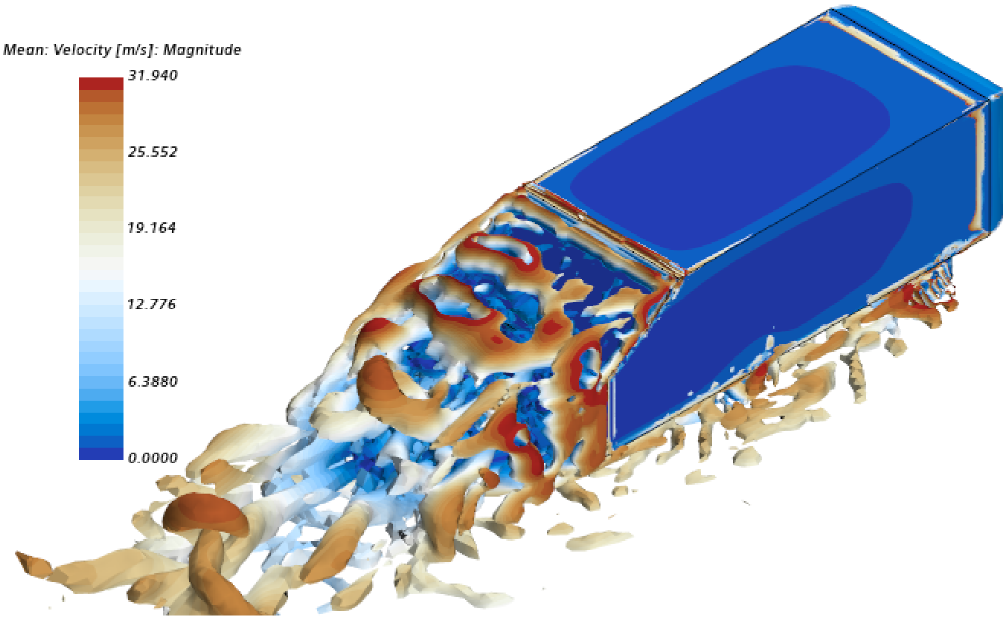

Figure 4.35: Turbulent vortices around the Ahmed body visualized by Q-criterion ($Q = 10000/s^2$)

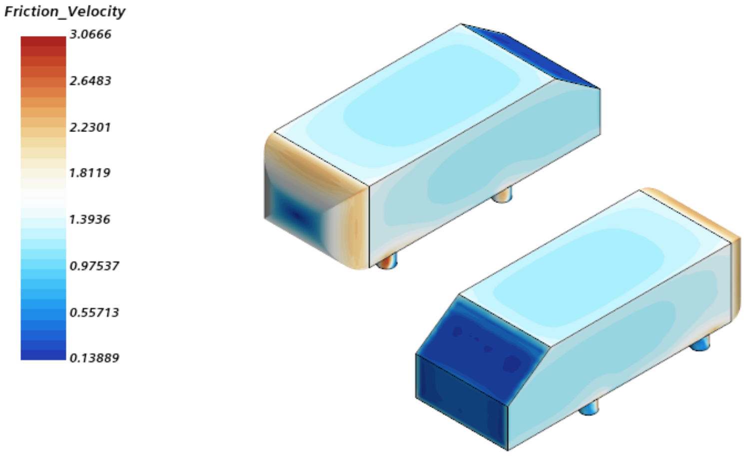

Figure 4.36: Shear velocity profile on Ahmed body with slant angle 35°

As discussed in Section 4.4.1.1, Q-criterion is used as a method to detect formation of vortex structures using iso-surfaces. In this analysis, an iso-value of 1000/s^2 is used and it is coloured by the mean velocity magnitude. Since the simulation settings is the same for all the cases, the characteristics are same at the front and mid-span regions.

It can be observed in Figure 4.35 that there is a formation of 2 discontinuous counter rotating trailing cone vortices on each side of slant edges. These vortices are weak and hence the flow is completely separated from the slant surface due to a very steep slant angle of 35°. There are horse-shoe vortices or U shaped vortices being formed at the rear wake region as well.

As discussed in the baseline configuration Section 4.4.1.1, the shear velocity is used to investigate the shear at the surface of the Ahmed body. The same has been investigated for the 35° slant angle configuration. The friction velocity is comparatively low along the edges of the rear and slant surfaces. They are slightly higher the central portion of both rear and slant surfaces as seen in Figure 4.36. However, if we take a look at the front, the velocity is relatively high at the curvature but lowest by the middle of the front surface. On the top and sides, the shear velocity magnitude is ranging from 1-1.5 m/s. The mid section of both top and side surfaces illustrate lower values of shear velocity and it increases gradually by the outer edges.

4.5 Analysis of Snow Contamination

4.5.1 The Wedge

Particle-wall collisions being the focal point of this analysis, *Boundary sampling* module in StarCCM+ is used to record parcel states when they impact on the respective surfaces of the bluff body. Collision statistics so collected through this approach are then processed on Python and finally visualized using Paraview.

Figure 4.37 illustrates the areas of initial particle collisions onto the surface for Backward Configuration. At the front surface, most of the surface is being contaminated by the particles. Upon flow separating along the edges at the front, they retract back beyond the mid-span of the side surfaces. Thereby, relatively more contamination is seen towards the trailing edge of the side surfaces. On the slant surface however, most particles tend to gather all throughout the surface instead of just being on the top and side surfaces as in the experiments. From Figure 4.38 observations similar to the one seen from boundary sampling can be confirmed.

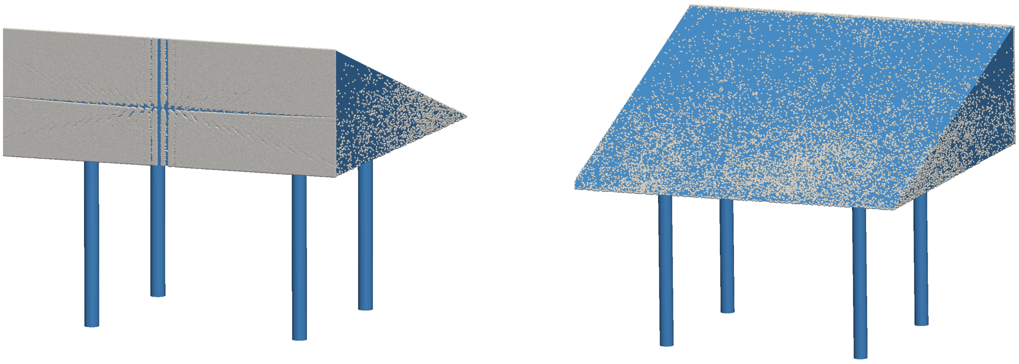

Figure 4.37: Initial impact of particles onto the Wedge surface

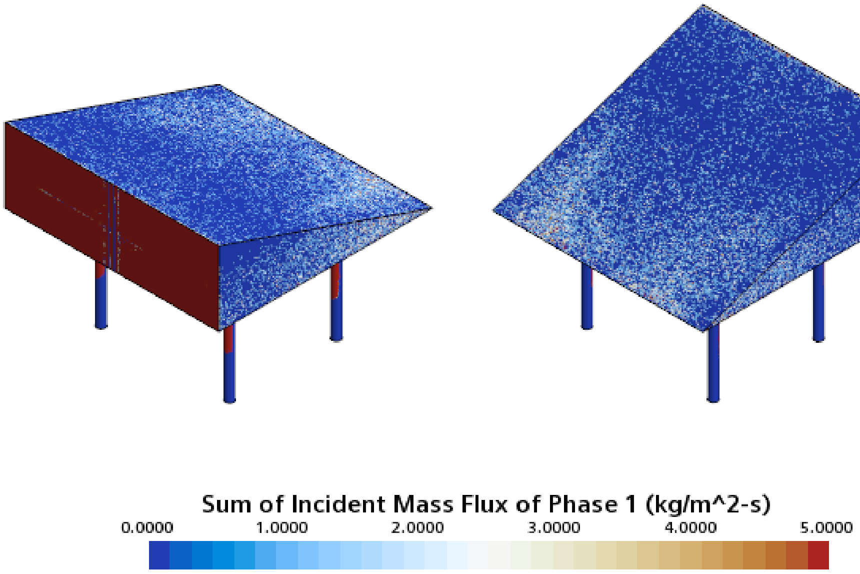

Figure 4.38: Sum of incidence mass flux for the Wedge: backward configuration

4.5.2 Ahmed Body

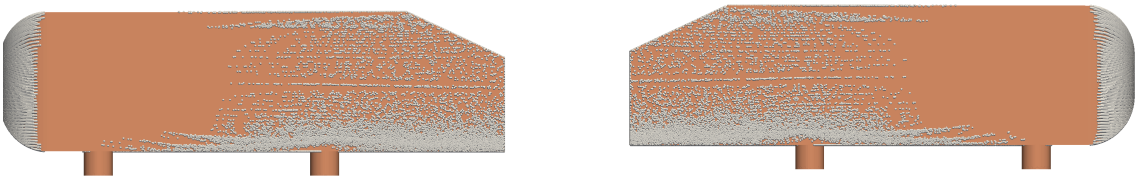

(a) Left surface

(b) Right surface

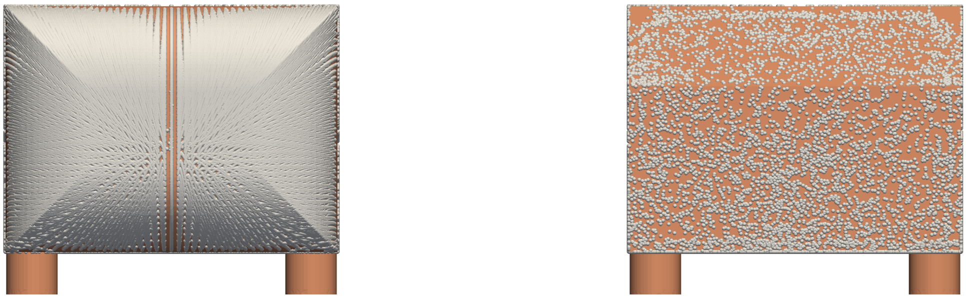

(c) Front surface

(d) Rear surface

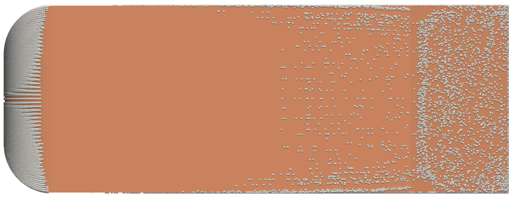

(e) top surface

Figure 4.39: Initial impact of Snow particles on Ahmed body

Figure 4.39 shows the areas where initial collisions occur on the Ahmed body from boundary sampled data. This is not to be misunderstood with the areas where particles accumulate, since particles may either suspend away from or adhere to the surface dependently. It can be observed that particles tend to collide throughout the front surface. On the top and side surfaces, however, they do not collide on the immediately adjacent area while the remaining surfaces experience collisions. This is can be correlated to the results from the aerodynamic field where the curvature on the front surface causes flow separation and it retracts shortly further downstream. On the slant and rear surfaces, initial collisions are observed throughout the surfaces but they are slightly higher at the extreme corners.

Figure 4.40 shows the sum of Incidence mass flux of the particles along different surfaces on the Ahmed body. The findings in connection to Figure 4.39 are much evident.

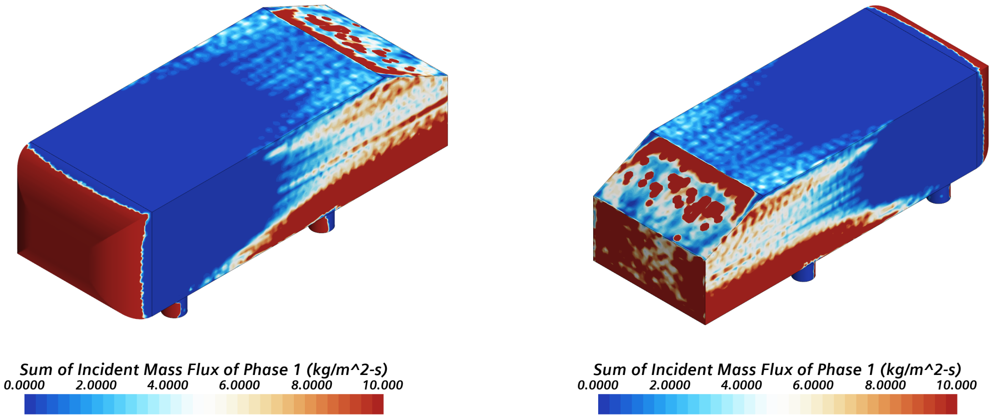

Figure 4.40: Sum of Incidence mass flux of initial particle collisions

However, in comparison with the snow contamination pattern observed from experiments, it can be noted that there exists significant differences.

a. **Front surface**: no contamination is recorded from the experimentation while most of the surface experiences particle collisions in simulation.

b. **Top and side surfaces**: Snow contamination is observed all throughout these surfaces in experiments while collisions are recorded only beyond the mid-span of the Ahmed body in simulation.

c. **Slant surface**: Denser mass flux is recorded at regions where higher snow deposition is seen in the experiments. However, the contamination pattern seen around the middle section is only in partial agreement with that seen from simulation.

d. **Rear surface**: Significant deposition is seen along the edges and the middle section from experiments. In simulation however, they do not exactly resemble the experiments but collisions are mainly observed along the edges alone.

Figure 4.41 represents the regions of both, particles that adhere as well as the ones that suspend away from the surface, for the baseline configuration (slant angle 25°). Particles colored with white represents the ones that adhere to the surface while the ones colored in blue corresponds to those that suspend away upon initial collision. It is observed that most of the particles along the corners of front surface suspend away while a small portion at the middle remains. Furthermore, particles along the bottom and upper edges of both the side surfaces suspend away. Similar observation can be made along the corners at the top as well.

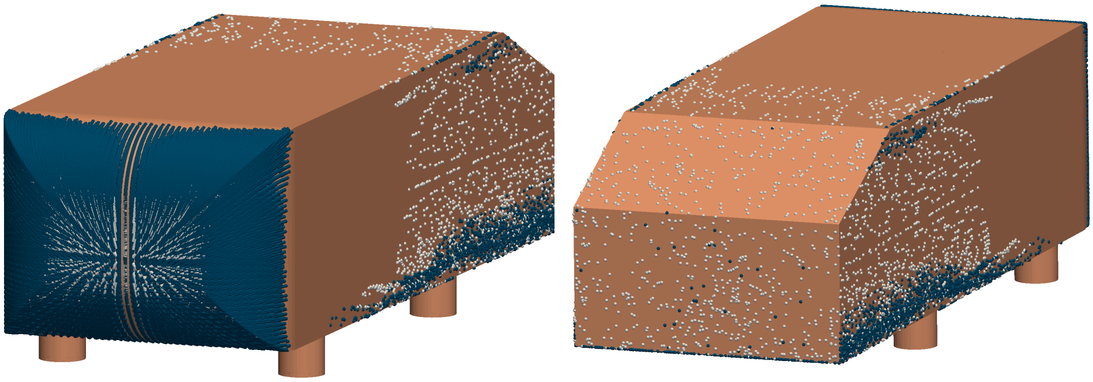

Figure 4.41: Visualization of Particle re-suspension criterion for Ahmed body with slant angle 25° when $\rho_p = 920 kg/m^3$

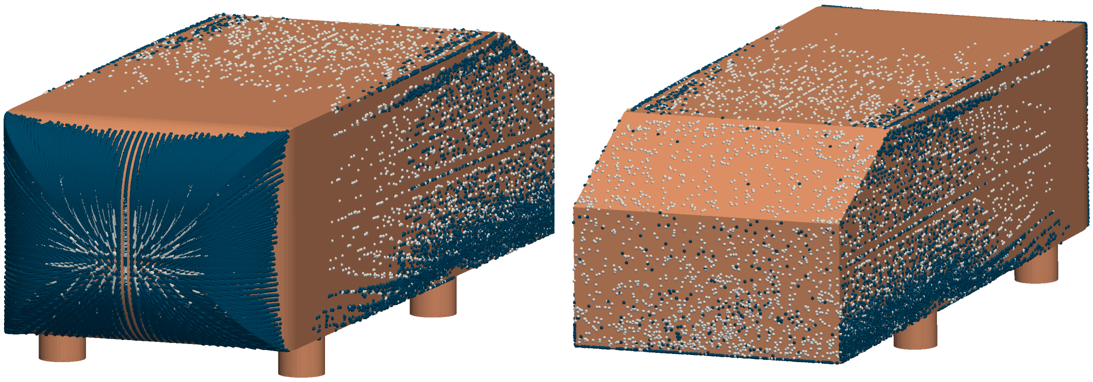

Figure 4.42: Visualization of particle re-suspension criterion for Ahmed body with slant angle 25° when $\rho_p = 460 kg/m^3$

Now that differences within accumulation pattern between simulations and experiments are observed, a study was carried out to evaluate the effect of solidity (hollowness) of the particles. Figure 4.42 shows the results from initial collisions on Ahmed body when particle density is halved (i.e. $\rho_P = 460\ kg/m^3$). Observing the initial impact of particles along different surfaces, it can be observed that particles impact at locations much closer to the leading edge on the top and side surfaces when compared the particle density in previous case (i.e. $\rho_P = 920\ kg/m^3$). Also, it can be observed that the particle deposition is much more dense on the rear and slant surfaces in the latter case. This leads to a speculation that snow particles from PVKA maybe hollow and that is yielding in snow deposition in less expected areas.

Furthermore, observations from Singh et al. shows that machine-made snow being produced very rapidly may result in ice crystals that contain a pocket of air, a bulge or may even be broken [37]. To further understand the validity of this speculation, there is a requirement for further investigations corresponding to the solidity of the particle.

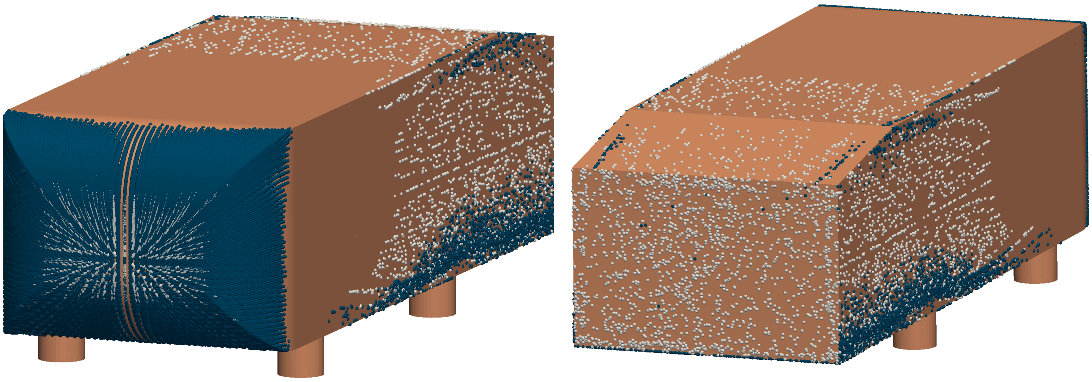

Figure 4.43: Visualization of particle re-suspension criterion for Ahmed body with slant angle 10°

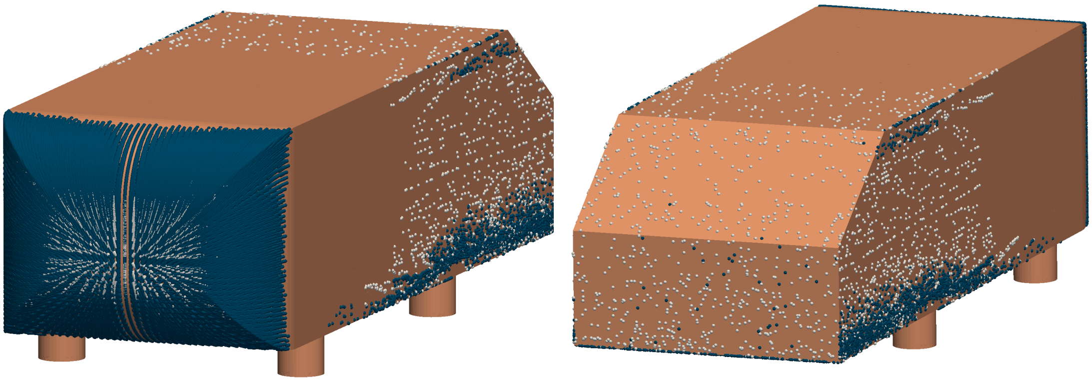

Figure 4.44: Visualization of particle re-suspension criterion for Ahmed body with slant angle 35°

Figures 4.43 and 4.44 illustrates the initial collisions on the Ahmed body with slant angle configurations 10° and 35° respectively. Similar observations as seen in 25° case is seen at the top and side surfaces. On the slant and rear surfaces, it is observed that in these cases the accumulation pattern does vary slightly with variation in rear slant angles.

4.6 Comparison between Present Simulation and Experimental Results

4.6.1 Aerodynamic Flow Analysis

From the experiments in wind tunnel, it was observed that there was snow deposition in the least expected areas like those of top and side surfaces. The shear will be high due to high velocities on these surfaces. This was the reason to go ahead with the tuft experiment to check if the flow is attached to or detached from the surface. The experiment was conducted in the wind tunnel on the Ahmed body with slant angle 10° as described in the Section 4.3.0.4. So to compare the flow in the aerodynamic simulation, a streamline visualization of mean velocity magnitude was set up for the same angle as seen in Figure 4.45b.

(a) Tufts on Ahmed body subjected to wind speed in the wind tunnel

(b) Velocity Streamlines of Mean of Velocity: magnitude

Figure 4.45: Comparison of flow along the Ahmed body surface with slant angle 10° from experiment and aerodynamic simulation

From Figure 4.45b, it can be clearly observed that the flow is attached on the top and side surfaces and its the same when compared to the tuft experiment where the tufts are attached to the surfaces in Figure 4.45a. This explains although the flow is attached to the surface, a uniform snow deposition is still seen in the top and side surfaces. So the reason for it's deposition maybe because of some other factor or reason.

4.6.2 Drag Coefficient Analysis

Table 4.1 gives a comparison of the drag coefficient values obtained from the simulations conducted using IDDES turbulence models and those obtained from the experiments conducted in previous works.

Table 4.1: Drag coefficient (C_d) obtained from simulation and literature experimental data

Source	Drag coefficients (C_d)			Reynolds number (Re)
	10°	25°	35°	
Present Simulation (IDDES)	0.225	0.246	0.240	2.78 x 10^6 [36]
Guilmineau et al. - Sim. [38]	-	0.380	0.345	1.2 x 10^6
Ahmed et al. - Exp. [31]	0.232	0.285	0.258	4.29 x 10^6
Meile et al. - Exp. [39]	-	0.299	0.279	2.78 x 10^6
Corallo et al. - Sim. [40]	0.31	0.32	-	9.8 x 10^4

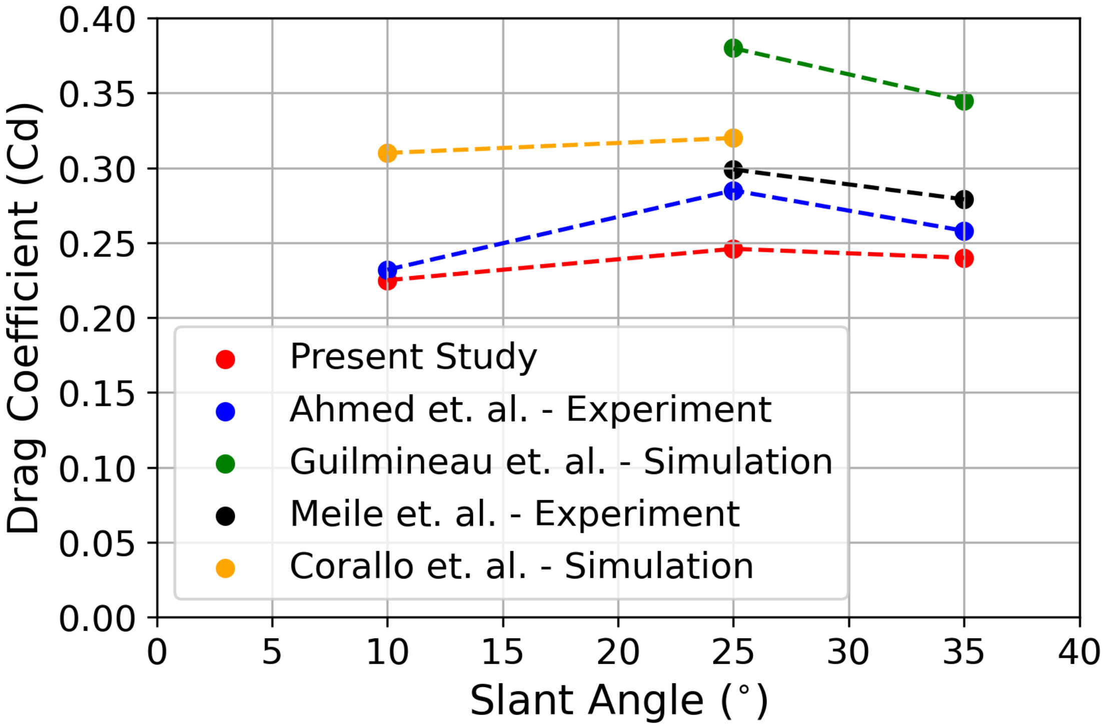

Figure 4.46: Drag Coefficient versus Slant angle of Ahmed body

The simulations and wind tunnel experiments in our case were conducted and performed at a wind speed of 115 km/h for Ahmed body. This corresponds to a height based Reynolds number (Re) of 2.78 million. The Re was taken as reference from Lienhart et al. [36] and then was used to calculate the wind speed to be used at -15°C. Ahmed et al. used a Re of 4.29 million to conduct the experiment by running it at a wind speed of 216 km/h which is much higher than what is used in our simulations [31]. However, Guilmineau et al. have used a Re of 1.2 million in their numerical simulations. as seen in the Table 4.1 and Figure 4.46 [38]. Meile et al. have used the same Re in their experiments as used by Lienhart et al. [39]. Corallo et al. have used a Re of the order of 10^4 which is two orders of magnitude lesser than the rest of the simulations and experiments mentioned [40]. The drag coefficients obtained in our simulation for 25° and 35° are in close agreement the experiments as seen in the Table 4.1 and Figure 4.46. However, the drag coefficents for the slant angles in the present study underpredict them when compared with the simulation results from the literature.

4.6.3 Choice of Particle Force Model

It is very important to make the appropriate choice of Particle force model in order to ensure the particles in the vicinity of the bluff body experiences sufficient turbulent interaction. Figure 4.47 compares between three scenarios for the baseline simulation of Ahmed body: no particle force treatment, implementation of DRW model and Turbulent Dispersion model within StarCCM+.

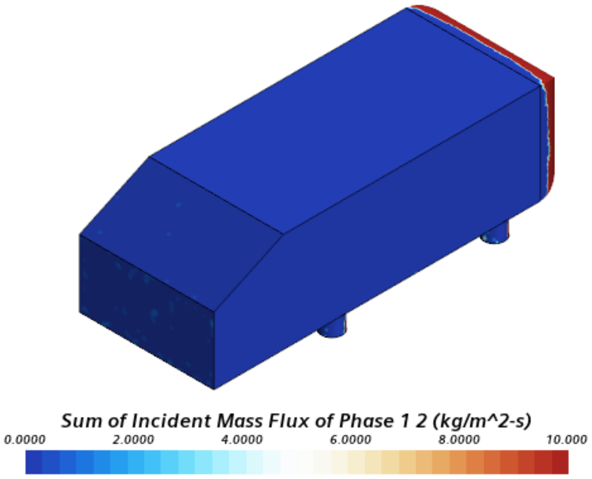

(a) Null

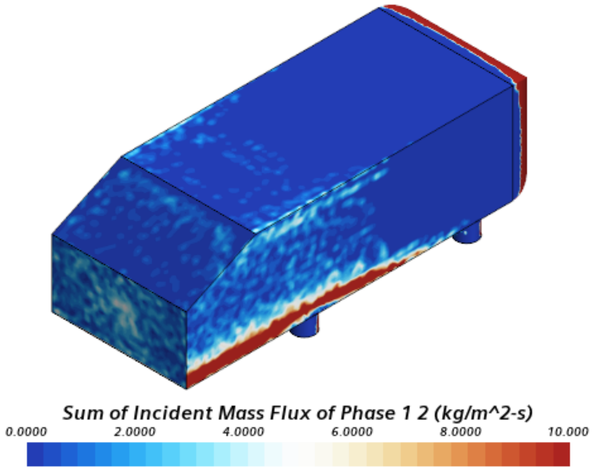

(b) User defined DRW

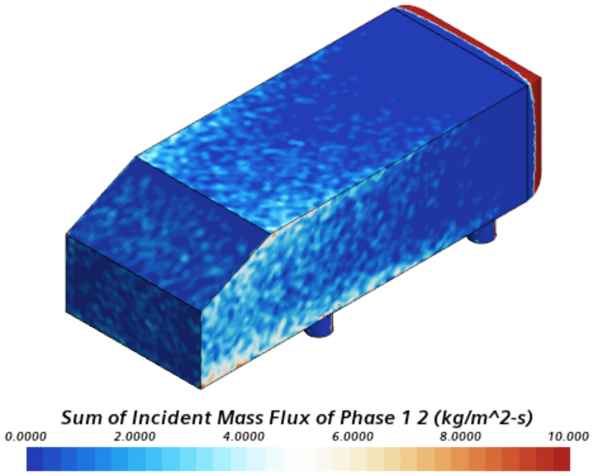

(c) Turbulent dispersion

Figure 4.47: Comparison between different particle force models

It is observed in Figure 4.47a that collisions occur mostly along the front and rear surfaces while no collisions are recorded along the other surfaces. From Figure 4.47b however, it is seen that enforcing DRW model to particle enhances their ability to interact with the turbulent flow field and hence resulting in improved interaction with the wall surfaces. Another choice has also been implemented for the same, that is the *Turbulent Dispersion* Module within StarCCM+ as seen in Figure 4.47c. It is to be noted that the latter model predicts much wider area of contamination than the previous case but given that fact that this module is not a direct implementation on star for the IDDES turbulence model, validity of results is not fully known.

4.6.4 Time Comparison Study

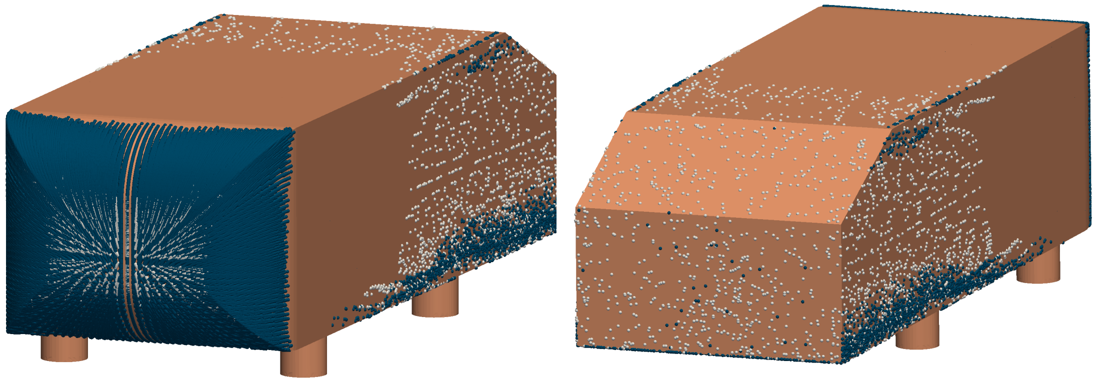

(a) Runtime = 1.0 s **(b)** Runtime = 1.0 s

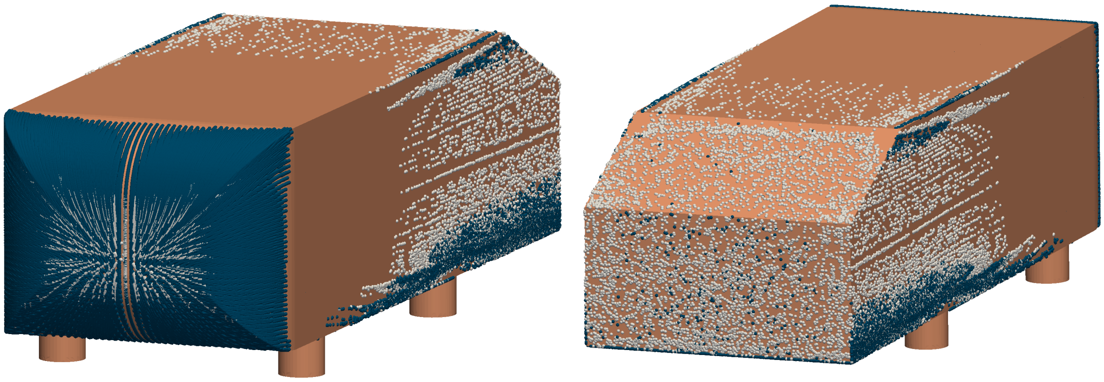

(c) Runtime = 2.5 s **(d)** Runtime = 2.5 s

Figure 4.48: Comparison of snow contamination pattern for Ahmed Body at various runtimes

In the previous sections so far, collision pattern of snow particles has been studied, followed by treatment of particle re-suspension upon initial impact. The order of time comparison between simulation and experiments vary between 0.5 [s] for simulation up to 30 minutes in the wind tunnel respectively. Hence, It would be more meaningful to look at the development in contamination for increasing simulation run time and check if they largely vary, before comparing with experiments.

Figures 4.48a and 4.48b depicts the snow deposition pattern for a simulation runtime of 1.0 seconds while figures 4.48c and 4.48d depict the snow deposition pattern for a simulation runtime of 2.5 seconds. It is observed that longer simulation times certainly improves the sample count during boundary sampling, as a result of which much prominent deposition is observed within the contaminated areas. However, no visible increase in the areas of deposition is observed. Therefore it can be inferred that simulation runtime is not necessarily the parameter affecting the contamination area.

4.6.5 Snow Accumulation Pattern

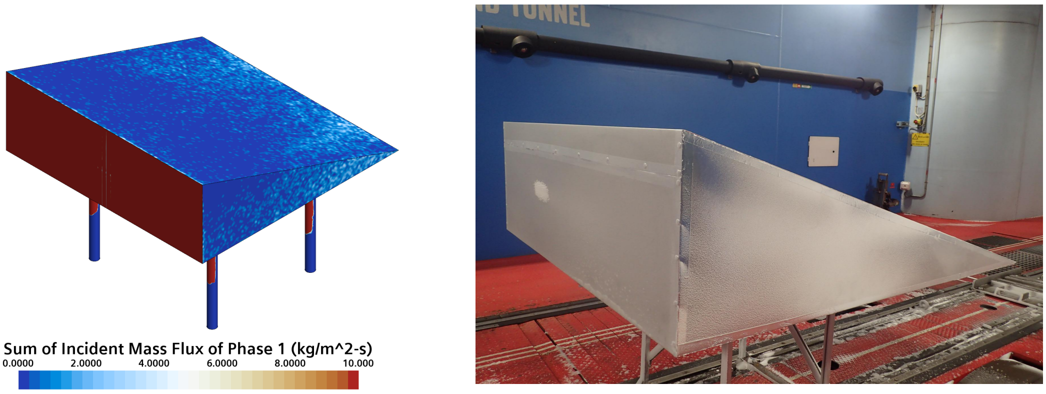

(a) Diagonal View: Simulation

(b) Diagonal View: Experimental

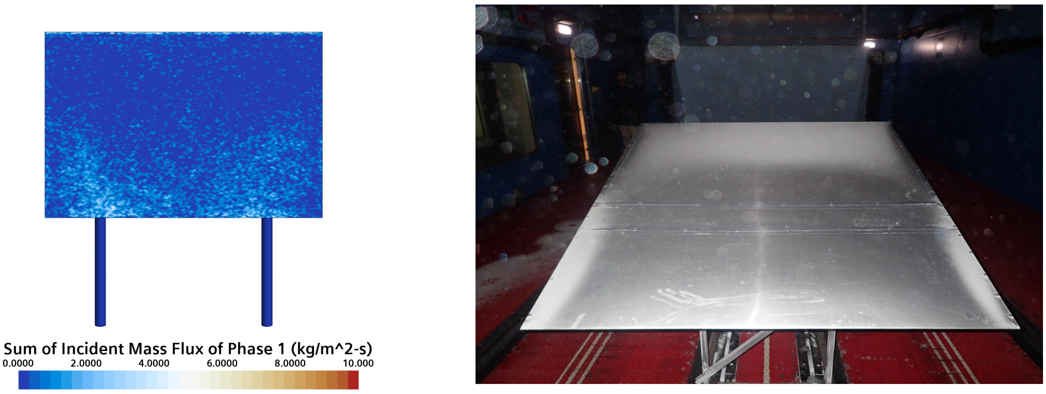

(c) Rear View: Simulation

(d) Rear View: Experimental

Figure 4.49: Comparison of snow accumulation pattern for the Wedge: Backward configuration

Figure 4.49 compares the snow accumulation in experimental versus the simulation. It is observed that particle-wall collisions occur as they are expected to, without the aid of additional particle force model. The simulation results are in fair agreement with the accumulation pattern as seen in the experiments along the side surfaces.

However, that is not the case with the slant surface where snow accumulation is observed mostly along the bottom half and very close along the upper corner.

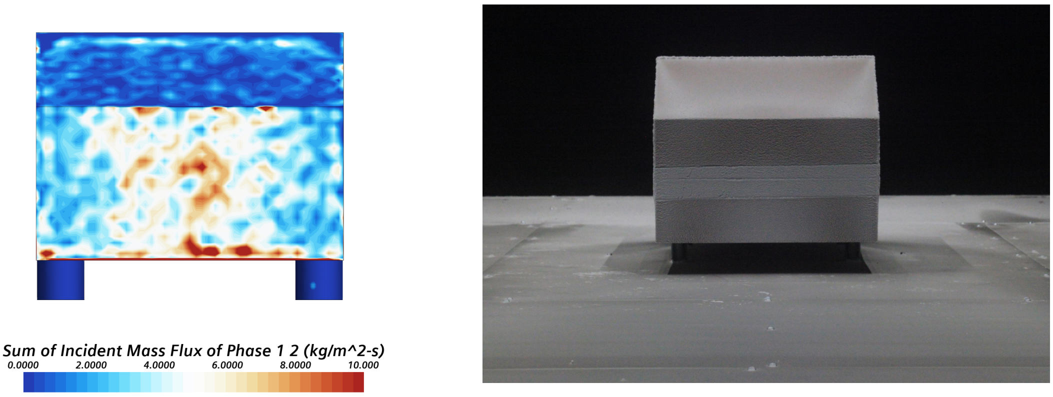

(a) Rear View: Simulation

(b) Rear View: Experimental

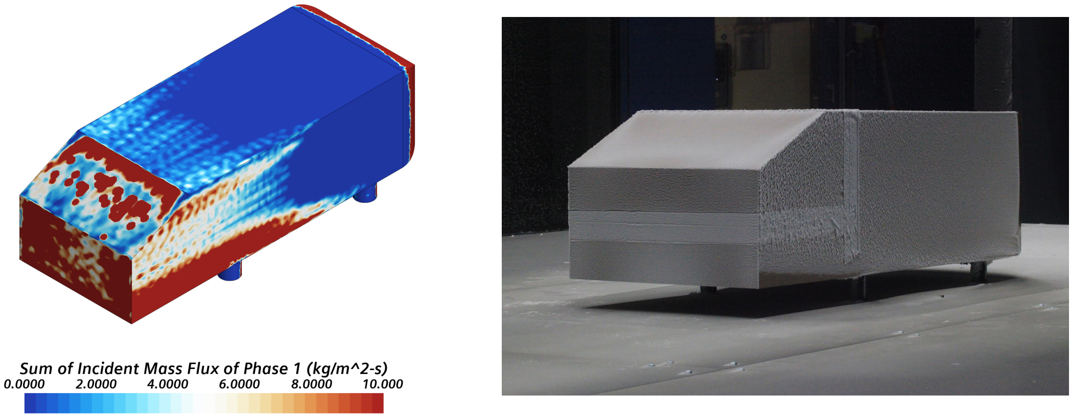

(c) Diagonal View: Simulation

(d) Diagonal View: Experimental

Figure 4.50: Comparison of snow accumulation pattern for Ahmed body with slant angle 25°

Figures 4.50, 4.51 and 4.52 compare the accumulation pattern of particles after a simulation run-time of 2.5 seconds physical time with the results obtained from experiments, for slant angle configurations of 25°, 10° and 35° respectively. Looking at the similarities between each other, it can be observed that the current particle force model is accounting for particle collisions across all of the surfaces when compared with that without any particle force model. However, no contamination seen on the front half of of top and side surfaces which is the issue at hand. Furthermore, the particle re-suspension model is able to account for the particle re-suspension at the wall with a reasonable correlation with the experimental observations (such as at the front surface). The understanding that with Re_P being bigger than the size of the boundary layer, them shearing away explains the reason why machine-made snow tends to adhere much more when compared to natural snow. As a consequence of this, snow accumulation is observed in the least expected areas during the wind tunnel tests. One must also note that the particle re-suspension is currently being treated only after initial impact. But in reality, a particle may collide again more than once upon suspending from the wall. Hence, multi-stage collisions of particles is also another thing to be accounted in the model to obtain a more resembling pattern to that of experiments.

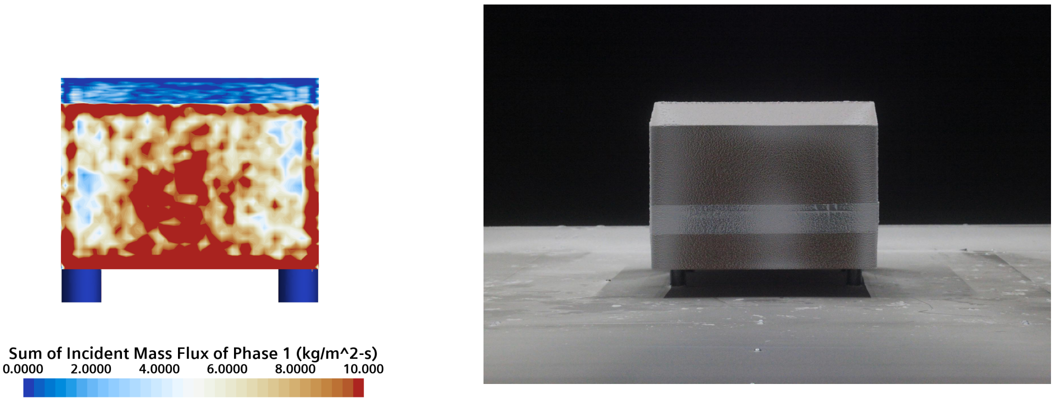

(a) Rear View: Simulation

(b) Rear View: Experimental

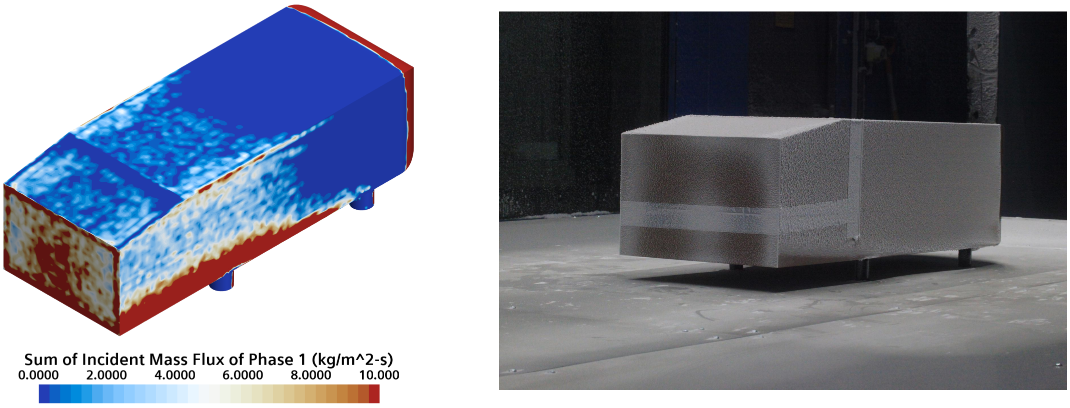

(c) Diagonal View: Simulation

(d) Diagonal View: Experimental

Figure 4.51: Comparison of snow accumulation pattern for Ahmed body with slant angle 10°

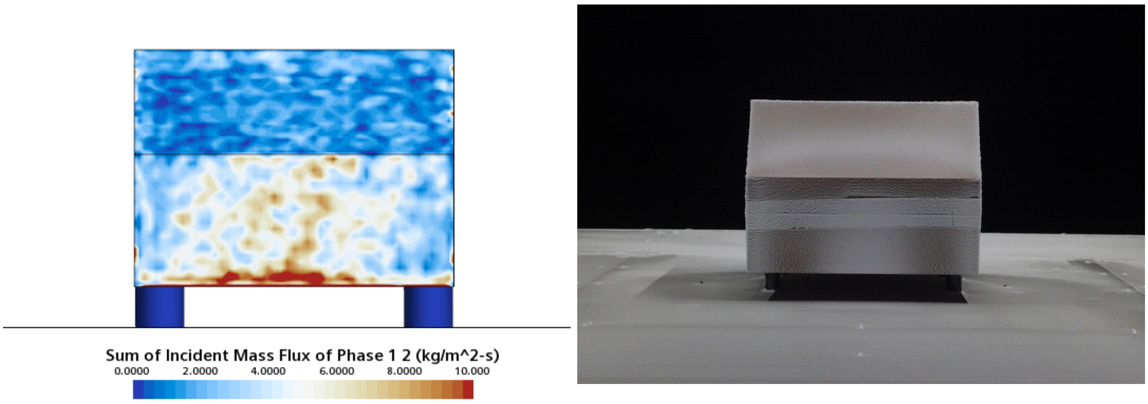

(a) Rear View: Simulation

(b) Rear View: Experimental

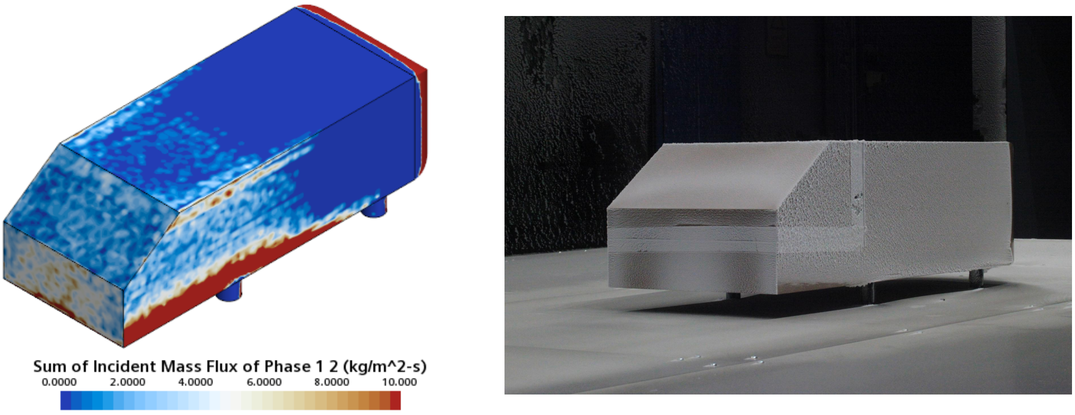

(c) Diagonal View: Simulation

(d) Diagonal View: Experimental

Figure 4.52: Comparison of snow accumulation pattern for Ahmed body with slant angle 35°

5

Conclusion

The before said objectives were mainly classified into two parts, namely, CFD analysis and experimental analysis. Throughout the CFD analysis, aerodynamic flow over different possible geometric features has been studied. This, in reality, holds good relevance to many of the common geometric features one can observe in a real-world car. Particularly, analysis over a wedge section has given considerable understanding comparing to that of an automotive spoiler for example, its different aerodynamic features and expected areas of contamination due to snow. Also, this has aided in establishing a baseline further for conducting this type of analysis.

Furthermore, analysis of an Ahmed body has proven to be of significant importance in many ways: firstly, it resembles the common geometric features of a real-world car. Secondly, it is a simplified model that saves a lot of computational resources, effort and time while conducting any method development (car in this case) and testing out different simulation approaches. The difference in contamination pattern with varying rear slant angles has been of valuable importance since this section of the geometry largely influences the aerodynamic flow over a car and possible snow contamination subsequently.

On the other hand, experimental investigations on the above mentioned bluff bodies have supplemented with quality results, thereby facilitating the comparison between the both. It has been observed that snow contamination occurs in areas that are least expected from CFD predictions. This has further opened up the possibilities to incorporate a particle force model to account for the turbulent dispersion of particles. Also, further work has been performed to account for the post-collisional treatment of particle-wall interactions through the particle re-suspension model. Even though the considerations taken towards developing this approach has been in their early stages, it is seen to be reasonably reliable in predicting the snow contamination for a given geometry. Further improvements to this approach would enhance the accuracy of predictions and also aid towards predictions much closer to the real-world phenomenon.

Prediction of snow contamination on cars or automotive exterior in general, during the course of this thesis has aided towards identifying potential areas of contamination. This approach implied to a real-world car further aids in smart placement of sensors or maybe even into evaluating various methods to de-contaminate them. Consequentially, unhindered functioning of the many different components of active safety systems can be expected. Such an outcome has multi-fold benefits. Firstly, it aids towards technological advancements in autonomous driving. This means that higher level of passenger safety can be ensured and life hazards due to road accidents, correspondingly. Furthermore, it would be a much befitting contribution to the Sustainable Development Goals (SDG's) set by the Department of Economic and Social Affairs, United Nations, thereby leading mankind towards sustainable transportation in general.

6

Future Scope of Work

Prediction of snow contamination on cars has been an increasingly demanding area of research in recent times due to the rapidly advancing automation technologies within the automotive industry. Many different approaches have been evaluated in the works previous to this thesis. IDDES approach being a hybrid approach towards modeling turbulence has had its advantages and limitations. It has proven to be a cost-effective approach in comparison with the full-scale LES or DNS approach while also yielding many accurate predictions when compared to RANS. However, it has had its limitations when it comes to modeling near-wall turbulence which has demanded the need for supplementary Turbulent dispersion modeling. Should this model be employed, it requires further improvements in predicting the deposition pattern more likely to that seen from experiments.

In the context of this thesis, particle-wall interaction alone has been considered here for studying the transport of snow particles. However, that may not be entirely correct since particle-particle interaction must also be accounted for.

Perfectly smooth walls have been assumed in the current approach. Inclusion of effect due to surface roughness would more likely mimic the real-world phenomenon. As a limitation within this thesis, only spherical particles have been considered. As discussed in earlier sections, snow particle exists in different shapes. Hence, considering non-sphericity of particles would be beneficial. Snow in general, exists in various forms, for example, dry snow and wet snow. The existence of these varieties is temperature-dependent. Therefore, the temperature dependency of snow buildup is another area that is to be studied.

Finally, to utilize the so developed particle simulation approach, the solver must be supplied with the model. Developing this model further into a user-defined code would be more tangible for industrial usage or commercial purposes in general.

Bibliography

[1] Tobias Eidevåg. *Snow Contamination of Cars: Collisions of Ice Particles with Surfaces.* PhD thesis, Chalmers University of Technology, 2020.

[2] Lars Davidson. Fluid mechanics, turbulent flow and turbulence modeling, 2015.

[3] B Çuhadaroğlu. An analysis of the turbulent boundary layer on a porous wall with transpiration. *ARI-An International Journal for Physical and Engineering Sciences*, 50(2):127–130, 1997.

[4] Clayton T Crowe, John D Schwarzkopf, Martin Sommerfeld, and Yutaka Tsuji. *Multiphase flows with droplets and particles.* CRC press, 2011.

[5] U Nakaya. Snow crystals, natural and artificial. harvard university press, 510. 1954.

[6] Henri Bader, Johannes Neher, Otto Eckel, Christian Thams, Robert Haefeli, and Edwin Bucher. *Der schnee und seine metamorphose.* Kommissionsverlag Kümmerly & Frey, Druck von Aschmann & Scheller a.-g., Zürich, 1939.

[7] Tobias Eidevåg, Erik S Thomson, Sofia Sollén, Johan Casselgren, and Anders Rasmuson. Collisional damping of spherical ice particles. *Powder Technology*, 383:318–327, 2021.

[8] Markus Enmark. Cfd modeling of snow contamination on cars. implementation of a snow adhesion regime map by user defined functions. Master's thesis, 2016.

[9] Eric Serre, Matthieu Minguez, Richard Pasquetti, Emmanuel Guilmineau, Gan Bo Deng, Michael Kornhaas, Michael Schäfer, Jochen Fröhlich, Christof Hinterberger, and Wolfgang Rodi. On simulating the turbulent flow around the ahmed body: A french–german collaborative evaluation of les and des. *Computers & Fluids*, 78:10–23, 2013.

[10] Adrian P Gaylard, John Pitman, Jonathan Jilesen, Adriano Gagliardi, Bradley Duncan, John Wanderer, and Alex Konstantinov. Insights into rear surface contamination using simulation of road spray and aerodynamics. *SAE International Journal of Passenger Cars-Mechanical Systems*, 7(2014-01-0610):673–681, 2014.

[11] Stefan Roettger, Martin Schulz, Wolf Bartelheimer, and Thomas Ertlt. Automotive soiling simulation based on massive particle tracing. In *Data Visualization 2001*, pages 309–317. Springer, 2001.

[12] Thomas Hagemeier, Michael Hartmann, and Dominique Thévenin. Practice of vehicle soiling investigations: A review. *International Journal of Multiphase Flow*, 37(8):860–875, 2011.

[13] Michiya Higa, Masahiko Arakawa, and Norikazu Maeno. Size dependence of restitution coefficients of ice in relation to collision strength. *Icarus*, 133(2):310–320, 1998.

[14] M Sommerfeld. Modelling of particle-wall collisions in confined gas-particle flows. *International Journal of Multiphase Flow*, 18(6):905–926, 1992.

[15] Tobias Eidevåg, Per Abrahamsson, Matthias Eng, and Anders Rasmuson. Modeling of dry snow adhesion during normal impact with surfaces. *Powder Technology*, 361:1081–1092, 2020.

[16] Henk Kaarle Versteeg and Weeratunge Malalasekera. *An introduction to computational fluid dynamics: the finite volume method.* Pearson education, 2007.

[17] Wolf Hucho and Gino Sovran. Aerodynamics of road vehicles. *Annual review of fluid mechanics*, 25(1):485–537, 1993.

[18] Florian R Menter, Martin Kuntz, and Robin Langtry. Ten years of industrial experience with the sst turbulence model. *Turbulence, heat and mass transfer*, 4(1):625–632, 2003.

[19] Mikhail L Shur, Philippe R Spalart, Mikhail Kh Strelets, and Andrey K Travin. A hybrid rans-les approach with delayed-des and wall-modelled les capabilities. *International Journal of Heat and Fluid Flow*, 29(6):1638–1649, 2008.

[20] Tony Persson. *Eulerian-Lagrangian Modeling of Multicomponent Spray for Aseptic Treatment of Carton Bottles in the Food Process and Packaging Industry.* PhD thesis, Master's Thesis in Applied Mechanics, 2013.

[21] Elaine S. Oran and Jay P. Boris. Fluid dynamics. In Robert A. Meyers, editor, *Encyclopedia of Physical Science and Technology (Third Edition)*, pages 31–43. Academic Press, New York, third edition edition, 2002.

[22] *User Guide: Star-CCM+ version 2020.2.* CD-ADAPCO, 2020.

[23] Martin R Maxey and James J Riley. Equation of motion for a small rigid sphere in a nonuniform flow. *The Physics of Fluids*, 26(4):883–889, 1983.

[24] George Gabriel Stokes et al. On the effect of the internal friction of fluids on the motion of pendulums. 1851.

[25] Clement Kleinstreuer and Yu Feng. Computational analysis of non-spherical particle transport and deposition in shear flow with application to lung aerosol dynamics—a review. *Journal of biomechanical engineering*, 135(2), 2013.

[26] SC Colbeck. An overview of seasonal snow metamorphism. *Reviews of Geophysics*, 20(1):45–61, 1982.

[27] DA Miller, EE Adams, and RL Brown. A microstructural approach to predict dry snow metamorphism in generalized thermal conditions. *Cold regions science and technology*, 37(3):213–226, 2003.

[28] CRLA Fierz, Richard L Armstrong, Yves Durand, Pierre Etchevers, Ethan Greene, David M McClung, Kouichi Nishimura, Pramod K Satyawali, and Sergey A Sokratov. The international classification for seasonal snow on the ground. 2009.

[29] Yeswanth Sai Tanneru. A dem study to investigate the influence of ice particle adhesion on the angle of repose. 2020.

[30] Christophe Henry and Jean-Pierre Minier. Progress in particle resuspension from rough surfaces by turbulent flows. *Progress in Energy and Combustion Science*, 45:1–53, 2014.

[31] Syed R Ahmed, G Ramm, and G Faltin. Some salient features of the time-averaged ground vehicle wake. *SAE Transactions*, pages 473–503, 1984.

[32] Tural Tunay, Besir Sahin, and Veli Ozbolat. Effects of rear slant angles on the flow characteristics of ahmed body. *Experimental Thermal and Fluid Science*, 57:165–176, 2014.

[33] Patrick Gilliéron and Francis Chometon. Modelling of stationary three-dimensional separated air flows around an ahmed reference model. In *ESAIM: Proceedings*, volume 7, pages 173–182. EDP Sciences, 1999.

[34] Boris Conan, Jérôme Anthoine, and Philippe Planquart. Experimental aerodynamic study of a car-type bluff body. *Experiments in fluids*, 50(5):1273–1284, 2011.

[35] Markus Enmark. Implementation of a snow adhesion regime map for cfd simulations of vehicle contamination. 2017.

[36] Hermann Lienhart and Stefan Becker. Flow and turbulence structure in the wake of a simplified car model. *SAE transactions*, pages 785–796, 2003.

[37] V. Singh, P. Singh, and U. Haritashya. Encyclopedia of snow, ice and glaciers. 2011.

[38] Emmanuel Guilmineau, GB Deng, Alban Leroyer, P Queutey, Michel Visonneau, and J Wackers. Assessment of hybrid rans-les formulations for flow simulation around the ahmed body. *Computers & Fluids*, 176:302–319, 2018.

[39] Walter Meile, Günter Brenn, Aaron Reppenhagen, Bernhard Lechner, and Anton Fuchs. Experiments and numerical simulations on the aerodynamics of the ahmed body. *CFD letters*, 3(1):32–39, 2011.

[40] Matthew Corallo, John Sheridan, and Mark Christopher Thompson. Effect of aspect ratio on the near-wake flow structure of an ahmed body. *Journal of Wind Engineering and Industrial Aerodynamics*, 147:95–103, 2015.

Appendices

A

Few important Dimensionless Quantities

A.1 Stokes Number

In theory, for particles to take a trajectory similar to that of aerodynamic flow field, they must be able to adapt to the changes in the flow instantaneously. This ability of a particle is defined by the particle response time. This being a relative quantity, they are measured in terms of Stokes Number. It is given as:

$$St_V = \frac{\tau_V}{\tau_F} \tag{A.1}$$

where,
τ_V is the particle response time and τ_F is some characteristic time scale of the fluid phase.

When Stokes number << 1, particle response time is much less than that of fluid response time. Then, particles will have sufficient time to respond to the changes in fluid field. On the contrary, when Stokes number >> 1, particle response time is much greater than that of fluid response time. Then, particles will essentially not have much time to respond to the changes in fluid field and therefore remains little affected due to the changes in fluid flow.

A.2 Reynolds Number

$$Re_f = \frac{\rho |V_f| L}{\mu} \tag{A.2}$$

where V_f is the fluid velocity, L is some characteristic length and ρ_f is the density.

A.3 Particle Reynolds Number

Particle Reynolds number is based on the diameter of the particle and relative velocity between the particle and the surrounding fluid. It is defined as:

$$Re_p = \frac{\rho |V_s| D_p}{\mu} \tag{A.3}$$

where V_s is the particle slip velocity, u_p is the particle velocity and Re_p is the particle Reynolds number.

B

Discrete Random Walk (DRW) model

B.1 Criterion:

1. Check if the particle is in a cell that lies within a RANS operated region or LES operated region.
2. If it lies within RANS operated region, enforce the DRW model on to the corresponding particles/ volume cells.

B.2 Implementation:

1. Compute the velocity fluctuation (u')

   $$\texttt{Velocity fluctuation}(u') = \sqrt{\frac{2k}{3}}\ [m/s] \tag{B.1}$$

2. Compute normal vector pointing towards the direction of the bluff body.

   `-($${Body_centre}-[0,0,0])/mag(($${Body_centre}-[0,0,0]))` (B.2)

   with, *Bodycentre* defined as:

   `$${ParcelCentroid}-[Lx/2, Ly/2, Lz/2]` (B.3)

3. Compute the Particle force that is to be supplied.

   $$\texttt{ParForceVec}(F_{Particle}) = \frac{1}{2} * C_{d,p} * \rho * A_P * |V_s| * V_s \tag{B.4}$$

   with

   $$\texttt{Particle Drag coefficient}(C_{d,p}) = \frac{24}{Re_p}(1 + 0.15Re_p^{0.687}) \tag{B.5}$$

   $$V_s = (u') \tag{B.6}$$

4. Enforce implementation criteria:
   `${SaTurbDesFd}>=0.5?$${ParForceVec}: [0,0,0]`

Where *SaTurbDesFd* is the IDDES blending function.